Jül-4288

Institute for Energy Research (IEF)
Plasma Physics (IEF-4)

# Analysis of disruptions and their mitigation using ultra-fast observation systems

*Sergey Bozhenkov*

Mitglied der Helmholtz-Gemeinschaft

JÜLICH
FORSCHUNGSZENTRUM

# Analysis of disruptions and their mitigation using ultra-fast observation systems

*Sergey Bozhenkov*

Berichte des Forschungszentrums Jülich; 4288
ISSN 0944-2952
Institute for Energy Research (IEF)
Plasma Physics (IEF-4) Jül-4288

D 294 (Diss., Bochum, Univ., 2007)

Vollständig frei verfügbar im Internet auf dem Jülicher Open Access Server (JUWEL) unter
http://www.fz-juelich.de/zb/juwel

Zu beziehen durch: Forschungszentrum Jülich GmbH · Zentralbibliothek, Verlag
D-52425 Jülich · Bundesrepublik Deutschland
☎ 02461 61-5220 · Telefax: 02461 61-6103 · e-mail: zb-publikation@fz-juelich.de

# Abstract

A tokamak disruption represents a potential threat to the integrity and availability of fusion reactors and experiments to come. Disruption is a complex process in which the energy stored in the discharge is lost in two steps. First the thermal energy is released on a submillisecond time scale. Then the magnetic energy associated with the plasma current is dissipated in a resistive way. Fast release of the thermal energy during the first stage can lead to a significant erosion of the wall components - up to 100 $\mu$m per event. In elongated plasmas loss of the vertical control is typical in a disruption and leads to excitation of halo currents. Since these currents are closed in the wall, the vessel is subjected to strong $\vec{j} \times \vec{B}$ forces. High induced fields during the current decay can accelerate a beam of runaway electrons with energies of tens of MeV. A local deposition of such beam can lead to melting of the wall. To prevent machine damage it was proposed to soften the disruption consequences by a fast injection of impurities. Such plasma quenching by massive gas injection is the topic of this thesis.

Massive gas injections are performed with the aid of a fast valve activated by eddy currents. The absence of any ferromagnetic materials in the construction makes the valve suitable for the magnetic fusion environment. The valve was developed several years ago at the Forschungzentrum Jülich, however its main characteristics remained poorly known. For this reason the first part of the thesis is devoted to study of the valve characteristics. The study is based on direct observation of the piston motion by means of a fast framing camera. The piston stroke and the injection duration are shown to strongly depend on the operational pressure and the used gas. The same is true for the valve throughput. The knowledge of the injection duration is also used to deduce the pressure decay rates and the gas outflow rates. The dependence of gas outflow rate on the piston stroke shows that the outflow rates can be increased by a factor of 4 by modifying the diameter of output orifice by a factor of 2. The modified valve is currently in operation at TEXTOR.

Disruption mitigation experiments with the fast valve were conducted at TEXTOR. The superior ultra-fast framing camera system that is available at TEXTOR allows detailed and systematic studies of the impurities dynamics. Together with complementary diagnostics (ECE, Thomson scattering, soft X-ray camera) these data reveal that the plasma quenching is gradual only at the beginning of the gas puff. As soon as the edge safety factor becomes equal to 2 the plasma is destabilized and the core of the discharge collapses. This phenomenology is confirmed in a wide range of gas pressures 1.5 – 20 bar and for different used gases: $D_2$, He, Ar, 5% Ar + 95% $D_2$, 10% Ar + 90% $D_2$, 20% Ar + 80% $D_2$. The thermal quench of the induced disruption, i.e. cooling of the core plasma, lasts about 0.5 ms for argon and mixtures of argon with deuterium and more than 1 ms for helium. The inward mixing of impurities during this stage accelerates the following current decay, which is known to be preferable for the reduction of the electromagnetic stresses due to halo currents. The current decay in argon experiments is almost 2 times faster than in helium experiments. In the case of low pressure ($p_w$ < 10 bar) argon injections the generation of runaway electrons carrying up to 25% of the initial plasma current is registered. Increase of the amount of injected argon suppresses runaway electrons.

Since runaway electrons are potentially the most dangerous consequence of a disruption in ITER, the generation of runaway electrons in TEXTOR experiments is analyzed in the framework of a 0D model. The model consists of equations for the plasma current, the

currents induced in the vessel, the generation of runaway electrons and the evolution of plasma thermal energy in coronal equilibrium. The main free parameters of the model are the density of deuterium and density of injected atoms. These parameters are chosen in such a way as to provide the best matching between the modeled current evolution and that measured experimentally. The analysis shows that the runaway electrons arise because of the incomplete inward mixing of atoms. The mixing efficiency is estimated to be 3% for pure argon injections, 15% for injections of argon mixtures and 40% for helium.

# Contents

# Chapter 1

# Introduction

Controlled realization of the fusion reaction

$$^2\mathrm{D} + ^3\mathrm{T} \rightarrow ^4\mathrm{He} + \mathrm{n} + 17.6\ \mathrm{MeV} \tag{1.1}$$

could probably satisfy the energy demands of the mankind. However "bringing the energy source of stars to the Earth" faces practical difficulties because of the high Coloumb threshold of the reaction. For the reaction to proceed at an appreciable rate the temperature of the medium should be about $\sim 10$ keV. It is confinement of such hot plasmas that is a major topic of research in the fusion community.

To provide a net energy gain the released fusion energy has to exceed the externally supplied plasma heating. The boundary situation when the fusion power is equal to the auxiliary heating is called break-even, the power multiplication factor $Q$ is then equal to 1. The ideal break-even is achieved if the following relationship between the plasma density $n_e$, energy confinement time $\tau^*$ and temperature $T_e$ is fulfilled (triple product): $n_e\tau^*T_e = 0.5 \cdot 10^{21}$ $\mathrm{m}^{-3}\cdot\mathrm{s}\cdot$ keV [1]. This condition is derived from the power balance between the external heating, heating by the fusion $\alpha$-particles and the energy losses due to bremsstrahlung radiation and transport. Since the temperature is in fact close to the optimal value of about 10 keV, one can distinguish two principal ways of achieving the energy gain: (i) high density pulse experiments (inertial fusion) and (ii) low density plasmas with long energy confinement times $\tau^* \gtrsim 1$ s (magnetic confinement).

Presently the most developed branch of the magnetic confinement, achieved values of the triple product, is the tokamak research. In a tokamak the plasma forms a closed ring and is confined by a magnetic field consisting of the toroidal $B_\phi$ and poloidal $B_p$ components. The toroidal field is imposed by currents in external coils, while the poloidal one results from the current $\vec{j}$ driven in the plasma by transformer.

The performance of tokamaks is restricted by a number of hard magnetohydrodynamic (MHD) limits. For example, it is common to express the fusion power $P_F$ in terms of the so called $\beta_t$:

$$P_F \sim \beta_t^2 B_t^4, \tag{1.2}$$

where $\beta_t$ is the ratio of the thermal pressure properly averaged over the plasma volume to the magnetic pressure, i.e. it shows the efficiency of confinement of plasma pressure by the magnetic field. The achievable $\beta_t$ is proportional to the plasma current $I$ (Troyon scaling) [2]. The maximum plasma current itself can not exceed the value given by the following condition on the edge safety factor:

$$q_a = \frac{L_p}{L_t} \cdot \frac{B_t}{B_p} > 2, \tag{1.3}$$

where $L_p$ and $L_t$ are the poloidal and toroidal circumferences correspondingly. One way of improving $\beta_t$ is to exploit elliptic shapes maximizing $L_p$ [3], i.e. to create the plasma elongation. Similarly, the achievable line average density is known to have limit referred to as Greenwald density $n_G([10^{20}\mathrm{cm}^{-3}]) = I_p/(\pi a^2)$ [MA/m$^2$] [4].

The operation close to the limits is advantageous from the point of view of performance, but uncontrolled termination of the plasma due to the growth of the instabilities becomes more probable. Even if the limits are avoided by a careful design of the operational scenario, the plasma can still be lost because of a failure of the control system. The uncontrolled plasma losses are called tokamak disruptions. In a course of a disruption two main stages may be distinguished. At first the thermal energy is lost on a sub-millisecond timescale, the so called thermal or energy quench. After the thermal quench the plasma is too cold ($T_e \sim 10$ eV) and contaminated by impurities to sustain the toroidal current, hence the current decays in a resistive way. In this phase referred to as current quench the magnetic energy is removed mainly by impurity radiation.

A disruption results not only in the termination of the ongoing discharge but is also able to damage the machine. Fast release of the thermal energy during the first stage leads to excessive heat fluxes that can reach a level of several GW$\cdot$m$^2$ and can cause a significant erosion of the wall components. In elongated plasmas loss of the vertical control is typical in a disruption and leads to excitation of halo currents. Halo currents are currents

flowing partially in a cold plasma along open field lines and passing through the vessel. Consequently the vessel is subjected to strong $\vec{j} \times \vec{B}$ forces. Moreover, high induced fields during the current decay can accelerate a beam of runaway electrons with energies of tens of MeV. A localized deposition of energy of runaway electrons on material surface can lead to a serious damage of the wall. These problems become especially severe in the future tokamak experiment ITER aiming at a fusion power of 500 MW. Disruptions in ITER, where the thermal energy will exceed 0.3 GJ and the full magnetic energy of the plasma current will approach 1 GJ, will limit the life time of the machine and will determine the availability of the reactor.

Since disruptions are inevitable, at least on an occasional basis, a technique of softening the machine damage is required. A successful mitigation technique has (i) to redistribute the heat fluxes over a large wall surface in the thermal quench, (ii) to accelerate the current decay relative to the growth time of vertical instability and/or to predominantly cool the halo region, so that the current transferred to the halo region is reduced (iii) and to prevent electrons from running away. All of that can be achieved by the injection of large amounts of impurities. The ways of delivering particles include pellet injections and massive gas injections.

Pellets are small pieces of material accelerated to a velocity of the order of 1000 $m \cdot s^{-1}$. Such pellets penetrate up to the center of a discharge due to the formation of a self-shielding cloud of ablated material. That is why they can relatively easily radiate the plasma thermal energy without triggering a disruptive phase with large scale instabilities. At the present time disruption mitigation experiments are concentrated on the study of physical basics and efficiency of particular methods. Therefore in almost all investigations the terminated discharges have been stable prior to the injection. It is generally observed that the injection of impurity pellets can significantly reduce the heat flux to the limiting surface (limiter/divertor). Similarly, halo currents and related forces are lowered. The only disadvantage of this method is the generation of runaway electrons because of a relatively small amount of additional electrons that can be introduced into the discharge by pellet injection. All of that along with an unclear scaling of the radial deposition profile of pellet particles make the success of this method in ITER questionable and calls for the development of alternative techniques, like massive gas injection by a fast valve.

In massive gas injection experiments impurities are delivered as a dense gas jet. Such plasma quenching by massive gas injection is the topic of this thesis. In the experimental part of this thesis it is shown that the injected particles are localized at the plasma edge before the onset of disruption. Such situation does not preclude the reduction of heat loads. Since the total number of introduced atoms is by orders of magnitude higher than in the case of pellet termination, it is hoped that the formation of runaway beams can be precluded.

It is known that massive gas injection reduces the halo currents and heat fluxes to the limiter/divertor. However, scaling of the mitigation effect was hardly possible as the dynamics of the injected atoms and the succession of events leading to the final collapse was poorly understood. In addition, for injections of heavy gases a strong population of runaway electrons is usually registered. A systematic investigation of the physical reasons for appearance of runaway electrons was lacking. These questions will be addressed in a systematic way for the first time in this thesis.

In the first part of this thesis the technique of massive gas injection is investigated. The valve developed at the Forschungzentrum Jülich is activated by eddy currents. Because of the immunity to high static and slow varying magnetic fields this valve is a good choice for tokamak applications. The study is based on the novel direct observation of the piston motion by means of a fast framing camera. The piston stroke and the injection duration are shown to depend strongly on the valve operational pressure and the working gas. The same is true for the valve throughput. The knowledge of the injection duration is used to deduce the pressure decay rates and the gas outflow rates that have remained unknown until now. The dependence of gas outflow rate on the piston stroke shows that the outflow rates can be increased by a factor of 4 by modifying the diameter of output orifice by a

factor of 2. The modified valve was machined and is currently in operation at TEXTOR. The gained understanding of the valve operation is an essential contribution for developing the valve for ITER.
Disruption mitigation experiments with the fast valve were conducted at TEXTOR. The unique ultra-fast framing camera system that is available at TEXTOR allows detailed and systematic studies of the impurities dynamics. Together with complementary diagnostics (ECE, Thomson scattering, soft X-ray camera) these data unambiguously reveal the phenomenology of the plasma quenching by massive gas injection. The shutdown scenario turns out to be disruptive.
In the analysis of the current quench it is shown that the inward mixing of impurities during the thermal quench accelerates the current decay rate, which is known to be preferable for the reduction of the electromagnetic stresses due to halo currents. However, in the case of low pressure ($p_w < 10$ bar) argon injections the number of atoms delivered to the core is relatively small and the generation of runaway electrons is registered. Increasing the number of injected atoms diminishes density of runaways: not only the generation of runaway electrons during disruptions but also their suppression by massive gas injection is demonstrated.
Since runaway electrons are potentially the most dangerous consequence of a disruption in ITER, the generation of runaway electrons in TEXTOR experiments is analyzed in the framework of a 0D model. For the first time such considerations are systematically applied to the generation of runaway electrons in the experiments on disruption mitigation by massive gas injection. The analysis shows that the runaway electrons arise because of the incomplete inward mixing of atoms.
In the rest of this chapter the general concepts related to the tokamak equilibrium, plasma elongation and the plasma stability are introduced. Chapter 2 gives systematization of different disruption types, theoretical description of the generation of halo currents and runaway electrons and a more detailed analysis of the loads associated with disruptions. A review of the existing disruption mitigation experiments is given at the end of chapter 2. In chapter 3 studies of the fast disruption mitigation valve and the short description of the main diagnostics are presented. The main experimental results concerning the disruption mitigation are described in chapter 4. The model explaining the generation of runaway electrons in these experiments is developed in chapter 5. Finally, the main conclusions are drawn in chapter 6. In the same chapter a short outlook is provided.

## 1.1 Tokamak

In a tokamak the plasma forms a closed ring of radius $R_0$, the radius of plasma cross section is $a$ (fig. 1.1). The magnetic field consists of the toroidal $B_\phi$ and poloidal $B_p$ components. The toroidal field is imposed by the currents in external coils, while the poloidal one results from the current $\vec{j}$ driven in the plasma by transformer. It is possible to show that if collisions are neglected the charged particles remain confined because of the compensated drifts [6]. Since particles move freely along the field, the confinement relies strongly on the "good" field lines that remain on the nested flux surfaces (fig. 1.1). The last facts can also be obtained from the consideration of the plasma equilibrium in the magnetohydrodynamic (MHD) approximation [7] (unless otherwise stated CGS units are used throughout the thesis, with $T$ being expressed in energy units):

$$\vec{\nabla} p = \frac{1}{c}\left[\vec{j} \times \vec{B}\right] \tag{1.4}$$

The plasma column in a tokamak tends to expand in the direction of major radius $R_0$ due to three reasons: (i) the force expanding a current ring $F = \partial W_{mag}/\partial R = (I^2/2c^2)\cdot\partial L/\partial R$; (ii) the pressure force $F = p\delta V/\delta R = 2\pi^2 a^2 p$; (iii) and the magnetic force appearing because of the external magnetic field being unequal to the internal one. To prevent plasma from moving horizontally the vertical field $B_z$ is applied. Its magnitude is found (either as the combination of the three mentioned forces [6] or from the MHD solution [7]) to be proportional to

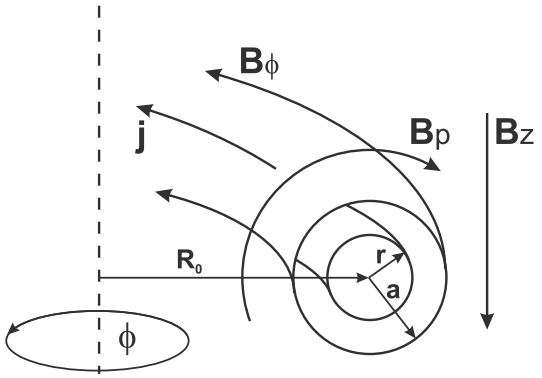


Figure 1.1: Tokamak

the plasma current $I$:

$$B_z = -\frac{I}{cR_0}\left(\ln\left(\frac{8R_0}{a}\right) + \beta_p + \frac{\ell_i}{2} - \frac{3}{2}\right), \tag{1.5}$$

where $\beta_p = \int pdS/(B_p(a)^2/(8\pi))$ is poloidal beta.
The main parameters of the tokamak TEXTOR in which the experimental part of the present work was performed are given in table 1.1 in comparison with the parameters of the next step experiment ITER.

## 1.2 Elongated plasma

To achieve a better performance of a tokamak it turns out to be favorable to create a vertical elongation. In particular, since in the range of interest $\langle\sigma v\rangle \sim T^2$ the thermonuclear power is proportional to $p^2$ or to $\beta_t^2 \cdot B_t^4$. Where $\beta_t$ is introduced as

$$\beta_t = \frac{\left\langle p^2\right\rangle^{1/2}}{B_t^2/8\pi)} \tag{1.6}$$

The achievable $\beta_t$ is limited by the plasma stability, which is described by the Troyon scaling [2] on $\beta_t$ and the condition on the edge safety factor $q_a$:

$$\beta_t < C_\beta^* \cdot I \tag{1.7a}$$

$$q_a = \frac{L_p}{L_t} \cdot \frac{B_t}{B_p} = \frac{cL_p^2}{8\pi^2 R_0} \cdot \frac{B_t}{I} > 2, \tag{1.7b}$$

| Parameter | TEXTOR [8] | ITER [9] |
|---|---|---|
| Major radius $R_0$, m | 1.75 | 6.2 |
| Minor radius $a$, m | 0.46 | 2.0 |
| Magnetic field $B_\phi$, T | 3 | 5.3 |
| Plasma current, MA | 0.8 | 15 |
| Pulse length, s | 10 | > 400 |
| Auxiliary heating, MW | 9 | 73 |
| Elongation | 1 | 1.86 |
| Triangularity | 0 | 0.5 |
| Power multiplication $Q$ | – | 10 |

Table 1.1: Main parameters of the TEXTOR and ITER tokamaks

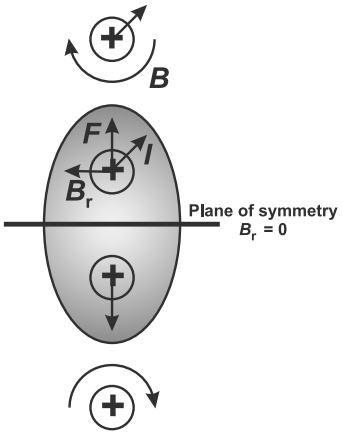


Figure 1.2: Plasma elongation. Plasma is elongated by two coils with parallel current.

where $L_p$ and $L_t$ are the poloidal and toroidal circumferences correspondingly. The way of improving $\beta_t$ while keeping constant the inverse aspect ratio $A = a/R_0$ is to exploit noncircular, e.g. elliptic, shapes maximizing $L_p$ [3]. The effect of $\beta_t$ scaling with the elongation has been observed experimentally [10, 11].

Vertical elongation can be created by two coils carrying current in the direction of the plasma current, fig. 1.2-1. Indeed, above the plane of symmetry current elements are drawn upwards, while below the plane they are drawn downwards. It is obvious that the illustrated equilibrium is unstable. If the plasma column obtains an accidental vertical shift the destabilizing radial field will increase. Under certain circumstances this instability results in high electromagnetic loads on the vessel. For this reason a simplified model of this process is considered in section 2.2. In practice more complicated coil configurations can be used. Nevertheless, the situation remains unstable [13].

## 1.3 Plasma stability

It is growth of instabilities that determines an operational regime and applicability of a particular confinement scheme. The topic of plasma stability is immense and ranges from the kinetic to magnetohydrodynamic scales. Some modes lead to the full termination of plasmas, while the others have soft character and only degrade the performance. Here only classical concepts of the large scale MHD instabilities are introduced.

Among MHD modes the ideal ones have the fastest growth rates and are potentially the most dangerous. The evolution of perturbations in ideal MHD, i.e. for a perfectly conducting plasma $\eta = 0$, is described by the following system linearized about the equilibrium point with zero velocity [14]:

$$\rho_0 \frac{\partial \vec{v_1}}{\partial t} = \frac{1}{c}\vec{j_1} \times \vec{B_0} + \frac{1}{c}\vec{j_0} \times \vec{B_1} - \vec{\nabla} p_1 \tag{1.8a}$$

$$\frac{\partial \rho_1}{\partial t} = -\vec{\nabla} \cdot (\rho_0 \vec{v_1}) \tag{1.8b}$$

$$\frac{\partial p_1}{\partial t} = -\gamma p_0 \vec{\nabla} \cdot \vec{v_1} - \vec{v_1} \cdot \vec{\nabla} p_0 \tag{1.8c}$$

$$\vec{\nabla} \times \vec{B_1} = \frac{4\pi}{c}\vec{j_1} \tag{1.8d}$$

$$\frac{\partial \vec{B_1}}{\partial t} = \vec{\nabla} \times [\vec{v_1} \times \vec{B_0}] \tag{1.8e}$$

where subscript 0 refers to the equilibrium state, subscript 1 designates perturbations and suitable boundary conditions are applied. Introducing displacement $\vec{\xi}$ one can reduce the system to the equation (for the explicit expression see section A):

$$\frac{\partial^2 \vec{\xi}}{\partial t^2} = \vec{F}(\vec{\xi}) \tag{1.9}$$

Because of the linearity the vector $\vec{\xi}$ can be decomposed into Fourier components $\exp(-i\omega t)$. The operator $\vec{F}$ turns out to be self-adjoint, consequently the values of $\omega^2$ are real [14, 15]. In the case $\omega^2 > 0$ the eigenmode corresponds to a stable oscillation, while negative $\omega^2$ results in instability.

To find out stability properties of the equilibrium it is not necessary to find all solutions of the eigenvalue equation. A complementary way is to consider the so called energy principle [15]. The potential energy of a perturbation is (section A):

$$\delta W = -\frac{1}{2}\int \vec{\xi}\cdot\vec{F}\,dV = \frac{1}{2}\int\left(\gamma p_0(\vec{\nabla}\cdot\vec{\xi})^2 + +\frac{1}{4\pi}B_1^2 + (\vec{\xi}\cdot\vec{\nabla}p_0)\cdot(\vec{\nabla}\cdot\vec{\xi}) + \frac{1}{c}\vec{j_0}\cdot\left[\vec{\xi}\times\vec{B_1}\right]\right)dV+$$
$$+\frac{1}{8\pi}\int_{vac} B_{v1}^2\,dV + \frac{1}{2}\int\left(\frac{1}{8\pi}\frac{\partial B_{v0}^2}{\partial n} - \frac{1}{8\pi}\frac{\partial B_0^2}{\partial n} - \frac{\partial p_0}{\partial n}\right)\xi_n^2\,dS \tag{1.10}$$

Similar to the usual mechanics [16], if there is an allowed displacement that casts a negative value of this potential energy, the equilibrium is unstable. The energy sources of the instabilities, i.e. the terms that can be negative, are related to the pressure gradient and current. The corresponding modes appearing in tokamaks will be listed later.

In the case of cylindrical symmetry the eigenmodes have the form $\exp(im\theta + ikz)$, where $\theta$ is poloidal angle. In toroidal geometry the situation is more complicated and interaction of modes known as mode coupling takes place. However, to understand the main structure of instability it is common to identify modes as $m/n$, $m$ and $n$ being the poloidal and toroidal mode numbers. The associated displacement has the form $\sim \exp(im\theta - in\phi)$. Such an approach is justified for a torus with large aspect ratio $R_0/a$.

Even if the plasma is predicted to be stable in ideal MHD approximation, it can be unstable because of resistive effects. These are usually paired with types of ideal modes since the energy source of energy is still available when the constraint of perfect conductivity is relaxed [17].

The most pronounced tokamak modes are the following ones [17]:

- Kink mode. The mode is driven by the gradient of the toroidal current. It results in kinking of the magnetic surfaces and plasma boundary. The necessary condition for the stability of the mode is that its resonance surface lyes in plasma $m/n < q_a$, where $q_a$ is the edge safety factor. It is violation of this criterion that is thought to be responsible for the plasma current boundary $q_a > 2$ found in experiments.
- Tearing mode. The mode is a resistive counterpart of the kink mode and is driven by the radial gradient of the toroidal current. The mode appears as an island around the resonant flux surface $q(r) = m/n$.
- Ballooning mode. This mode is localized at the low field side and is driven by the pressure gradient. It develops if the pressure gradient is high enough to deform magnetic field lines in such way that the perturbation is localized to the outer side of the torus with adverse field curvature.

Note that a special role in plasma stability is played by the safety factor:

$$q(r) = \frac{L_p(r)}{L_t}\cdot\frac{B_t}{B_p(r)} = \frac{r}{R_0}\cdot\frac{B_t}{B_p(r)} \tag{1.11}$$

The dynamics of tokamak plasmas in the unstable region is governed by a non-linear evolution of instabilities. In many cases the modes mentioned above lead to an uncontrolled

termination of discharge. Because of the abrupt energy release such termination called disruption is potentially dangerous for the machine. This thesis is devoted to a possible softening of the disruption loads by massive gas injection.

# Chapter 2

# Disruptions

A disruption is an uncontrolled loss of the full stored plasma energy on a millisecond timescale. Sequence of events taking place during this process is considered. Special emphasis is placed on the consequences of a disruption and a need for a mitigation technique. The review of existing mitigation experiments is given in place. Aims of the work are formulated at the end of the chapter.

## 2.1 Disruptions

A disruption is a complex process in which the whole thermal and magnetic energy of the plasma is lost on a relatively short timescale. It usually develops as a result of operation at extreme plasma parameters or due to technical failures.
In a course of a disruption two main stages may be distinguished. At first the thermal energy is lost on a sub-millisecond timescale - thermal or energy quench (hereafter TQ). Sometimes the final energy quench is preceded by precursor prominent through slow instability growth in hundreds of milliseconds. If this period does exist the instability sooner or later reaches critical amplitude and stops rotating: it locks to the wall. Having locked the instability grows even faster and finally leads to the energy quench. The last transition can itself consist of several minor disruptions flattening the temperature profile [18]. After TQ the plasma is too cold ($T_e \sim 10$ eV) and dirty to sustain current, hence the current decays in a resistive way - current quench (hereafter CQ), with the magnetic energy being mainly removed by impurity radiation. One should also mention that at transition from TQ to CQ plasma current always experiences transitive spike just prior to its decay. This spike is caused by flattening of current density profile by some large scale instability. Flat current profile has lower inductivity $L$ as compared to the peaked configuration, which provokes positive increment of the total plasma current $I$ in accordance with the conservation of magnetic energy $LI^2/2$.
Schüller proposed classification of disruptions on basis of the underlying physical mechanism. He specified two main categories: (i) edge deficiency disruptions and (ii) $\beta$-limit like disruptions [19]. (i) In the first case thermal quench usually takes place in two stages separated by a quiet phase. At the beginning the plasma outside of $q = 2$ is cooled. Consequently the current in that region almost disappears creating favorable conditions for the abrupt growth of the 2/1 tearing mode. In addition peaking of the current profile allows the 1/1 island to grow. The toroidal coupling of 2/1 and 1/1 modes facilitates their locking. Locked modes swiftly redistribute thermal energy inside of $q = 2$. This is what constitutes the first observed stage of edge deficiency disruptions [19]. The second stage bringing plasma to very low $T_e$ and initiating CQ is poorly understood. Ward and Wesson suggested strong impurity influx from the wall to be responsible for the final crash [20]. (ii) Thermal quench in the $\beta$-limit like disruptions is less complicated and occurs in a single stage. These events are attributed to development of ideal kink and ballooning modes without distinct precursor [19]. It is to be noted that described qualitative classification does not reveal the internal complexity of the phenomena responsible for the fast radial heat transport and appearance of the positive current spike. The possible explanation is nonlinear development of low $m/n$ number modes (resistive/ideal) resulting either in reconnection and stochastization of magnetic lines [21, 22] or in capture of the cold plasma bubble from periphery [23].
In practice it is more common to categorize disruptions on basis of the responsible operational parameter (the list does not pretend to be complete):

- Density limit. The achievable line average density is known to have limit referred to as Greenwald density $n_G([10^{20}\mathrm{cm}^{-3}]) = I_p/(\pi a^2)$ [MA/m$^2$] [4]. Processes at the limit are complex and can include: MARFE formation, detachment, H/L transition, current channel contraction, growth of MHD instabilities, a series of minor disruptions and final crash [24, 25]. In many cases poloidally localized radiating zone having low $T_e$ and high $n_e$ and impurity concentration is observed at densities $n_e = (0.4 - 1) \cdot n_G$. This zone of energy sink is called MARFE (multifaceted asymetric radiation from the edge). Just before the collapse, $n_e \approx (0.8 - 0.95) \cdot n_G$, the H-mode discharges degrade back to L-mode. At the highest densities region of cold radiating plasma expands to the core region forming poloidally symmetric mantle. In most cases such situation is unstable, as a consequence the temperature profile shrinks and growing MHD activity is observed. After maybe few minor disruptions and as soon as the edge safety factor $q_{95}$ drops to 2 the thermal quench takes place [18, 26].
- $q_a = 2$ limit. If the edge safety factor decreases to 2 plasma becomes unstable with

respect to the 2/1 kink/tearing mode [17]. The mode leads to a disruption on a timescale of $10-20$ ms [18].

- Low density locked-mode. This type of disruption is found at densities so much lower than the Greenwald one as to make plasma screening of the error fields produced by slight misalignments of magnetic coils ineffective. As a result low number mode (most probably the 2/1 mode) is created, which finally triggers a disruption [26, 19]. Schüller attributes this disruption to the edge deficiency class, with the edge being cooled by convection.

- $\beta$-limit. The maximum achievable $\beta$ is limited according to Troyon scaling $\beta_t < C^*_\beta \cdot I_{pl}/(aB)$ [2]. If in addition to high $\beta$ the edge safety factor $q_{95}$ is less than 3 disruption is initiated. At higher values of $q_{95}$ the limit is soft and degrades the discharge [27]. The main role in restricting the achievable $\beta$ is played by ideal kink and ballooning modes [11].

- Internal transport barrier (ITB) disruptions. As the name suggests in ITB discharges heat and particle transport is strongly reduced at some point in the core part of the plasma. These regimes studied with the aim of improvement in confinement time $\tau$, temperatures $T_e$, $T_i$, energy $\beta$, stability are achieved by combined optimization of $\vec{E}\times\vec{B}$ shear flows and magnetic shear $s = (r/q)\cdot(dq/dr)$. To create transport barrier the magnetic shear should be either close to 0 or even negative (non-monotone q-profile), with such configuration being stabilized against sawtooth oscillations and NTM modes. However the strong pressure gradient at the position of the barrier excites ideal kink or ballooning low-$n$ modes or their combination also known as infernal-kink mode, which disrupts the plasma and limits the achievable peak pressure [28]. Because of the ideal nature and proximity of the provoked mode to the main energy reservoir, this type of disruption is characterized by fast time scales and preservation of high thermal energy content up to the final quench [29].

- Vertical displacement event (VDE). In vertically elongated configurations the vertical position of the plasma has to be stabilized by a feedback. In the case of accidental control loss the plasma column drifts toward the wall. As soon as the $q \approx 2$ surface is scraped-off the plasma is terminated [19, 30]. The type of VDE described above is often referred to as hot VDE. In general, vertical instability can arise after thermal quench of other disruption types, so that current channel moves towards the wall during current decay. Since this instability results in dramatic increase of the electromagnetic forces exerted on the vessel the conditions of its appearance and its consequences are considered in detail in sections 2.2 and 2.4.2 correspondingly.

- Fast impurity penetration. Sometimes melted pieces of in-vessel structures called UFOs penetrate deeply into plasma and cause disruption.

Disruptions lead not only to the termination of the ongoing discharge but also cause stresses on the machine in the form of: excessive heat loads, electromagnetic forces and runaway electrons generated in high electric fields during current quench. To elucidate the physical side of the problem these aspects are considered in what follows. As it has been already mentioned section 2.2 is devoted to the vertical displacement events responsible for large electromagnetic forces. Section 2.3 deals with the runaway electrons theory to be extensively used in analyzing the data in the thesis. And in section 2.4 data on stresses imposed in a disruption are briefly summarized.

## 2.2 Vertical displacement event

The magnetic fields required to provide a favorable vertical elongation give rise to an unstable configuration. As the plasma moves from the plane of symmetry the attracting radial field increases (fig. 1.2). The typical time scale of this instability depends on the used elongation and the electrodynamic coupling of the plasma to vessel: eddy currents induced in the vessel retard the plasma motion. If the induced currents are able to stabilize the plasma the instability develops on the vessel resistive timescale $\tau_v = L_v/R_v$. In the opposite case the instability is limited to tens of microseconds by a very small plasma inertia. Such disadvantageous configurations are usually excluded by a proper design of the vessel or by introducing some passive stabilizing loops [31], e. g. ITER was designed to have vertical displacement growth timescale of the order of 1 s [32].
Let's consider a simplified model of the vertical plasma motion with the good coupling to vessel. The process is described by the following equations linearized around the equilibrium point (SI units are used in this section[1]):

$$m_{pl} \cdot \frac{d^2 z}{dt^2} = -2\pi R_0 \cdot I_{pl} B_r \tag{2.1a}$$

$$L_v \cdot \frac{dI_v}{dt} + R_v I_v + \frac{dM_{vp}}{dz}\frac{dz}{dt} \cdot I_{pl} = 0 \tag{2.1b}$$

where $z$ is the vertical position and $m_{pl}$ is mass of the plasma. For the full list of the used symbols see section D.
The radial magnetic field consists of the equilibrium destabilizing field and of the retarding field of induced currents. The equilibrium component is usually introduced in the form of the so called decay index $n$ (note that in the plane of symmetry the radial field is absent $B_r(z=0)=0$):

$$n = -\frac{R_0}{B_z} \cdot \frac{dB_z}{dR} \tag{2.2}$$

$$rot\ \vec{B} = 0 \Leftrightarrow \frac{dB_{r,eq}}{dz} = \frac{dB_z}{dR} \Leftrightarrow B_{r,eq} = -n \cdot \frac{B_z(0)}{R_0} \cdot z = \frac{\mu_0 I_{pl} \Gamma n z}{4\pi R_0^2}, \tag{2.3}$$

where $B_z(0)$ is the vertical field found from the equilibrium requirements, $\Gamma = \ln(8R_0/a) + \beta_p + (\ell_i - 3)/2$ (see eq. 1.5 and its discussion). The field created by the eddies can be found from the expression for the acting force $F = \partial W_{mag}/\partial z$ [33, 34]:

$$W_{mag} = \frac{L_{pl} I_{pl}^2}{2} + \frac{L_v I_v^2}{2} + M_{vp} I_{pl} I_v \tag{2.4}$$

$$F = \left(\frac{\partial W_{mag}}{\partial z}\right)_{I=\text{const}} = I_{pl} I_v \cdot \frac{dM_{vp}}{dz} = 2\pi R_0 \cdot I_{pl} B_{r,ind} \Rightarrow B_{r,ind} = -\frac{I_v}{2\pi R_0} \cdot \frac{dM_{vp}}{dz} \tag{2.5}$$

where $W_{mag}$ is the magnetic energy of the system embracing the plasma filament and vessel and a proper sign was written in the final expression for $B_{r,ind}$.
Plasma inertia can be safely neglected as introducing no new phenomena in the region of interest [35]. The assumption of massless plasma requires force balance or equivalently zero total radial magnetic field (prime stands for $z$-derivative):

$$\frac{dz}{dt} = \frac{2M'_{vp} R_0}{\mu_0 I_{pl} L_{pl} n} \cdot \frac{dI_v}{dt} \tag{2.6}$$

To simplify the expression the critical index $n_{cr}$ standing for the coupling between the plasma and wall is introduced:

$$n_{cr} = \frac{2\left(M'_{vp}\right)^2 R_0}{\mu_0 L_{pl} L_v} \tag{2.7}$$

[1] SI units are more convenient and are commonly used in considering the problems related to electrical circuits

With the last substitution the equation of system evolution takes the form:

$$\left(1 + \frac{n_{cr}}{n}\right) \cdot \frac{dI_v}{dt} + \gamma_v I_v = 0, \tag{2.8}$$

where $\gamma_v = R_v/L_v$. The solution is exponential function having the growth rate $\gamma$ related to the vessel resistive time $1/\gamma_v$ by:

$$\gamma = -\frac{\gamma_v n}{n + n_{cr}} \tag{2.9}$$

Remembering that $n < 0$ one sees that as the decay index approaches $-n_{cr}$ the instability growth rate increases. If the decay index becomes less than $-n_{cr}$ this mode is stabilized, however the other modes not considered here start to go up on a much faster inertia time scale making the plasma control impossible [35]. Consequently tokamaks are operated in the region $n > -n_{cr}$, with the aid of the feedback stabilization reacting on the change of the plasma position and the velocity of that change. The analysis of feedback control that is supported by the achieved experimentally $n/n_{cr} = -0.9$ is given, for example, in [35].
Under certain circumstances the stabilization principles fail leading to a plasma motion towards the wall: a vertical displacement event (VDE) takes place. The most prominent situation when feedback can not cope with the position control is a disruption. The fraction of disruptions in elongated plasma that are accompanied by VDEs is fairly high [31, 36]. During current quench the instability can develop even faster than derived above due to the attracting eddy currents induced by the current decay. To account for the reducing current one has to fix the elongating field at the initial value, since the control system usually can not follow such fast changes, and to include eddy currents excited by dI/dt. Having been transformed the system of equations 2.1 becomes:

$$\frac{dz}{dt} = \frac{2M'_{vp}R_0}{\mu_0 I_{pl}(0)L_{pl}n} \cdot \frac{dI_v}{dt} \tag{2.10a}$$

$$L_v \cdot \frac{dI_v}{dt} + R_v I_v + \frac{dM_{vp}}{dz}\frac{dz}{dt} \cdot I_{pl} + \frac{dM_{vp}}{dz} z \cdot \dot{I}_{pl} = 0 \tag{2.10b}$$

With assumption of exponential plasma current evolution $I_{pl} = I_{pl}(0)\exp(-\gamma_I t)$ the final equation following from this system is:

$$\cdot\left(1 + \frac{n_{cr}}{n} \cdot e^{-\gamma_I t}\right)\frac{dI_v}{dt} + I_v \cdot \left(\gamma_v - \frac{n_{cr}}{n} \cdot \gamma_I \cdot e^{-\gamma_I t}\right) = 0 \tag{2.11}$$

At certain time the coefficient before the first term disappears making the approximation of massless plasma to be invalid, i. e. the plasma motion remains limited only by its inertia. The time for the plasma to become "completely" unstable is:

$$\tau = \frac{1}{\gamma_I} \cdot \ln\left|\frac{n_{cr}}{n}\right| \tag{2.12}$$

For the typical CQ time scale $1/\gamma_I \approx 10$ ms and strong elongation $n = -0.9n_{cr}$ this time is of the order of 1 ms. The reason for such behaviour is evident: the stabilizing force $F_{st} \sim I_{pl}I_v \sim I_{pl}^2$ decays faster than the destabilizing one $F_{dest} \sim I_{pl}B_z \sim I_{pl}I_{pl}(0)$ [31]. To prevent instability from falling into Alfvén domain the shaping fields are usually switched off as soon as a disruption is foreseen.
There can be two main reasons for the initial plasma displacement in a disruption. (i) After thermal quench internal inductance $\ell_i$ and plasma pressure $\beta$ drop, so that the vertical field balancing the plasma current and pressure hoop force is higher than required for a new equilibrium (eq. 1.5). This drop results in plasma shifting inwards and vertically. Resembling as it does the vertical motion the horizontal one is different because of the field $B_z$ descending with decreasing major radius. The growth rate of a VDE at lower major radii is higher because of the more favorable field curvature and reduced stabilizing force (the main part of stabilizing currents flow at the outboard side of the vessel) [36, 37].

Even more the eddies retarding the horizontal motion of the plasma degrade the decay index [37]. (ii) The other mechanism is due to the vessel asymmetry. If the vessel has an up-down asymmetry the eddy currents excited by the decaying plasma current are not balanced, which drags the column towards the prevailing side.
Provided the plasma current quench is sufficiently slow $\sim 100$ ms and the discharge is operated close to the neutral point, i. e. the point of the vessel symmetry, the last mechanism can be suppressed, as it has been shown in JT-60U [38, 39, 40]. It is to be noted here that the current decay rate in natural disruptions is uncontrolled. The situation is even more complicated in diverted tokamaks, where the divertor currents in single null configuration are de facto asymmetrical and flattening of the current profile initiate a VDE, as observed in ASDEX Upgrade [41]. The attraction being strongly dependent on the degree of profile flattening, an universal correction of the neutral point is almost impossible. Furthermore the plasma can be non-rigid in contrast to what has been assumed above. Deformations appear especially at high elongations and decrease the efficiency of the stabilization system [42, 43].
A better way of dealing with the VDE could be an acceleration of the CQ, which can be achieved for example by injection of impurities. Very fast decaying currents were observed to experience primarily inward shift, in JT-60U the fast CQs are those with $\tau_{CQ} < 20$ ms [39]. However it is not clear why such plasmas do not drift vertically.
VDEs are dangerous because they impose large forces by driving halo currents. Halo currents are currents flowing partially in a cold plasma and passing through the vessel, see section 2.4.2. These currents provide stabilizing force slowing the VDE down [31, 44].
VDE can develop without a preceding disruption (hot VDE) either as a result of fast plasma parameters change, $\ell_i, \beta$, elongation, or simply because of the feedback system failure, for phenomenology of hot VDEs see section 2.1. Besides being responsible for large forces on the machine this type of VDE leads to excessive heat loads especially to the unprotected regions outside of the divertor. They are considered to be unacceptable in ITER and in the case of their initiation the plasma should be safely terminated faster than in 1 s [22].

## 2.3 Runaway electrons

A runaway particle is a particle whose energy exchange with surrounding ions and electrons is negligible in comparison with the applied electric force so that its energy continually grows. The question of running away particles was for the first time considered in two fluid approximation by Dreicer [45]. It was found that if the applied electric field was stronger than some critical value $E_D$ the drift velocities of ions and electrons grew infinitely making the usual conductivity theory inapplicable. The critical field $E_D$ is the electric field required for a particle moving with an average thermal velocity to gain between two collisions momentum comparable to the thermal one $v_T = \sqrt{T_e/m}$:

$$\frac{eE_D}{\nu} = \frac{eE_D}{n\sigma_{tr}v_T} = mv_T \Leftrightarrow E_D = \frac{n\sigma_{tr}T_e}{e} \tag{2.13}$$

where $\nu = n\sigma_{tr}v_T$ is collision frequency. Using Rutherford transport cross section $\sigma_{tr} = 4\pi e^4 \ln\Lambda/T_e^2$ upon rearranging one finds:

$$E_D = \frac{4\pi e^3 n \ln\Lambda}{T_e} \tag{2.14}$$

This so called Dreicer field differs by a factor of 2 from that introduced by Dreicer himself. Because of the high electric conductivity, electric fields found during tokamak operation are usually much smaller. Indeed, even in the current quench phase characterized by high induced field $E \sim L/(2\pi R_0)\cdot dI/dt \sim \mu_0 I/(2\pi\tau) \sim 10 \div 100$ V·m$^{-1}$ the value of $E_D$ is more than 1000 V·m$^{-1}$.
The case of vital importance $E \ll E_D$ was also treated by Dreicer [46]. Even in such a weak electric field there always exists a group of particles running away. Dreicer derived an approximate rate of the runaway population growth by solving the Fokker-Planck equation for electrons:

$$\frac{\partial f_e}{\partial t} - \frac{\vec{E}}{E_D}\cdot\nabla_v f_e = -\frac{\partial}{\partial v_k}\left(f_e\cdot\left(\frac{\partial h_{ee}}{\partial v_k}+\frac{\partial h_{ei}}{\partial v_k}\right)\right) + \frac{1}{2}\cdot\frac{\partial^2}{\partial v_k\partial v_j}\cdot\left(f_e\cdot\left(\frac{\partial^2 g_{ee}}{\partial v_k\partial v_j}+\frac{\partial^2 g_{ei}}{\partial v_k\partial v_j}\right)\right) \tag{2.15}$$

Electron-electron and electron-ion collisional terms were taken from [47]:

$$h_{e\alpha} = \Gamma_e\frac{m_e+m_\alpha}{m_\alpha}\cdot\int f_\alpha(\vec{v}')\left|\vec{v}-\vec{v}'\right|^{-1}d^3v' \tag{2.16a}$$

$$g_{e\alpha} = \Gamma_e\int f_\alpha(\vec{v}')\left|\vec{v}-\vec{v}'\right|d^3v' \tag{2.16b}$$

$$\Gamma_e = \frac{4\pi e^4\ln\Lambda}{m_e^2} \tag{2.16c}$$

The solution was obtained in the two term approximation, i.e. the distribution function differs only slightly from a spherically symmetrical one. With $z$ axis antiparallel to $\vec{E}$ this expansion assumes the form:

$$f(\vec{v},t) \approx f_0(v,t) + cos\theta\cdot f_1(v,t), \tag{2.17}$$

where part $f_1$ represents runaway contribution and angle $\theta$ is relative to $z$ axis.
The main conclusion has a clear physical explanation. The energy gained between two collisions by a particle moving with velocity $v$ is:

$$\delta v \sim \frac{eE}{mvn\sigma_{tr}(v)} \sim \frac{mv^3E}{4\pi e^3 n\ln\Lambda} \sim \frac{mv^3}{T_e}\cdot\frac{E}{E_D} \tag{2.18}$$

If the gained velocity is comparable to its initial value a particle runs away, since a collision consumes only about thermal velocity. The "critical" velocity is:

$$v_c = \left(\frac{T_e}{m}\right)^{1/2}\cdot\left(\frac{E_D}{E}\right)^{1/2} \tag{2.19}$$

The estimation of the critical velocity on basis of the average particle equation indicates an additional weak factor of $(Z+2)^{1/4}$ [48] . The number of runaway particles grows due to the diffusion of thermal particles in the velocity space towards the critical value $v_c$. In that case the task is to calculate the flux of particles across the critical boundary.
A quantitative theory was developed by Gurevich [49] who considered the kinetic equation for fast electrons in dimensionless variables:

$$u = \frac{v}{\sqrt{T_e/m}} \tag{2.20a}$$

$$\tau = t \cdot \nu_{ee}(T_e/m) \tag{2.20b}$$

$$\mu = \cos\theta \tag{2.20c}$$

$$\frac{\partial f}{\partial \tau} + \frac{E}{E_D}\left(\mu\frac{\partial f}{\partial u} + \frac{1-\mu^2}{u}\frac{\partial f}{\partial \mu}\right) - \frac{1}{u^2}\frac{\partial}{\partial u}\left(\frac{1}{u}\frac{\partial f}{\partial u} + f\right) - \frac{1}{u^3}\frac{\partial}{\partial \mu}\left((1-\mu^2)\frac{\partial f}{\partial \mu}\right) = 0 \tag{2.21}$$

This equation can be directly derived from the general kinetic equation with collisional integral written in Landau form (section B.1). Firstly the steady state solution of equation 2.21 was found, with $f = \exp(\phi(u,\mu))$ and $\phi$ being expanded in series of $\mu - 1$: $\phi(u,\mu) = \phi_0(u) + (\mu-1)\phi_1(u) + (\mu-1)^2\phi_2(u) + \ldots$ (in fact only first order in $(\mu-1)$ was considered). Afterwards, the non-stationary equation was considered in cylindrical coordinates $z \uparrow\downarrow E$:

$$\frac{\partial F}{\partial \tau} - \frac{\partial}{\partial u_z}\left(\frac{1}{u_z^2}\left(3 - \frac{E}{E_D}u_z^2\right)F + \frac{1+\bar{u_r^2}}{u_z^3}\frac{\partial F}{\partial u_z}\right) \tag{2.22}$$

Small terms $u_r/u_z$ were neglected in deriving the last equation. $F(u_z,\tau) = 2\pi\int f u_r du_r$ is distribution function relative only to $z$ component of velocity. Value of $\bar{u_r^2}$ being dependent on $u_z$ was evaluated from the found stationary distribution function $f_{st}$:

$$\bar{u_r^2} = \frac{\int_0^\infty u_r^3 f_{st} du_r}{\int_0^\infty u_r f_{st} du_r} \tag{2.23}$$

The non-stationary equation was solved by using results for general statistical acceleration mechanism developed by the same author earlier [50]. The idea of the method is to divide the velocity space into three regions. In the first region, the acceleration mechanism is of minor importance and the distribution function changes only due to the streaming away of particles. In the small second region, deceleration by collisions and the acceleration are comparable, the flux through this region was assumed to be constant and equal to the outflux of particles from the first region. And in the last part, the acceleration dominates. On combining solutions from all regions with correct normalization Gurevich found the desired growth rate of number of runaway electrons [49]:

$$S = \frac{2}{\sqrt{\pi}} n_e \nu_{e0}\left(\frac{E}{E_D}\right)^{1/2} \exp\left(-\frac{E_D}{4E} - \sqrt{2}\left(\frac{E_D}{E}\right)^{1/2}\right), \tag{2.24}$$

where $\nu_{e0}$ is collisional frequency at thermal velocity $\nu_{e0} = \nu_{ee}(T_e/m)$. The result holds for $E \leq 0.1E_D$ as it follows from the time necessary to form the quasi-stationary flux $\tau \geq (E_D/E)^{3/2}\nu_{e0}^{-1}$ and requirement of the weakness of the acceleration mechanism, i. e. the amount of electrons running away in time $\tau$ should be much less than the number of bulk thermal electrons [49]. Remembering earlier mentioned disruption values of electric fields one observes a good fulfilment of the given criterion.
Strictly speaking, the solution found by Gurevich is not completely consistent. Namely the stationary distribution function satisfying equation 2.21 was obtained for small $u$ only, which automatically means inaccurately calculated $\bar{u_r^2}$. Having considered this equation in two limiting cases Lebedev refined the distribution function and the runaway rate defined as [51]:

$$S = \lim_{y\to\infty} \frac{2\pi v^2 eE}{m} \int_{-1}^{+1} f(y,\mu) d\mu, \tag{2.25}$$

where $y = u^2/u_{th}^2$. The formula expresses flux in the velocity space through a sphere of radius $v^2$ under the action of acceleration $eE/m$. To calculate runaway production rate this flux is to be determined at $v_c$ however in the case of a weak electrical field being analyzed here the expression can be estimated in the limit. The final result reads:

$$S = 2^{-1/6}\pi^{-1/2} n_e \nu_{e0} \left(\frac{E_D}{E}\right)^{1/4} \exp\left(-\frac{E_D}{4E} - \sqrt{2}\left(\frac{E_D}{E}\right)^{1/2} - \frac{1}{2}\right) \tag{2.26}$$

The difference appears in the preexponential factor.
An alternative approach to the problem was followed by Kruskal and Berstein. Unfortunately their work has never been published. The sense of the method was described and generalized by Cohen [52]. The solution was sought in series of the small parameter $E/E_D$. To do so the whole velocity space was subdivided into 5 regions, with suitable conditions applied at the boundaries. It was not possible to determine the analytical solution for all regions and the preexponential constant remained unknown ($\zeta \equiv (Z+1)/2$, $Z \equiv \langle Z^2 \rangle$ see section B.2):

$$S = C \cdot n_e \nu_{e0} \left(\frac{E_D}{E}\right)^{3\zeta/8} \exp\left(-\frac{E_D}{4E} - \sqrt{2\zeta}\left(\frac{E_D}{E}\right)^{1/2}\right) \tag{2.27}$$

From comparison of numerical simulations with the analytical expression $C \approx 0.35$ follows for $Z = 1$ and $E \leq 0.1E_D$ [53], dependence of $C$ on $Z$ is discussed in [52]. The transient time for the flux to set in is of the same order $(E_D/E)^2$ as for Gurevich's solution [53]. In [52] it was also pointed out that it was possible to bring Lebedev's formula in agreement with numerical simulations by adjusting the preexponential factor as in the case of equation 2.27.
The law 2.27 was confirmed experimentally [54]. For this reason, it is taken as a runaway generation rate for the primary mechanism in this work (section 5). However, it is to be noted that the associated error bars are as large as one order of magnitude [54].

### 2.3.1 Relativistic correction

As it has been shown in the previous section, when a weak electric field $E << E_D$ is applied to the plasma, at the tail of the distribution function $v > v_c$ (eq. 2.19) the collision frequency of electrons is unable to compensate acceleration by electrical field. In a very weak field the critical velocity becomes comparable to the light speed $c$ and collisional friction force should be calculated in the framework of special theory of relativity. Such considerations show that the friction force has a minimum (electron-ion collisions are neglected as ineffective in exchanging energy):

$$F_{col} = \frac{4\pi e^4 n_e^* \ln\Lambda}{mc^2} \tag{2.28}$$

The acceleration of runaway electrons is impossible unless the electric field exceeds the critical one equal to the minimal frictional force divided by the elementary charge:

$$E > E_c = E_D \cdot \frac{T}{mc^2} = \frac{4\pi e^3 \ln\Lambda}{mc^2} n_e^* \approx 5.2 \cdot 10^{-22} \cdot n_e^* \ \mathrm{V/m} \tag{2.29}$$

Where $n_e^*$ is in $\mathrm{m}^{-3}$ and Coulomb logarithm was estimated in Born limit $\ln\Lambda \approx \ln(T_e \lambda_D/(\hbar c))$ ($\lambda_D$ Debye length) [55] to be 10 at $T_e \approx 10$ eV. Since an electron moving at $v \sim c$ has energy much higher than the bound energy in an atom we have to take into account collisions with all present electrons, i. e. bound and free $n_e^* = n_e + n_{bound}$. The question about critical field $E_c$ was raised by Connor and Hastie [56]. Complementary analysis of motion of the average electron was provided in [57, 58]. The condition 2.29 does not include any additional possible energy loss mechanisms like synchrotron and "Bremsstrahlung" radiation important for tokamak conditions. The role of the synchrotron radiation is to increase the critical field in several times as revealed in [58]. "Bremsstrahlung" on the other hand does not contribute to the value of critical field [59]. Nevertheless both mechanisms were

shown to play important role in limiting final kinetic energy of electrons.
Besides providing the expression for critical field the work [56] reports relativistic correction $S_{REL}$ (a multiplication factor) to the generation rate of runaway electrons. Even though both $T/mc^2$ and $E/E_D$ are small, they can be of the same order $E \cdot mc^2/(E_D \cdot T_e) \sim 1$, in fact when they equal the condition for critical field appears. The Fokker-Planck equation with collisional term expanded up to the second order in parameter $v'^2/c^2$ and neglected contribution of electro-ion collisions to the energy exchange was solved by Kruskal-Bernstein method to give:

$$S_{REL} = \exp\left(-\frac{T_e}{mc^2} \cdot \left(\frac{1}{8}\left(\frac{E_D}{E}\right)^2 + \frac{2}{3}\left(\frac{E_D}{E}\right)^{3/2} \cdot (1+Z)^{1/2}\right)\right) \tag{2.30}$$

The omission of the ion contribution to the energy exchange restricts the solution to hot plasmas $m_e/M_i \ll T_e/mc^2 \ll 1 \Leftrightarrow 0.5$ keV $\ll T_e \ll 500$ keV. Only qualitative conclusions concerning the relativistic effects can still be drawn for colder plasmas. The condition of the classical result (eq. 2.27) applicability is $(E/E_D)^2 \gg T/(8m_ec^2)$, which in the case of the current quench plasma $T_e \sim 10$ eV corresponds to $E > 10^{-3} \cdot E_D$. It may seem that, as current decays and consequently the induced field decreases, it should be obligatory to include factor 2.30. However if any runaways are to be expected, at the later stage with low fields $E \sim 10^{-3}E_D$ the primary mechanism is negligible and is dominated by the avalanche mechanism introduced in the next section. For this reason the relativistic factor is neglected in simulations of TEXTOR runaway discharges (chapter 5).

### 2.3.2 Avalanche mechanism

It was Sokolov [60] who first pointed out that the number of runaway electrons in modern tokamaks can exceed that predicted by the conventional theory due to close electron-electron collisions, in which a recoiling electron at once receives critical energy $\delta\varepsilon = mv_c^2/2$. If the lifetime of a runaway electron in the system is longer than time between two such close collisions an exponential multiplication takes place. The cross section of Coulomb collision with energy exchange $\delta\varepsilon$ is [61]:

$$\sigma = 2\pi r_e^2 \frac{\gamma^2}{\gamma^2 - 1} \frac{m_e c^2}{\delta\varepsilon} \tag{2.31}$$

where $r_e = e^2/m_ec^2 \approx 2.8 \cdot 10^{-13}$ cm is the classical radius of an electron. The frequency of the process is $\nu_{close} = n_e\sigma c$. Having estimated the life time of runaway electrons in tokamaks Sokolov found the number of secondary electrons created by one primary:

$$K = 3 \cdot 10^{-2} I_{pl}[\text{kA}] \tag{2.32}$$

As soon as $K$ exceeds 1 ($I_{pl} \geq 30$ kA) the exponential multiplication is possible, with exponentiation factor being $\gamma_{RA} = \nu_{close} = n_ec\sigma = eE/(2mc \ln\Lambda)$. Sokolov calculated $K \approx 12$ for T-10 tokamak and proposed this mechanism to be responsible for long lasting runaway tails in T-10 disruptions.
Essentially the same analysis was later performed in [62]. From comparison of the secondary multiplication rate $\gamma_{RE}n_{RE}$ with the rate of the energy gain from the field $ecE$ it was also pointed out that one secondary electron is knocked out for every $10 - 20$ MeV kinetic energy gained from the electrical field. That is why the mechanism took on significance only in the present day machines and will become even more effective in future (section 2.4.3). In most of the earlier experiments a runaway electron was lost before it reached such energies.
Rosenbluth and Putvinski [63] analyzed the Fokker-Planck equation with collisional integral consisting of two parts, with the first one being responsible for the small angle collisions and the other representing close collisions. For the small angle collisions the weak relativistic form was employed ($q = p/(mc)$, for further discussion of this form see section B.3):

$$St(f) = \frac{eE_c}{m_ec}\left(\frac{1}{q^2}\frac{\partial}{\partial q}\left((q^2+1)f\right) + \frac{(Z+1)\sqrt{q^2+1}}{2q^3}\frac{1}{\sin\theta}\frac{\partial}{\partial\theta}\left(\sin\theta\frac{\partial f}{\partial\theta}\right)\right) \tag{2.33}$$

The close collisions source of the secondary electrons was based on the Möller relativistic cross section in the limit of large energies. The analysis was performed in three limiting cases. In the first case, pitch angle scattering was neglected (formally $Z = -1$) and essentially Sokolov's result with $E$ replaced by $E - E_c$ was recovered. The other two cases with positive Z were distinguished as $E/E_c \gg 1$ and $E/E_c \sim 1$. On interpolating all three limiting cases by one formula Rosenbluth and Putvinski found the following growth rate:

$$\gamma_{RE} = \frac{e(E - E_c)}{m_e c \ln \Lambda} \sqrt{\frac{\pi\phi(a/R)}{3(Z+5)}} \cdot \left(1 - \frac{E_c}{E} + \frac{4\pi(Z+1)^2}{3\phi(a/R)(Z+5)(E^2/E_c^2 + 4/\phi(a/R)^2 - 1)}\right)^{-1/2} \tag{2.34}$$

Where $\phi$ is function of the inverse aspect ratio $a/R$:

$$\phi \approx \frac{1}{1 + 1.46\sqrt{a/R} + 1.72a/R} \tag{2.35}$$

Under assumption of $E \gg E_c$ equation 2.34 reduces to the approximate form:

$$\gamma_{RE} \approx \sqrt{\frac{4\pi\phi(a/R)}{3(Z+5)}} \frac{eE^{1/2}(E - E_c)^{1/2}}{2m_e c \ln \Lambda} \tag{2.36}$$

The square root factor represents the difference from Sokolov's result. It appears mainly because of the large initial pitch angle of the secondary electrons, which in toroidal geometry results in the particle trapping, as witnessed by the presence of the aspect ratio.For the typical TEXTOR current quench with $Z = 1 \div 2$ the numerical factor is in the range $0.62 \div 0.67$.

In the same work [63] the growth rate 2.34 was benchmarked versus solution of Langevin equation by Monte-Carlo procedure. It was found that for $E \gtrsim 2E_c$ the analytical expression underestimates the generation rate by less than 20%, with difference tending to 0 at larger fields. These results were later checked by the direct solution of the Fokker-Planck equation to have accuracy of about 10% [64]. It is also worth noting that if the avalanche mechanism is taken into account the energy spectrum of runaway electrons becomes exponential. The typical "temperature" of this spectrum is about $20 - 30$ MeV for $Z = 1 \div 4$ [63, 64].

Experimentally the secondary generation mechanism was unambiguously confirmed for the first time by Jaspers at TEXTOR [54].

## 2.4 Consequences of a disruption

### 2.4.1 Heat loads

The release of the full stored thermal energy on a short timescale during a disruption represents a serious problem to the plasma facing components. The highest loads are expected in the thermal quench phase because of the energy being deposited locally and on a very short time scale. To estimate the power flux $F$ it is necessary to specify three parameters: duration of the thermal quench $\tau_{TQ}$, broadening of the wetted area $b$, i.e. the ratio of the energy deposition width during disruption to that during normal operation $S_{norm}$, and the fraction of thermal energy $E_{th}$ preserved up to the TQ $f_{TQ}$:

$$F \sim \frac{f_{TQ}}{b} \cdot \frac{E_{th}}{\tau_{TQ} S_{norm}} \tag{2.37}$$

The inter-machine analysis of the duration of thermal quench results in the estimation for ITER $\tau_{TQ} = 0.3 \div 3$ ms [22] . As for the affected area, the earlier data suggested a conservative factor of $b = 3$ [22]. According to the latest observations the broadening of the power footprint can be up to a factor of 10 [29], with appreciable part of energy deposited outside of the limiting surface (divertor, limiter) [65]. The scatter in inter-machine scalings as well as between different types of disruptions is significant $b = 1 \div 10$. The fraction of the energy conserved up to TQ strongly depends on the type of disruption, for example in the density limit disruptions big portion of the energy is radiated [66] and only $20 - 40\%$ is lost in the final collapse. On the contrary hot VDEs and $\beta$–limit disruptions are characterized by $f_{TQ} \sim 100\%$.

The first assessment of ITER disruptions based on $\tau_{TQ} = 0.3 \div 3$ ms, $b = 3$, $f_{TQ} = 50 \div 100\%$ predicted enormous heat fluxes $10 \div 200$ GW·m$^{-2}$ [22]. Extrapolation from the recent JET data, where in the fast disruptions the flux of 1 GW·m$^{-2}$ was registered, with $b = 10$ remains threatening $0.3 - 100$ GW·m$^{-2}$ with average of 2 GW·m$^{-2}$ [29]. The latest inter-machine analysis indicates that the loads can be marginally tolerable if the toroidal asymmetries are not large and $f_{TQ} < 50\%$ [67]. The heat loads are to be mitigated if the thermal content of the discharge at the moment of the thermal quench is more than 50%, i.e. in case of hot VDEs or $\beta$–limit disruptions (including ITB case) [67].

To evaluate possible wall damage it is more convenient to characterize transitive heat loads in terms of the so called damage parameter $\phi_d = E/\sqrt{\tau}$ representing in fact the surface temperature after heat pulse of duration $\tau$. Indeed, consider the heat conduction problem for semi-infinite line with the heat influx $W$ at $x = 0$ different from zero in the time interval $0 \le t \le \tau$:

$$\frac{\partial T}{\partial t} = \kappa \frac{\partial^2 T}{\partial x^2}, \quad 0 \le t \le \tau, \quad x \ge 0 \tag{2.38}$$

$$T(x,0) = 0, \quad -K \frac{\partial T}{\partial x}\bigg|_{x=0} = W \tag{2.39}$$

The analytical solution of the problem is easily found to give the surface temperature at the end of the square pulse [68]:

$$T(0,\tau) = 2\sqrt{\frac{\kappa}{\pi}} \cdot \frac{W}{K} \cdot \sqrt{\tau} \sim \frac{E}{\sqrt{\tau}} \tag{2.40}$$

Extrapolation to ITER on basis of JET measurements gives $\phi_d = 24 \div 953$ with average $\sim 106$ MJ·m$^{-2}$·s$^{-1/2}$ [29]. Simple modeling considerations for hot VDE result in $\phi_d = 10 - 250$ MJ·m$^{-2}$·s$^{-1/2}$ [69]. The given parameters are seen to exceed the critical erosion parameter $\phi_{cr} \sim 15 \div 60$ MJ·m$^{-2}$·s$^{-1/2}$ for evaporation/melting for carbon, beryllium and tungsten to be used as wall materials. Solution of the two-dimensional heat conduction problem confirms that about 100 $\mu$m of the wall can be eroded in one major disruption or hot VDE [69]. It is to be mentioned that the physics of ablation process is much more complex due to the

formation of self shielding cloud of evaporated material, such calculations still indicate that layers about $30-70\ \mu$m can be lost in one event [70].
To sum up, the uncertainties in scalings toward ITER are high. It is nevertheless clear that the heat loads are marginally at or above the critical level and will determine the lifetime of plasma facing components. For this reason softening of heat loads is required.

## 2.4.2 Electromagnetic loads on the vessel

During current quench the vessel is subjected to large $\vec{j}\times\vec{B}$ forces. The current in the vessel has two main components: the mainly toroidal one induced by the decay of the plasma current and the mainly poloidal one transferred in direct contact of plasma with the wall. The last part is referred to as halo current. Even though both components have comparable magnitude the forces associated with the halo currents are stronger because of the interaction with the large toroidal field. Halo currents are usually a result of a VDE (independently on the hot/cold type of the instability) in elongated plasmas.

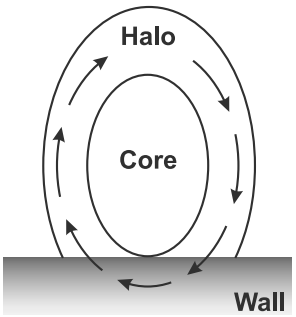


Figure 2.1: Schematic view of halo currents in poloidal projection.

**Halo currents**

As a result of a VDE the plasma turns from the diverted configuration into the limiter one. The scrape-off layer (terms SOL and halo zone are equivalent) is an area where the field lines are opened and intersect the wall. In spite of being colder than the core with closed magnetic surfaces this region is still able to sustain appreciable current. This current while flowing in the plasma is essentially force free owing to the low plasma pressure:

$$\vec{j}\times\vec{B}\approx 0 \Rightarrow \frac{j_p}{j_t}=\frac{B_p}{B_t}$$
$$\frac{I_p}{I_t}=\frac{2\pi R_0 w_h}{2\pi a w_h}\cdot\frac{j_p}{j_t}=\frac{R_0}{a}\cdot\frac{B_p}{B_t}=\frac{1}{q}, \qquad (2.41)$$

where subscripts "p" and "t" designate poloidal and toroidal components. In the wall the current follows the path of minimal impedance and can cause an appreciable force. This current is transferred from the core to halo region via three main paths: (i) direct transfer during vertical motion, the part of the core is scraped off to join the halo zone; (ii) induction by decaying core current; (iii) induction of poloidal voltage due to the change of the plasma area and consequently of the linked toroidal flux.
The existence of the poloidal current transferred from the halo region to the wall was confirmed by direct experimental measurements first in DIII-D [141] and later also in a number of other machines [22]. The current was measured either by arrays of Rogowski and toroidal field pick-up coils or by shunts installed in the current path. The direction of the current was found to coincide with the direction of the magnetic field lines as concluded from the experiments in which the direction of both $\vec{I}_{pl}$ and $\vec{B}_t$ was changed [36]. The current in the wall is predominantly poloidal [36] suggesting low rational number of poloidal turns in the plasma halo zone.
The maximal amplitude of the poloidal current measured in the wall in one machine scales like $I_{pl}(0)/q_{95}$ [36, 71, 72], while the inter-machine database shows clear scaling only with the plasma current but not with the edge safety factor [22]. It is to be noted that there is a strong scatter in the data even in one machine especially in comparing VDE events caused by different types of disruptions [71]. To understand this law we consider the late phase of VDE, i.e. when plasma motion is negligible and is balanced by the halo currents $\vec{j}\times\vec{B}$ force. The main driving force of halo current is the change of the core plasma current

$LdI_{pl,c}/dt$. Since the halo zone and the core are geometrically close to each other their mutual inductance almost coincides with the self-inductance. Hence the induced currents differ only because of the different resistances:

$$I_h \cdot \frac{q \cdot 2\pi R_0}{\sigma_h \cdot 2\pi a w_h} = I_{pl,c} \cdot \frac{2\pi R_0}{\sigma_{pl,c} \cdot \pi a^2} \Leftrightarrow I_h = \frac{\sigma_h}{\sigma_{pl,c}} \cdot \frac{2w_h}{a} \cdot \frac{I_{pl,c}}{q}, \tag{2.42}$$

where the core safety factor $q_c$ was taken to be unity. The equation gives the full "helical" amplitude of the halo current which in fact corresponds to the poloidal current in the vessel as mentioned above. The values of $q$ and $I_{pl}$ are those measured at the time of the plasma-wall contact, whose proportionality to the initial values is reasonable to assume. However the proportionality coefficient can be different for different types of disruptions, this being able to explain scatter in the experimental data. The additional source of the divergency is the ratio of halo to core conductivities $\sigma_h/\sigma_{pl,c}$. In reality, the scaling should be more complicated because of the halo width $w_h$ itself being determined by the force required to balance the vertical motion [31]. To reduce the halo current it is advantageous to dissipate as much as possible of the plasma current ($q$ grows at the same time!) before the width $w_h$ of the halo zone becomes significant and/or to diminish the halo conductivity $\sigma_h$ dramatically.
The toroidal distribution of halo currents is asymmetrical with dominant $n = 0$ and $n = 1$ components, with the last being probably caused by remains of the $n = 1$ instability participating in the TQ. The asymmetry can rotate toroidally with a frequency about several kHz like in ALCATOR C-MOD [36] or can be frozen similar to JET and COMPASS-D. The reasons for the rotation or its absence are not understood.
To characterize the magnitude of the asymmetry the toroidal peak factor is introduced TPF= $max(I_h(\phi))/f$, where $f$ is the average halo fraction $f = \langle I_h(\phi)\rangle /I_{pl}(0)$. The peaking value lies in the range $1 - 5$ and decreases with the growth of the average amplitude $f$. That is why the engineering specification is the product $f \cdot$ TPF, e.g. for ITER the value of $0.5 - 0.75$ is expected. In vertically stable discharges small halo currents are registered in the inner wall because of the inward plasma shift [36].
As for the modeling of the problem, with a suitable choice of the halo temperature the computations based on the Tokamak Simulation Code (TSC) are able to provide good agreement with experiment [44]. Many physical properties of the process can be understood in the framework of the simplified model derived in [73]. In this model the core and halo regions are represented by two coupled lumped circuits:

$$L_h \frac{dI_t}{dt} + R_h I_t = -M_{hp} \frac{dI_{pl,c}}{dt} - \frac{d\Phi_t}{dt} \tag{2.43a}$$

$$\frac{dI_{pl,c}}{dt} = -\gamma_I I_{pl,c} + (1 - f_r) \cdot j_{edge} \cdot \frac{d}{dt}\left(\pi a^2\right) - \frac{M_{ph}}{L_{pl}} \cdot \frac{dI_t}{dt} \tag{2.43b}$$

Transfer of currents takes place via inductance - terms with $M$, direct convection - term $(1 - f_r) \cdot j_{edge} \cdot \frac{d}{dt}\left(\pi a^2\right)$, and currents are also excited due to the change of linked toroidal current $\frac{d\Phi_{tor}}{dt}$. Good agreement with experiment is claimed to be achieved in simulations with experimentally measured halo resistivity and halo width [74, 75].

### Forces due to halo currents

The interaction of poloidal current flowing in the vessel with the strong toroidal field results in dangerous forces on the machine. Poloidal localization of the current leads to a net vertical force, while the toroidal asymmetry is responsible for a radial force. It is of course possible to determine the global force from the known amplitude of the halo current. But the easier way is to consider the force balance in the late VDE stage. The halo currents provide a force on the plasma column that balances the destabilization [31]:

$$F_{z,max} \approx 0.7 \cdot I_{pl}(0) \cdot \Delta Z_{max} \cdot \frac{dB_{r,eq}(Z_{max})}{dZ} \sim I_{pl}^2, \tag{2.44}$$

where the numerical factor 0.7 is an empirical value. The force equal in magnitude and opposite in direction is exerted on the vessel. An estimation for ITER gives 150 MN (15 kt) for the vertical force and 50 MN (5 kt) for the lateral loads [22].
The machine should be designed to withstand the expected forces. But since the loads can be localized and the current path in the vessel is unpredictable it is desirable to lower the induced stresses. The reduction of forces can be achieved by accelerating the current decay relative to the VDE growth rate. For example in ITER shortening of the current decay time from 2 s to 500 ms is predicted to decrease halo induced loads 3 times. This speculations are supported by the observation of reduced halo currents with increased current decay rate in JET [72].
However, for very short CQ times the eddy currents induced by the decaying plasma current have to be taken into account. In fact, in fast JET disruptions the EM loads are determined only by eddy currents [76]. The optimum range of CQ times for ITER predicted from the analysis of the detailed structure of the ITER wall is 50 – 500 ms [32, 69]. In particular the gaps in the ITER blanket give rise to local mechanical loads if the current quench time becomes less than 50 ms and large eddy currents are induced.

### 2.4.3 Runaway electrons

Runaway electrons were responsible for the localized wall melting already in the present day experiments. The exponential growth of the population is thought to lead to the overwhelming number of runaway electrons in the future experiment ITER. The number of exponentiations $\alpha_{tot} \sim \gamma_{RE} \cdot \tau_{CQ}$ during CQ phase of duration $\tau_{CQ}$ can be estimated from Maxwell equations and Sokolov's formula for the secondary multiplication (section 2.3.2):

$$B = \frac{2I}{ca} \Rightarrow \frac{dB}{dt} \sim \frac{2I}{ca\tau_{CQ}}, \; E = \frac{R_0}{2c} \cdot \frac{dB}{dt} \sim \frac{I}{c^2\tau_{CQ}} \frac{R_0}{a} \tag{2.45}$$

$$\alpha_{tot} \sim \gamma_{RE} \cdot \tau_{CQ} \sim \frac{eI}{2m_e c^3 \ln\Lambda} \cdot \frac{R_0}{a} \sim \frac{I}{I_A \ln\Lambda}, \tag{2.46}$$

where the Alfvén current $I_A = m_e c^3/e \approx 0.02$ MA was introduced. The equation predicts multiplication of the order of $e^{50}$ for a 20 MA discharge in ITER to be compared with the factor about 5 for 350 kA TEXTOR and $e^5 \approx 150$ for 2 MA JET discharges. More elaborated modeling gave 10 MA current carried by runaways with the associated energies of 50 MJ and 1000 MJ in the kinetic and magnetic parts correspondingly [32]. If such runaway beam is lost to the wall new runaways are likely to be created by the induced voltage, which would in the worst case deposit of 80% of the stored runaway energy onto undefined but most probably very limited surface. To conclude, the generation of runaway electrons must be prevented in any disruption.

## 2.5 Disruption mitigation

It has been shown above that the softening of disruptions will be required in ITER. A successful mitigation technique has (i) to redistribute the heat fluxes over a large wall surface in the thermal quench, (ii) to accelerate the current decay relative to the growth time of vertical instability and/or to predominantly cool the halo region, (iii) and to prevent electrons from running away. All of that can be achieved by the injection of large amounts of impurities. The heat fluxes are ameliorated either by creating a radiative mantel around the plasma column which intercepts the heat flow or by depositing impurities directly into the central part of the discharge. At the beginning of the current quench it is expected that an appreciable number of impurities has penetrated to the core plasma. These impurities have to accelerate the current decay and/or to predominantly cool the halo region, which is necessary for suppression of halo currents, and to unconditionally prevent the generation of runaway electrons. The latter can be achieved if the induced electric field is below the critical one $E_{ind} < E_C \sim 5.2 \cdot 10^{-22} \cdot (n_e^*[\mathrm{m}^{-3}])$ V/m, i.e. the density of electrons (including the bound ones!) is high enough.
Of course, to perform mitigation the forthcoming disruption is to be detected well before it actually happens. Therefore the problem of early disruption detection on basis of the global plasma parameters has become a topic of major interest. Up to now the artificial neural networks made it is possible to predict disruptions in a single tokamak $20 - 40$ ms before the thermal quench with the probability better than 90% and the false alarm chance of only few percents [77, 78, 79], the high-$\beta$ disruptions being the most difficult to predict owing to the short precursor phase [80, 81]. Recently the first attempts to compose inter-machine networks appeared [82], the performance of such schemes has not yet reached the desired level. A more detailed discussion of this topic is beyond the scope of the thesis.
At the present time disruption mitigation experiments are concentrated on the study of physical basics and efficiency of a particular method. Therefore in almost all works the terminated discharges are stable. The ways of delivering particles include pellet injections and massive gas injections.

### 2.5.1 Review of pellet injection experiments

Pellets of frozen deuterium are used for the deep plasma fueling. When accelerated to velocities of the order of $1000$ m·s$^{-1}$ such pellets penetrate up to the center of a discharge due to the formation of self shielding cloud of ablated material [83, 84]. Impurity pellets deposit material deeply into the plasma in the same way and that is why they can relatively easily cause a radiative collapse without disruptive phase. The experiments where impurity pellets were intentionally injected to study radiative collapse disruptions are considered in the machine oriented way. The main parameters of discharges used in different disruption mitigation (DM) experiments are listed in table 2.1.

#### T-10

Injections of small size KCl and Ti pellets were reported [85]. Strictly speaking, these experiments can not be classified as disruption mitigation, since the amount of injected impurities $< 5 \cdot 10^{18}$ limited by the size of the pellet guiding tube was not enough to terminate the discharge. When injections were performed in the flat top phase the plasma recovered its initial parameters after an interval of the order of $50$ ms after the last minor disruption. Introduction of impurity pellets in the current ramp down phase accelerated the current decay rate significantly, which is favorable for the suppression of halo currents.
The 1D model developed to describe the experimental data could reproduce the behaviour of the central temperature only if increased transport similar to DIII-D experiments described below was allowed (pellets penetrated only to the half of the minor radius).

| Tokamak | $a_p/R_0$, m/m | $B_t$, T | $I_{pl}$, MA | $n_e$, $10^{19}$ m$^{-3}$ | L/D | $P_{aux}$, MW | $E_{th}/E_{mag}$, MJ/MJ | Type | N, $10^{21}$ atoms |
|---|---|---|---|---|---|---|---|---|---|
| **T-10 [85]** | 0.39/1.5 | 2.5 | 0.08 – 0.2 | 2.5 – 4.5 | L | 0 | ?/? | **P** - KCl, Ti | 0.005 |
| **TEXTOR present** | 0.46/1.75 | 2.25 | 0.35 | 2 | L | 0 | 0.05/0.3 | **MGP** - $D_2$, He, Ar, Ar% | 0.8 – 20 |
| **TORE SUPRA [91]** | 0.72/2.40 | < 4.2 | < 1.2 | 4 | L | 0 | ?/? | **MGP** - He | 200 |
| **ASDEX-U [86]** | 0.5/1.6 | < 3.9 | 0.6; 1 | ? | D | 0; 9 | (0.06; 0.5)/(0.6; 1.5) | **P** - Ne | 0.17 |
| **ASDEX-U [92]** | 0.5/1.6 | < 3.9 | 0.4 – 0.8; ? | ? | L/D | ? | (0.05 – 0.2)/? | **MGP** - He, Ne, Ar | 0.7 – 3 |
| **DIIID [87, 88]** | 0.6/1.7 | 1.8 – 2.1 | 1 – 1.5 | ? | D | ? | ~ 1/ ~ 2 | **P** - Ne, Ar, Ne% | 0.28 – 0.68 |
| **DIIID [95, 96, 97, 98]** | 0.6/1.7 | 2.1 | 1.5 | 3; 8 | D | 5 – 7 | (0.6 – 0.9)/1.6 | **MGP** - $D_2$, He, Ne, Ar | 40 |
| **ALCATOR C-Mod [99]** | 0.21/0.66 | 5.4 | 1 | 15 – 30 | D | ? | 0.1/0.65 | **MGP** - He, Ne, Ar, Kr | 50 – 100 |
| **JT-60U [89]** | 1/3.4 | 2.2; 3.3 | 1.6 – 1.7 | ? | D | 0; 12 | (0.25; 1.8)/3.7 | **P** - Ne | 0.5 – 2.1* |
| **JT-60U [101, 102]** | 1/3.4 | 3.5 | 0.85 | 1 – 1.5 | D | ? | ~ 0.3/ ~ 0.93 | **SGP** - $H_2$, Ar, Kr, Xe,% | 0.2 – 10 |
| **JET [103]** | 1.25/2.96 | 3 | 2 | ? | D | ? | ?/? | **SGP** - He, Ne, Ar | < 9 |

Table 2.1: Parameters of discharges used for disruption mitigation experiments in different tokamaks. "L" - limiter, "D" - divertor,"$P_{aux}$" - auxiliary heating, mainly NBI. "$E_{th}$" - thermal energy content, "$E_{mag}$ - magnetic energy", "**P**" - pellet injection, "**MGP**" - massive gas puff by ferromagnetic or eddy currents valve, stated amount of particles is introduced in 1 – 10 ms, "**SGP**" - slow gas puff by standard fueling valves, the stated amount of atoms is introduced in 50 – 100 ms, "$N$" - number of injected atoms. "?" stands for unknown value. In TEXTOR case "Ar%" denotes the argon mixture experiments, while in JT-60U row "%" marks experiments with mixtures of hydrogen with one of Ar, Kr, Xe. It worth noting that the shown limit of injected particles in the gas puff experiments is imposed by requirements of the tokamak vacuum system, while for "killer" pellets it is limited by the achievable size of the pellet itself. *– achieved by train of three pellets.

**ASDEX**

Neon pellets containing about $1.7 \cdot 10^{20}$ atoms were used to terminate discharges with and without additional NBI heating [86]. Heat fluxes to the divertor were found to be strongly reduced in comparison with unmitigated cases. In ohmic discharge the ratio of the energy deposited onto the divertor plates to the discharge thermal content was close to 0. In NBI (9 MW) heated shots this ratio reached 12% to be compared with nearly 100% found in the density limit disruptions. In addition low mode number MHD activity and the positive current spike typical for any other disruption were not detected in Ohmic discharges terminated by pellets. In experiments with additional NBI heating both phenomena were present. Stresses on the machine due to halo currents were suppressed on average by 50%. Generation of runaway electrons was not reported.

**DIII-D**

Injections of 1 – 4 mm large Ar and Ne pellets removed large part of the plasma thermal energy during pellet ablation [87]. The heat flux to the divertor was reduced by 40% by radiative redistribution. However, the fact that the bulk of the energy was radiated at relatively shallow pellet penetration $\sim 0.4 \cdot a_p$ required an assumption of dramatically increased inward transport. The observed decrease of the vessel forces due to halo currents amounted up to 50%. In addition to lowering the average value of the halo currents $f$ the toroidal peak factor was also lower by a factor more than 1.5 in comparison with natural disruptions [88]. The amount of introduced impurities corresponding to a few percents of the discharge electron content was insufficient to hinder the formation of runaway electrons carrying up to 30% of the predisruptive plasma current [87]. The formation of RE beam was found to follow any argon pellet injection and many of that of neon pellets.

**JT-60U**

Ne pellets one per shot or as a train of 3 pellets drastically reduced the heat flux to the divertor [89]. After TQ the vertical position of the plasma channel could be reliably controlled close to the neutral point so that the halo currents were almost completely suppressed. Strong runaway electrons generation was registered by several diagnostics including X-ray detectors in two complimentary energy ranges (0.1 – 1 MeV/> 1 MeV) and neutron detector sensitive to RE with energies exceeding 30 MeV. The generation was proved to be sensitive to the toroidal magnetic field $B_t$ and to the level of radial field $B_r$ fluctuations.

**Summary**

It is a general observation that the heat flux to the limiting surface (limiter/divertor) can be significantly reduced due to enhanced radiation of injected impurities. Impurities turn out to be rapidly mixed toward the plasma center even without reaching it. Similarly halo currents and related forces are reduced significantly. The only disadvantage of this method is the generation of runaway electrons because of relatively small amount of introduced electrons. To unconditionally suppress runaway electrons in ITER deuterium pellet should have a size of about 10 cm [22] and even larger pellets of higher-$Z$ materials are to be considered. All of that along with an unclear scaling of the rapid inward transport make the success of this method in ITER questionable and call for the development of other techniques.

### 2.5.2 Review of massive gas injection experiments

In massive gas injection experiments impurities are delivered as a dense gas jet. It is not clear whether atoms can penetrate to the center of a discharge before the disruption. In fact, in the experimental part of this thesis it is shown that the injected particles are localized at the plasma edge before the onset of disruption. Nevertheless, such situation

does not preclude the reduction of heat loads, as discussed below. Since the total number of introduced atoms is by orders of magnitude higher than in the case of "killer" pellet termination, it is hoped that the inward mixing during the thermal quench is able to deliver to the plasma core so many atoms as to stop the generation of runaway electrons. The experiments are again listed in the machine oriented form.
In the following descriptions two experimental techniques are to be distinguished. In the first of them gas is introduced through the standard fueling valves in 50 – 100 ms (slow gas puff). In the other specially designed ferromagnetic or eddy currents valves are able to inject particles in 1 – 10 ms, with the particle flux being by more than two orders of magnitude higher. In spite of being not suitable for actual disruption mitigation slow gas puff nevertheless helps to understand the physical basics.

**TEXTOR**

A valve activated by eddy currents[2] was developed in Jülich. The absence of any ferromagnetic materials in the construction allowed the valve to be operated in high static magnetic fields present in the tokamak environment. In the first experiments at TEXTOR about 10 mbar·l[3] of helium were injected by the fast valve into low-density runaway discharges [90]. Helium led to termination of the existing runaway beam and prevented electrons from running away in the current quench phase. The conditioning of the following discharge was not found to be affected by the intense puff. A more detailed investigation of the suppression of runaway electrons in the current quench phase and study of the typical timescales were not conducted.

**TORE SUPRA**

Acceleration of runaway electrons is the usual consequence of natural disruptions in TORE SUPRA. Injections of 1 – 10 bar·l of helium performed by a fast valve driven by an electromagnet were able to suppress runaway electrons in the caused disruption [91]. On basis of this it was argued that the neutral gas penetrated to the very center of the discharge. The effect on the discharge following the one terminated by the massive helium injection was negligible.

**ASDEX Upgrade**

Different gases (He, Ar, Ne, 30 – 120 mbar·l) were injected by the fast disruption mitigation valve developed in Jülich [92]. In the circular limiter configuration the gas was found to considerably (order of magnitude) accelerate the current decay rate. In the elongated divertor phase the effect was less pronounced (maybe a factor of 1.5) and was not studied in detail. Anyway the massive injections led to up to 3 times reduction in halo currents and up to 4 times in mechanical stresses. Runaway electrons were not studied systematically.

**DIII-D**

In the first experiments argon puff by standard fueling valves was used to provide reliable triggering for study of temperature and electron density dynamics in what was called "radiative" collapse [93]. $T_e$ and $n_e$ profiles measured by Thomson scattering showed complex behaviour with the initial pronounced cooling and at the same time electron density peaking at the edge. The current profile determined by the motional Stark effect as well as by the equilibrium reconstruction of magnetic probes signals experienced flattening in the positive current spike on a timescale much faster than the neoclassical resistivity would

[2] One has to distinguish the eddy currents mentioned here from the eddy currents excited during the plasma current decay in the vessel components. The eddy currents opening the valve are excited by discharging a capacitance bank through a coil mounted close to the valve piston. For a more detailed description of the valve construction see section 3.1.

[3] "bar·l" is a convenient unit for measurements of the number of particles. 1 bar·l $\approx 2.4 \cdot 10^{22}$ particles.

assume.
DM studies were mainly conducted with the fast ferromagnetic valve [87]. As in the "killer" pellet experiments such injections of helium reduced forces on the vessel due to the halo currents as much as by 50%. The fraction of radiated energy during experiments increased by almost 50% compared with the natural events. No traces of runaway electrons were found. Presence of helium made it possible to measure the electron temperature and effective charge during CQ by XUV spectroscopy under reasonably confirmed assumptions of the uniform density distribution [94]. The sense of the method was to compare intensities of HeI and HeII lines and of the recombination continuum emission. The found values were $T_e \approx 5$ eV, $Z_{eff} \approx 1.8$ for the core region and $T_e \approx 4$ and $Z_{eff} \approx 1$ for the halo zone.
Later the fast valve was used for injections of up to 2 bar·l of different gases: deuterium, helium, neon and argon [95, 96]. On basis of the cold front propagation it was argued that the neutral gas penetrated to the very center of the discharge. Neon and argon were found to lower heat loads on the divertor plates by an order of magnitude, which was confirmed by the divertor thermography and bolometry. The absence of any features typical to runaway electrons was attributed to lowering of the induced electric field below the critical one $E_C$.
However already in the next work the more complex nature of the massive gas puff shutdown was revealed [97]. Discharge termination was found to proceed in two main step: at first the cold front changed considerably regions up to about $q = 2$ and then the thermal quench took place with pronounced MHD activity having dominant $n = 1$ and $m = 1,2$ modes. The start of MHD seemed to correlate with the cold front penetration seen on Thomson scattering profiles to the $q = 2$ flux surface [98]. To confirm the last point a variation of the $q$-profile was performed and demonstrated strong influence on the duration of the predisruptive phase. The time for the gas to destabilize the plasma changed from 1 to 3 ms as the position of the $q = 2$ flux surface was shifted from $\Delta r = 5$ to $\Delta r = 15$ cm relative to the plasma edge. Consistent data were obtained by an array of XUV detectors: XUV emission was localized to the plasma edge before TQ and progressed towards $q = 2$ in the collapse phase [97]. The shallow penetration of neutral jet was concluded from one image of the neutral impurity visible radiation per shot taken by a gated CCD camera. In spite of not penetrating to the plasma center, impurities were found to radiate bulk of the thermal energy and to reduce the heat fluxes to the divertor; the toroidal symmetry was not discussed. Small traces of runaway electrons were present in discharges terminated by massive injections of argon or neon, but their magnitude was two orders smaller than in the "killer" pellet experiments as judged from soft X-ray emission during current quench.

**ALCATOR-C**

Injections of helium, neon, argon and krypton in amounts up to 5 bar·l were performed by the same system as at DIII-D [99]. Similar to DIII-D it was observed that the heavy gases did not penetrate deeply into the plasma before TQ. Helium in contrast was deposited much deeper and increased electron density at radii up to $0.5a_p$ at $t = t_{TQ} - 0.8$ ms and in the plasma center just prior to the disruption. These facts were derived from one visible camera frame per shot and from Thomson scattering measurements of $T_e$ and $n_e$. The halo currents were reduced by 50%. As for the heat loads, in mitigated disruptions up to 70% of the initial energy content including thermal and magnetic parts were radiated, with larger radiated fraction being typical for higher-$Z$ impurities.
To accompany experimental investigations the simulations of the MHD activity in argon injection experiments were carried out by using 3D resistive MHD code NIMROD [100]. In these simulations impurities with concentration $f_Z = n_Z/n_e = 0.75$ were placed at a fixed distances from the $q = 2$ flux surface. The inward propagation and mixing of impurities were not considered. The position of the radiating boundary relative to the $q = 2$ flux surface proved to be the critical parameter determining the time of the fast growth of modes with low numbers $m/n$, i.e. the delay before thermal quench. The delay time depended in strongly non-linear manner on the relative position of the impurities. The TQ itself

developed in two stages: at first the $n = 1$, $m = 2$ island grew destroying the outer flux surfaces and giving rise to the stochastization there, afterwards in the inner domain the energy was evenly redistributed by the $n = 1$, $m = 1$ mode. In the post TQ phase intact flux surfaces were restored in the plasma center, which provides favorable conditions for RE acceleration. It is to be noted that to facilitate computations in the simulations Lundquist number inverse proportional to the resistivity was artificially decreased by two orders of magnitude, so that the model does not directly reproduce the experimental time scales.

**JT-60U**

At JT-60 [101] massive gas puffs were performed with the aid of the standard fueling valves providing flow rates about 0.2 bar·l·s$^{-1}$ for pure argon and about 1.2 bar·l·s$^{-1}$ for hydrogen. The experiments showed strong runaway electron generation in the case of the discharge termination by pure argon injections, while pure hydrogen precluded formation of the runaway tail. The further step was to combine injection of hydrogen and argon through two different valves to produce a "mixture" containing about 1% of argon. Such mixtures were found to terminate the discharge on the time scale 2 times faster than with pure argon or hydrogen and without accelerating runaway electrons. The derived critical parameters for the generation of runaways were the ratio of loop voltage to electron density $V_L/n_e$ and the level of magnetic fluctuations, with high magnetic fluctuations being advantageous in suppressing RE.
Later similar experimental technique was used for comparative study of argon, krypton and xenon as pure gases or in "mixture" with hydrogen [102]. The injection of Kr + $H_2$ resulted in the lowest heat flux to the divertor and the lowest amount of generated runaway electrons. Termination of the discharge took place before the cold front observed by ECE measurements reached the plasma centre. The velocity of the cold front before the thermal quench was found to be inverse proportional to the square root of the atomic mass of the used gas $\sqrt{m}$. But the absolute magnitude of that velocity was much slower than the sound speed ~ $\sqrt{T/m}$ of the neutral gas at room temperature.

**JET**

Slow standard fueling valves supplied up to $9 \cdot 10^{21}$ atoms of He,Ne or Ar in 50 ms [103]. Helium injections prevented the formation of runaway electrons in the specially designed discharges otherwise leading to their acceleration. On the other hand helium slowed down the current decay rate and, as a consequence, increased electromagnetic loads on the vessel. Neon and argon accelerated current quenching and resulted in the reduced vessel electromagnetic loads, but were prone to runaway tails.

**Summary**

Massive gas injection successfully reduces the halo currents and heat fluxes to the limiter/divertor like "killer" pellets. Scaling of the mitigation effect is hardly possible as the dynamics of the injected atoms and the succession of events leading to the final collapse are poorly understood. Only recently it was realized that the neutral gas penetration is very shallow and the central role is played by the critical $q = 2$ flux surface and destabilization of low number MHD modes. The shutdown scenario turned out to be disruptive. However such conclusions arose from very scant experimental data, which should be certainly extended.
For injections of heavy gases a strong population of runaway electrons is usually registered. A systematic investigation of the physical reasons for RE appearance was not conducted.
In this thesis the following questions related to the disruption mitigation by massive gas injection are raised: (i) investigation of the main characteristics of the fast valve developed for MGI in Jülich. (ii) clarification of the phenomenology of MGI experiments, in particular the dynamics of the injected particles is observed by means of the unique fast

framing camera; (iii) a systematic analysis of the generation of runaway electrons in the experiments on disruption mitigation by MGI.

# Chapter 3

# Experimental setup

In the previous chapter it was shown that to mitigate a disruption large amounts of impurities are to be introduced in a short time. In this chapter the design of suitable system is discussed. Calibration data for the fast valve are presented. In addition a short description of the ultra-fast camera system and other essential diagnostics used in the experiments is given.

## 3.1 Fast disruption mitigation valve

The systems used for the gas injection are either solenoid-actuated valves or valves activated by eddy currents. It is to be mentioned that there are also attempts to use piezoelectric valves. However the gas flow rate of $\sim 1$ bar·l·s$^{-1}$ achieved with such systems [105, 106] is much lower than required for large scale experiments. The high performance solenoid valves extensively used at DIII-D [95, 97], Alcator-C [107] and Tore-Supra [91] are similar to that described in [108], in which the ferromagnetic piston is drawn by the gradient of the magnetic field. In the recently emerged two stage valve [109] the solenoid valve is the pilot one, the second stage being opened by the pressure imbalance created by the outflow from the first stage. Though providing in both mentioned cases the valve opening time shorter than millisecond the ferromagnetic piston does not allow the valve to be installed in the immediate vicinity of a tokamak. A several meter long tube connecting the injection system and the vessel has to be introduced. This fact considerably increases the total system reaction time consisting of the valve opening time and the time for the gas to travel through the delivery tubes. As opposed to it, the disruption mitigation valve (DMV) activated by eddy currents [104] does not exploit any ferromagnetic materials and can be reliably operated in a high static magnetic field as it has been already demonstrated experimentally [90, 92]. This type of DMV is currently used at the tokamak TEXTOR and has been recently installed at the largest fusion experiment JET. In this section the detailed calibration data of the DMV are presented.
The calibration is based on the direct observation of the piston motion by means of the fast framing camera. The results of these observations are used to determine the valve reaction time, the gas outflow rates and to explain the dependence of valve performance on the operational parameters.

### 3.1.1 DMV principles

To begin with, briefly consider an ideal DMV working cycle. In the charged state (fig.3.1-1) the aluminium mushroom-shaped piston, with the diameter of stem 20 mm and the diameter of back part 200 mm, effectively closes the 10 mm orifice of the working chamber owing to the pressure imbalance on the orifice surface. The registered leak rate does not exceed $10^{-5}$ bar·l·s$^{-1}$ [110] as required by a tokamak vacuum system. In the valve used for calibrations the volume of the working chamber is 320 ml, which differs from that used at TEXTOR and JET: 30 and 650 ml. The scaling of the obtained results with volume is straightforward. The pressures in working ($p_w$) and back ($p_b$) chambers are in the range 5 – 60 bars and related by the closing condition $p_w < 1.8 \cdot p_b$ given by the ratio of the actual areas $A_1$,$A_2$ on which the pressures are acting, as it is illustrated in figure 3.1-2. The closing force provided by the pressure imbalance at $p_b = 5$ bar approximately amounts to ($S_o \approx 3/4$ cm$^2$, the force on "$A_2$" is not taken into account):

$$F_p = S_o \cdot p_b \approx 40\ N \tag{3.1}$$

For the modified valve with two times larger diameter of the orifice as discussed at the end of this section the force is correspondingly four times higher.
When the capacitance bank ($C \approx 200$ mF, $U \approx 2$ kV) is discharged through the coil a time-varying magnetic field excites eddy currents in the back part of the piston. The resulting $\vec{j} \times \vec{B}$ force opens the valve by repelling the piston (fig.3.1-2). To estimate opening force we examine a simplified 1D problem. The magnetic field having only $x$ component is varied close to the half-space field by a conductor, fig. 3.2-1. The evolution of magnetic field is described by the well known heat conduction equation [111]:

$$\frac{c^2}{4\pi\sigma}\Delta B = \frac{\partial B}{\partial t} \tag{3.2}$$

The field penetrates to the characteristic skin depth $\lambda \sim \sqrt{\tau c^2/(4\pi\sigma)}$. The typical timescale of the field variation in the experiment is about 0.3 ms as illustrated by the oscillogram of

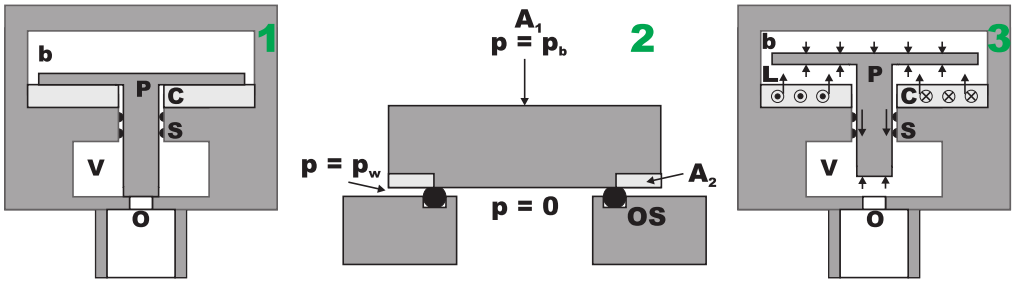


Figure 3.1: The schematic view of the valve. 1 - the valve is charged; 2 - the detailed view of the output orifice; 3 - the valve is being opened, main forces are illustrated. The notation: "V" - the chamber containing the gas to be injected (working chamber); "b" - the chamber filled with the gas providing the closing force (back chamber); "L" - part of the back chamber separated by the piston; "P" - the aluminium piston; "C" - the pancake coil; "S" - the sealing separating working and back chambers; "O" - the orifice; "OS" - the O-ring sealing the output orifice; "$A_1$", "$A_2$" - the areas on which $p_b$ and $p_w$ are acting.

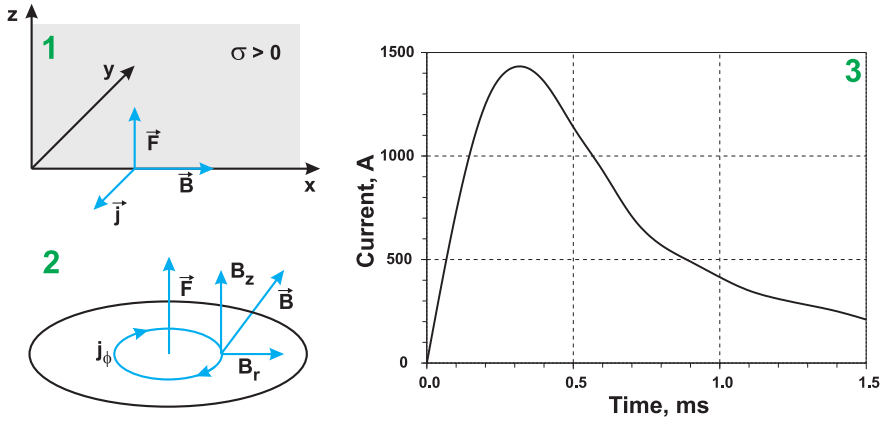


Figure 3.2: Repelling force. 1 - the one-dimensional problem. The direction of current $\vec{j}$ is easy to obtain from $rot\vec{B} = 4\pi\vec{j}/c$. Since $\vec{B} = (B,0,0)$ decreases with $z$ the current is antiparallel to $y$–axis. 2 - the problem with cylindrical symmetry. The field $\vec{B}$ created by the coil (not shown here) is decomposed into the axial component $B_z$ and the radial component $B_r$. 3 - the typical oscillogram of the current flowing through the coil. This plot is reproduced from [92].

the current flowing through the coil (fig. 3.2-3). The resulting depth $\lambda \sim 0.23$ cm[1] is much smaller than the thickness of the back part of the piston $h = 0.5$ cm. In the case $\lambda \ll h$ the order of magnitude of the opening force can be obtained in the following way:

$$rot\vec{B} = \frac{4\pi}{c}\vec{j} \Rightarrow j \sim \frac{c}{4\pi\lambda}B$$
$$F_{EM} = \frac{1}{c}VjB \sim S_b\frac{B^2}{4\pi} \qquad (3.3)$$

Where the force is assumed to act in the volume $V = S_b\lambda$, with $S_b$ being the surface area of the piston back part. A characteristic value of magnetic field is that at the axis of the coil $B = \mu_0 NI/(2a) = 0.3$ T [33], where $N \sim 50$ is number of windings, $a \sim 0.1$ m is typical radius of the coil and $I \sim 1$ kA. The electromagnetic force $F_{EM} \sim 2$ kN is seen to be much larger than the closing pressure force $F_{EM} \gg F_p$. Hence the piston can be

[1] Resistivity of aluminium $1/\sigma$ is $3 \cdot 10^{-18}$ s in CGS units or $2.7 \cdot 10^{-8}$ Ohm·m in SI units.

thought to be accelerated by the $\delta$-like force $F_{EM}$ and later decelerated and returned to the original position by the pressure imbalance. In cylindrical geometry the situation is more complicated: the axial component of the magnetic field $B_z$ excites an eddy current $j_\phi$, the repelling force is produced by the interaction of this current with the radial magnetic field $B_r \sim B_z$ (fig 3.2-2).
In the laboratory a thin plate similar to the piston but having no stem was fired upward by the coil. The maximum achieved altitude of the disc was interpreted as the energy transferred by the repelling force. Such measurements indicate that about 5% of the electrostatic energy of 1 kJ stored in the capacitance bank can be transformed into kinetic energy of the piston. Assuming the energy $W$ is transferred on the distance $L \approx 1$ cm one assesses the force:

$$F_{EM} = \frac{W}{L} \sim 5 \text{ kN} \tag{3.4}$$

The estimation (eq. 3.3) and the measurements are in reasonable agreement within an order of magnitude.
The next question to be addressed is the ability of the valve to stay closed in strong external magnetic fields typical for the tokamak environment. The typical tokamak fields vary so slowly as to fall into the limit $\lambda \gg h$ ($\tau \geq 10$ ms). In such case the estimation given by equation 3.3 is not applicable since $rot\vec{B}$ becomes zero in the first order [111]. An alternative way has to be followed:

$$rot\vec{E} = -\frac{1}{c}\frac{\partial \vec{B}}{\partial t} \Rightarrow E \sim \frac{h}{c}\frac{B}{\tau} \Rightarrow j = \sigma E \sim \frac{\sigma h}{c\tau}B \tag{3.5}$$

$$F_{ext} = \frac{1}{c}VjB \sim S_b\frac{\sigma h^2}{c^2\tau}B^2 = S_b\frac{B^2}{4\pi}\cdot\frac{h^2}{\lambda^2}, \tag{3.6}$$

where the typical gradient length equals the height of the disk and the integration volume is accordingly $V = S_b h$. The requirement of $F_{ext} < F_p$ is fulfilled for toroidal field of 2 T if the typical time scales are larger than $2-3$ s. The same condition for the field produced by plasma current ($B \sim 0.2$ T) is satisfied for $\tau > 30$ ms. Even though no screening was taken into account and the amplitudes of magnetic fields at the location of the valve are certainly overestimated, the conditions are always fulfilled for TEXTOR discharges. It is also worth stressing here that the estimations performed in both manners (eq. 3.3 and eq. 3.6) coincide in the limit $\lambda \ll h$.

### 3.1.2 Test arrangement

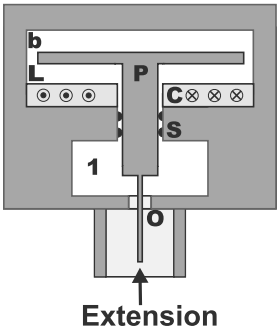


Figure 3.3: Modified piston. Notations coincide with those of figure 3.1.

In reality the piston dynamics is affected by all applied forces illustrated in fig. 3.1-3: EM force exerted by the coil current, pressures $p_1 \equiv p_w$, $p_b$, $p_L$ (pressure in the section appearing below back part of the piston) and the friction force in the sealing separating the chambers (the pressure equivalent of the friction force $p_{fr} \equiv F_{fr}/A_1$ is 5 bar), where the pressures are themselves dependent on the piston motion. It is this dynamics that determines the width and the duration of the valve opening and hence the gas injection rate and the total amount of the puffed gas. To measure the opening characteristics of the valve experimentally a 3 mm thin pin was mounted at the leading end of the piston as it is sketched in fig. 3.3. The displacement of the pin was observed with the aid of the fast framing camera PSI5 (section 3.2) through a vacuum window. The optical setup provided a spatial resolution of about 0.3 mm. This approach allows the opening characteristics to be measured with a pressure evolution very similar to the original one when the piston extension is not mounted. Furthermore the

average gas outflow rate is easy to estimate from the obtained injection durations without implementing any particular scheme of the unsteady transonic flow measurements. The disturbances introduced by the presence of the pin are thought to be insignificant: the piston mass modification is about 1.7%, the orifice area change is about 9%.
Injections were performed into a 20 l volume evacuated to $\sim 10^{-2}$ Torr by a roughing pump. In addition to the registration of the piston position the pressures in the working and back sections were measured before and after every experiment by means of pressure transducers. During the tests, only helium and argon were addressed as being of particular interest for the disruption mitigation experiments. The gases in the back and working sections could be the same or different, i.e. the following configurations of gases were used: "Ar/Ar", "He/He", "Ar/He", "He/Ar", where the first symbol stands for the working gas and the last one is the gas in the back section. The back pressure $p_b$ was varied in the range 5 – 35 bar, the working one was either equal to it $p_w = p_b$ ("equal") or higher by the fixed factor $p_w = 1.5 \cdot p_b$ ("overpressure").

### 3.1.3 Opening characteristics

An example of the recorded frame sequence of the pin movement is shown in figure 3.4, the pin is the black square in the center as seen in backillumination. Upon receiving the trigger signal at time moment 0 the piston together with the pin are drawn to the left: the valve is opened. As the pressure in the working chamber decays the resulting decelerating force makes the piston stop and move back. The original set consists of 300 frames obtained with 50 $\mu$s time resolution. The piston position relative to the closed state as a function of time is given in figure 3.5. The noticeable opening of 0.5 mm to be associated with the reaction time of the system is achieved about 0.3 ms after the trigger in all cases. The full opening occurs after approximately $1 \div 2$ ms. The detailed dynamics depends on the gas species and the overpressure factor as it is discussed below.

The graph in fig. 3.5-1 compiles the time-position correspondences for a number of different pressures in "He/He" experiments. The curves are labeled by the corresponding working and back pressures "$p_w/p_b$". It can be concluded from the plot (curves "5/5", "15/15", "35/35") that an increase of the back pressure decreases both the width and the duration of the opening . While the overpressure (curves "8/5", "23/15", "53/35") provides a wider gap and prolongs the injection time by keeping the back pressure balanced for a longer period. The described results are in full correspondence with the change of the term $p_b - p_w(t)$ in the equation of the piston motion:

$$m_p \cdot \frac{dV}{dt} = (p_b - p_w(t) - p_{fr} \cdot \mathrm{sign}(V)) \cdot \mathrm{A}_1, \tag{3.7}$$

where $\mathrm{A}_1$ is the surface area of the stem and $m_p$ is mass of the piston. The backward motion starts at the time moment when the back pressure exceeds the sum of the working

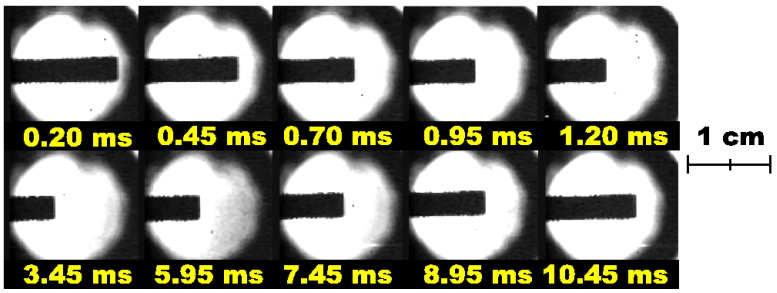


Figure 3.4: An example of the frame sequence showing the motion of the pin. The pin is a black rectangle observed in a back illumination. The valve located on the left is not shown. The corresponding frame times relative to the trigger signal are denoted.

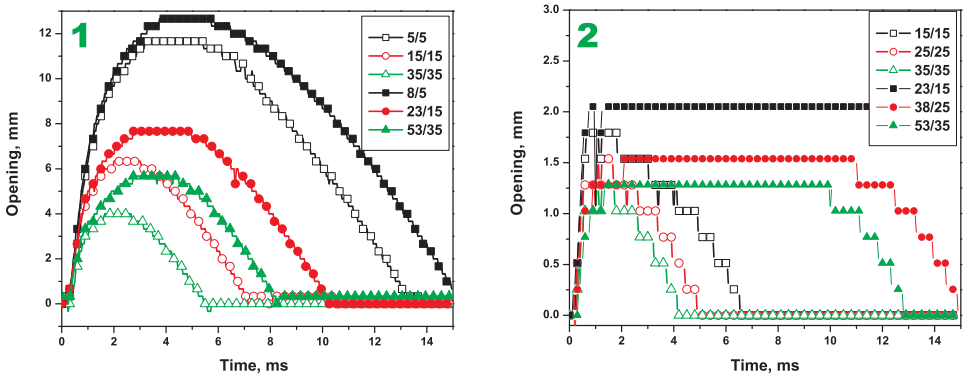


Figure 3.5: The dependence of the piston position on time for different pressures. 1 - "He/He"; 2 - "Ar/Ar". The pressures in the legends are indicated in the format $p_w/p_b$. The cases of $p_w = p_b$ ("equal") and $p_w = 1.5 \cdot p_b$ ("overpressure") are shown.

and friction pressures. Since the gas outflow rate is expected to grow with $p_w$, this motion and the valve closing take place earlier at higher operational pressures.

The similar dependencies are observed in the case of "Ar/Ar" experiments (fig. 3.5-2). However in comparing plots 3.5-1 and 3.5-2 the following two points are to be discussed. First, injection times in "Ar/Ar" experiments are comparable to that in the "He/He" set in spite of the expected slower decrease of $p_w$. The gas outflow velocity being of the order of sound speed $c_s$ is about three times less in the case of argon injection. And second, the piston is stopped much earlier and consequently the achieved valve opening is narrower. The explanation is likely to be related to the gas dynamics in the back section. Indeed, the time required for the equilibration of the argon pressure along both sides of the piston back part is found from the ratio of the back radius $r$ to the sound speed $c_s$. This value amounts to about 0.3 ms to be compared with the characteristic time of the problem 0.3 ms (fig. 3.2-3). Moreover the 1 mm narrow and several millimeters long separation gap between subsections "b" and "L" (fig. 3.1) is to aggravate the imbalance. The overpressure better evens the forces and provides the time for the back pressure relaxation, which leads to a dramatic performance improvement to be shown later. In helium experiments the pressures in the back part are equilibrated more effectively.

The described analysis leads us to conclude that helium is to be preferred in the back section. Confirming this conclusion is the other series of measurements performed with the different gases in the two chambers: "Ar/He", "He/Ar". The figure 3.6-1 shows the comparison of the time-position dependencies for all gas combinations at the fixed working pressure $p_w = p_b = 25$ bar. Reformulating the above made conclusion once more, helium in the back section provides the wider valve opening and prolongs the injection time. The difference in the slopes of the curves "He/He" and "Ar/He" (as well as "He/Ar"and "Ar/Ar") is caused by the difference in sound velocities. It is to be noted that the using of overpressure is always advantageous.

To perform estimations of the gas flow rates the injection durations were determined (fig.3.6-2). The accuracy of the data is specified mainly by the spatial resolution and constitutes approximately 0.35 ms. The end of the injection was not directly observed in the "Ar/He over" case due to the limited record length. The values were found by extrapolating the time-position curves with a second order polynomial. All main findings are clearly seen in this figure: the duration decreases as the pressure increases and the choice of the gas combination and overpressure factor plays a significant role. The argon tests appear to be more sensitive to the overpressure effect. Regimes with the same gases in both chambers are required as calibration data for TEXTOR experiments, that is why they were investigated also at lower pressures.

To sum up, to achieve better performance of the DMV it is advised to use helium in the

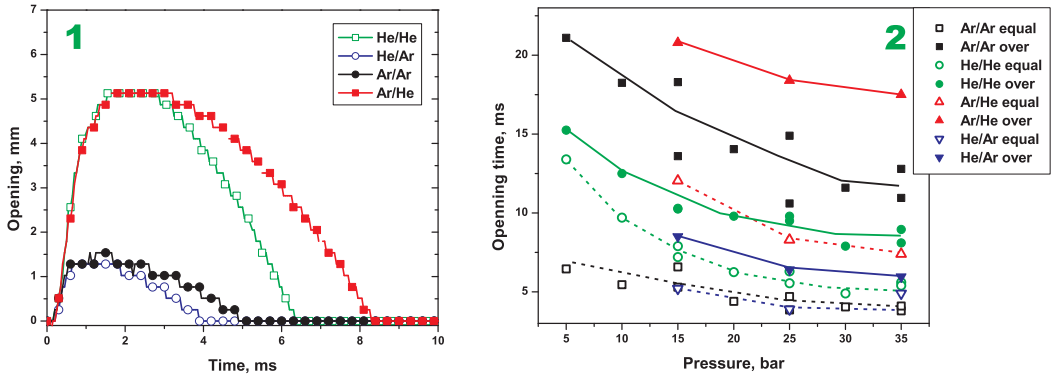


Figure 3.6: The effect of using He in the back chamber. 1 - the comparison of the piston position for different combinations of gases $p_w = p_b = 25$ bar; 2 - the comparison of the injection durations for different pressures and gasses. The notation: "the working gas / the gas in the back chamber"; "equal" - $p_w = p_b$; "over" - $p_w = 1.5 \cdot p_b$. Lines are to guide the eye only.

back section and the overpressure in the working chamber.

### 3.1.4 Valve efficiency, throughput and decay rate.

Before proceeding to measurements, the appropriate terminology is to be introduced. The simplest model assuming gas outflow with sound velocity $c_s$ from the volume $V$ through the hole of area $S_o$ leads to an exponential law of the particle content evolution:

$$\frac{dN}{dt} \approx -N \cdot \frac{c_s \cdot S_o}{V} \tag{3.8}$$

That is $N = N(0) \cdot \exp(-\alpha_{id} \cdot t)$, where $\alpha_{id} = c_s \cdot S_o/V$ is the ideal decay rate. It is reasonable to characterize the process by measuring $\alpha$. The value $1/\alpha$ reciprocal to the decay rate corresponds to the characteristic volume exhaust time. The a priori estimation for the used DMV gives decay rates of 0.22 $ms^{-1}$ for helium and of 0.07 $ms^{-1}$ for argon, or approximately 5 and 14 ms in terms of the exhaust times. The validity of the model has to be proven in the course of the analysis.

Let us first consider the valve efficiency. The dimensionless efficiency is defined as the amount of the injected particles relative to the initial particle content in the working chamber:

$$\mathrm{Ef} = \frac{p_w(0) - p_w(\infty)}{p_w(0)} = 1 - \exp(-\alpha \cdot t^*) \tag{3.9}$$

where $t^*$ is the injection duration. It is to be noted that the efficiency itself is easy to obtain, however here the simultaneous measurements of the injection time reveal the reasons of the observed tendencies. The results of the efficiency measurements are presented in fig. 3.7-1 for helium and 3.7-2 for argon. It can be concluded from the plots that the use of the overpressure or helium in the back section improves the efficiency by a factor between 1.5 and 3, the exact number depending on the particular conditions. There are only two ways to modify the efficiency either by changing the duration of the injection or by modifying the decay rate. The comparison of the injection time and efficiency behaviours makes it clear that the prevailing role is played by the change of the injection time. The modification of the decay rate does take place but amounts only to the relatively low value of 20% to be discussed below. We note also the simple relation between the total number of the injected particles also known as throughput and the efficiency:

$$\mathrm{Th} = \mathrm{Ef} \cdot p_w(0) \cdot V \tag{3.10}$$

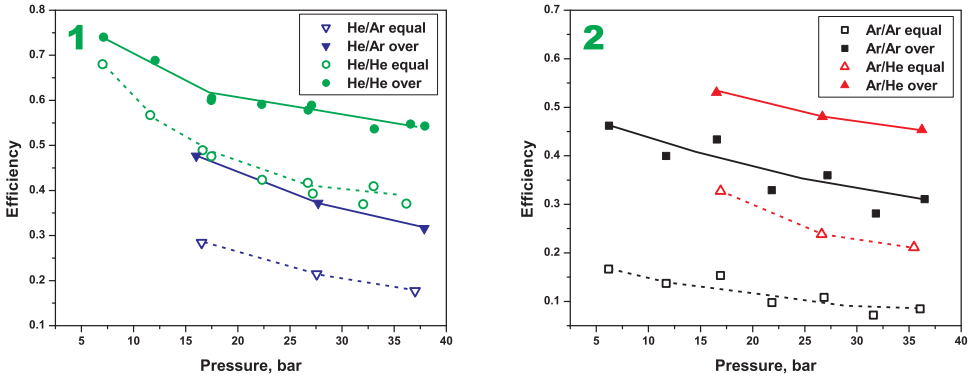


Figure 3.7: Efficiency of the valve as a function of the back pressure for different gas combinations. 1 - He as working gas; 2 - Ar as working gas. The notation coincides with that of fig. 3.6.

The maximum realized throughput is about 7.5 bar·l for argon and about 9.5 bar·l for helium[2].
To stay in the framework of the introduced model the decay rate is found from the experiment as:

$$\alpha = \frac{-\ln\left(\frac{p_w(\infty)}{p_w(0)}\right)}{t^*} = -\frac{\ln(1-\mathrm{Ef})}{t^*} \tag{3.11}$$

The dependence of the decay rate on the main parameters is illustrated in fig. 3.8-1, the error is about 5%. As expected for the given experimental conditions (the working gas, the back gas and the overpressure factor) the decay rate is a very weak function of the pressure, which confirms the validity of the used model. The still persisting pressure dependence is caused by the change of the piston stroke as the pressure changes. The abrupt drop at $p_b = 35$ bar for two points arises from the malfunction of the sealing separating back and working chambers, this fact could be already inferred from the corresponding injection duration measurements (fig. 3.6-2). The experimentally found decay rates differ by a factor of $2-2.5$ from the ideal estimation given above, while the ratio of He to Ar decay rates constituting 2.7 coincides with the sound velocity ratio $\approx 3.16$ within the accuracy of 15%. This discrepancy is to be attributed to the flow dynamics effects. The further clarification requires a detailed modeling of the outflow process.
It is to be noticed that the decay rate defined in such a way is an average over the whole piston motion. Equations 3.8 - 3.11 are easily generalized for the case of $\alpha$ changing in time:

$$N(t) = N(0)\cdot\exp\left(-\int_0^t \alpha(\tau)d\tau\right), \quad \frac{1}{t^*}\int_0^{t^*}\alpha(\tau)d\tau \equiv \langle\alpha\rangle = -\frac{1-\mathrm{Ef}}{t^*} \tag{3.12}$$

The mean decay rate $\langle\alpha\rangle$ coincides to the first order of accuracy with the value at the average opening:

$$\langle\alpha(h)\rangle = \frac{1}{t^*}\cdot\int_0^{t^*}\alpha(h(t))\cdot dt \approx \alpha(\langle h\rangle) + \left.\frac{\partial\alpha}{\partial h}\right|_{\langle h\rangle}\cdot\frac{1}{t^*}\cdot\int_0^{t^*}(h(t)-\langle h\rangle) + \\ + \left.\frac{\partial^2\alpha}{\partial h^2}\right|_{\langle h\rangle}\cdot\frac{1}{2t^*}\cdot\int_0^{t^*}(h(t)-\langle h\rangle)^2 = \alpha(\langle h\rangle) + \left.\frac{\partial^2\alpha}{\partial h^2}\right|_{\langle h\rangle}\cdot\frac{\sigma_h^2}{2} \tag{3.13}$$

In assessing the peak valve performance it is necessary to analyze the difference between the maximum and the average values. The in-depth study based on the knowledge of the function $\alpha(\langle h\rangle)$ (fig. 3.10) and on the measurements of the maximum opening leads to the

[2]with the volume of 320 ml used during tests

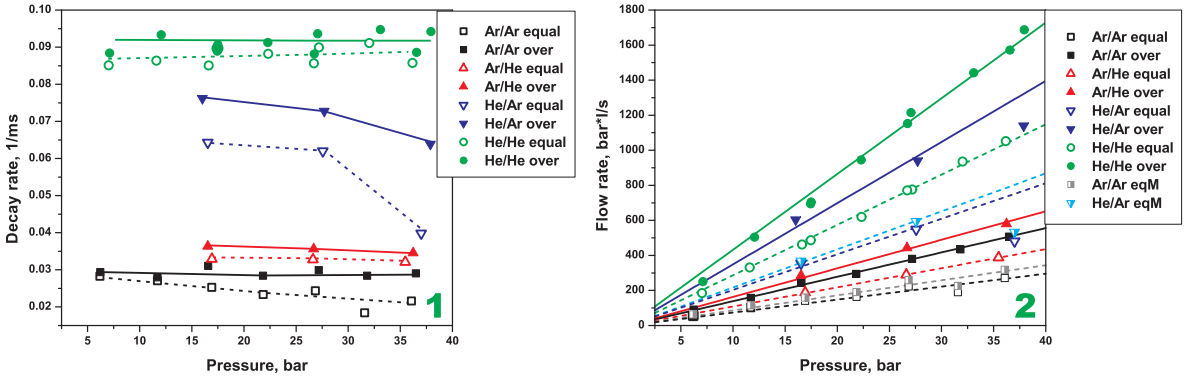


Figure 3.8: Time characteristics of the valve. 1 - decay rate as defined in the text. Lines are to guide the eye only.; 2 - ideal particles influx rate. The notation coincides with that of fig. 3.6. The curves marked "M" in plot 2 represent the estimation of the maximum outflow rate with the 1.2 modification factor derived in the text. Lines are the best linear fitting to the experimental points, the corresponding values are listed in table 3.1

conclusion that these changes remain at the insignificant several percent level for all cases with the exception of "Ar/Ar equal" and "He/Ar equal". In these two sets the maximum outflow could exceed for a short period of about 1 ms the average one by 20%. If the specified time is enough for the flow to form, this factor brings the maximum ratings of "*/Ar equal" set close to that of the "*/Ar over". Nevertheless the shown values are with good accuracy representative of the valve functionality. The use of helium in the back section is able to modify the decay rate by about 20%.

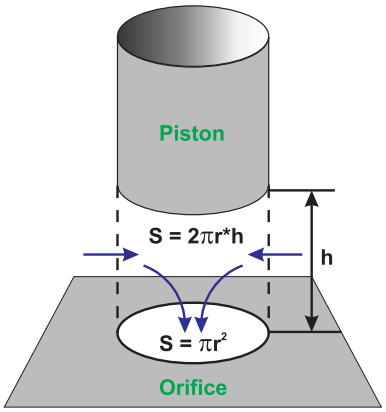


Figure 3.9: Comparison of the surface of the cylinder based on the orifice with the surface of the orifice itself.

The main reason of the low sensitivity of $\alpha$ to the substantial change of $h$ in using helium in the back section is the saturation demonstrated in the fig. 3.10. Correction of the dependence according to equation 3.13 with known $\sigma_h$ results in negligible effect and for this reason it is not discussed. When the surface area of the cylinder with the height $h$ based on the orifice of radius $r$ becomes comparable with the value $\pi \cdot r^2$, or $h = r/2 \approx 2.5$ mm, the flow is limited by the surface of the orifice, fig. 3.9. This moment is marked with the black vertical line in figure 3.10. In order to use the piston stroke effectively the orifice is to be extended by a factor about 2, which should correspond to the 4 times increase of the decay rate. The further modification of the diameter should cause only a linear effect on $\alpha$ since the flow would be limited by the opening width. A scrupulous analysis taking into account the flow dynamics as well as the piston mass modification is left for a future work.

The other important value intimately related to the decay rate is the ideal particle influx. That is the particle influx rate of the gas into the plasma if the valve were installed next to the plasma edge. This parameter does not depend on the volume of the valve and hence represents better way of describing all valves with similar orifice dimensions. The maximum influx is given by $V \cdot p_w(0) \cdot \alpha$. As the average opening is achieved on a timescale 0.5 ms being much shorter than the exhaust time, the use of $p_w(0)$ is justified with the accuracy better than 5%. The values expressed in bar·l·s$^{-1}$ are shown in fig. 3.8-2. Together with the usual data set the outflow rates for the cases "Ar/Ar equal" and "He/Ar equal"

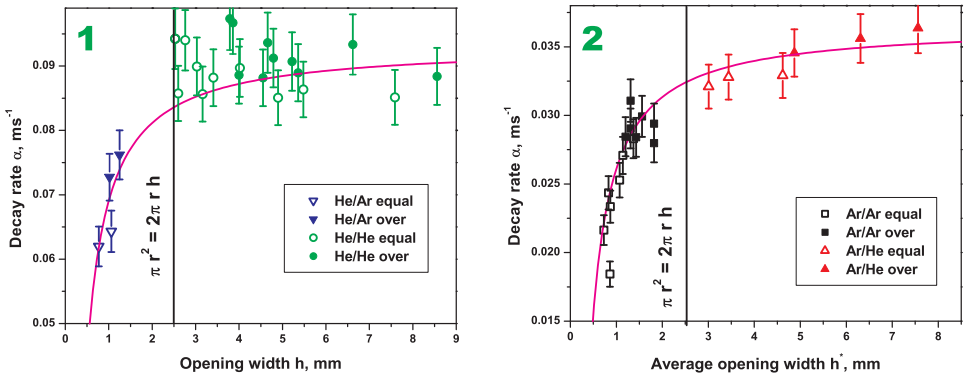


Figure 3.10: Dependence of the average decay rate on the average opening width. The fitting curve has form $a + b/x$. 1 - He as working gas, $a \approx 0.093$ ms$^{-1}$, $b \approx -0.0243$ mm·ms$^{-1}$; 2 - Ar as working gas, $a \approx 0.037$ ms$^{-1}$, $b \approx -0.0105$ mm·ms$^{-1}$. The black vertical line marks the opening from which the gas flow is limited by the orifice surface area.

modified by the factor 1.2 discussed above are given. The maximum achieved delivery rates are 500 bar·l·s$^{-1}$ for argon and 1500 bar·l·s$^{-1}$ for helium. The lines shown in the figure are the best linear fits to the experimental points, the corresponding fit coefficients are listed in table 3.1

Instead of looking at maximum ratings one can be interested in the delivery rate averaged

| Regime | k, (bar·l·s$^{-1}$)/bar |
|---|---|
| "Ar/Ar equal" | 7.4 |
| "Ar/Ar over" | 13.9 |
| "Ar/He equal" | 10.9 |
| "Ar/He over" | 16.3 |
| "He/Ar equal" | 20.3 |
| "He/Ar over" | 34.9 |
| "He/He equal" | 28.7 |
| "He/He over" | 43.2 |

Table 3.1: Best fitting parameters for the measured flow rates. Notation is the same as earlier. The flow rate can be found as $F = k \cdot p_b$. Note that this dependence is on the back pressure, that is why for overpressure cases $q = 1.5$ the fluxes are about one and half times higher.

over $t^*$: $(p_w(0) - p_w(\infty))/t^*$. The transition between this two definitions is straightforward, the correction factor being given by $Ef/(\alpha \cdot t^*)$, which is effectively in the range $0.5 - 1$ in the present measurements.

### 3.1.5 DMV at TEXTOR

The volume of the valve used at TEXTOR was reduced to about 30 ml to meet the requirements of the vacuum system: the maximal allowed transient pressure in the torus is limited by the mechanical properties of the turbo pumps to about $10^{-1}$ mbar. The reduction was realized by a cylinder like insertion into the originally 320 ml large reservoir. The insertion had a spatial groove to allow valve filling. In such a way dead unknown volume appeared. Additional dead volume was located in the filling valve. To find out the exact amount of injected particles test shots into the TEXTOR vessel were conducted. During

these experiments all torus valves leading to pumps were closed, so that the amount of particles could be easily determined by the pressure rise. Measurements (fig. 3.11) indicate that the effective volume is 53 and 44 ml for helium and argon correspondingly. The difference appears because of a slightly different efficiency and different flow rate into the working chamber from the dead volume. For the mixture case the volume can be scaled linearly with the sound speed.

The valve was installed at the top of the tokamak (TEXTOR section 7/8), as shown

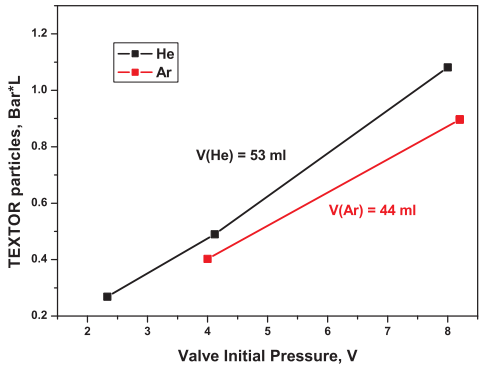


Figure 3.11: TEXTOR dry runs to determine the valve volume.

schematically in figure 3.12-1. The supply system allowed the choice of three different gases and pumping of both working and backing volumes. In the first campaign (TEXTOR discharges from 99681 to 101170) the valve was operated in the pressure range $p_w = 1.5 - 5$ bar, with $p_b$ being always equal to $p_w$. The gases used in both valve sections were always the same. It is to be noted that the performance deterioration with argon in the back section is not important for the small volume of the injector. The exhaust time is always shorter than the injection duration so that the bulk of particles was always injected.

Since the measurements of the valve properties indicate that the piston stroke in the base configuration is not used effectively, in the second campaign (TEXTOR discharges from 102509) the orifice diameter was doubled. The corresponding increase of the outflux rate should be 4, however calibration of the new system was not performed. The modified version of the valve had the same injection volume, but experiments were performed in a wider pressure range: $p_w = 5 - 20$ bar, the highest pressure corresponding to the limit of the vacuum system. The closing pressure in these experiments was always kept at 5 bar. The modification of the orifice allowed overpressure factors up to 4 to be used, in fact the upper boundary was not determined. In accordance with the calibration results the gas in the back chamber was chosen to be helium for all gas species in the working volume.

Figure 3.12-2 shows the particle flow rates for the operating modes used at TEXTOR. For the valve with increased orifice the values were estimated by applying the factor of 4 to the values measured with standard output nozzle in the overpressure case. Red vertical lines limit the pressure regions investigated in experiments for the two types of valves. Exhaust times are listed in table 3.2.

To distinguish the two different configurations of the valve they are designated as “x1” and “x4” for standard and enlarged orifice correspondingly.

| Mode | $\tau_{Exhaust}$, ms |
|---|---|
| “He/He x1” | 1.9 |
| “He/He x4” | 0.5 |
| “Ar/He x1” | 5.1 |
| “Ar/He x4” | 1.3 |

Table 3.2: Exhaust times for TEXTOR DMV.

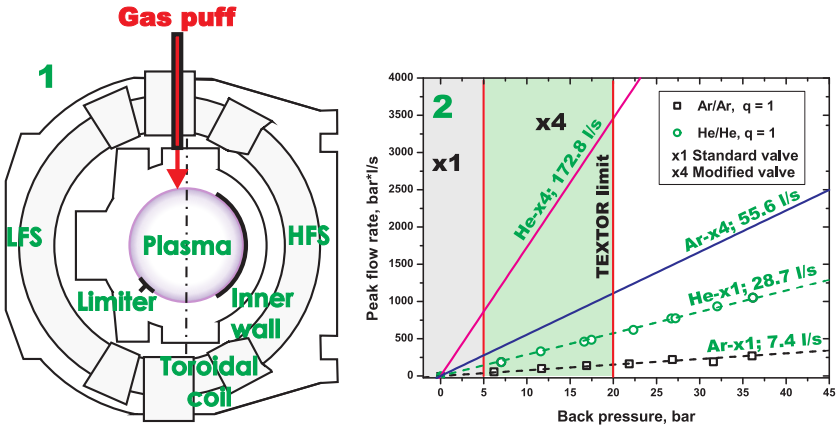


Figure 3.12: Disruption mitigation valve at TEXTOR. 1 - a schematic poloidal view of the valve installation at TEXTOR; 2 - gas flow rates. For the valve with increased orifice ("x4") the flow rates are estimated on basis of measurements with the standard configuration.

It is to be noted that the structure of the injection port is more complicated. To provide sufficient mechanical stability the liner is equipped with a rod exactly in the middle of the gas path (fig. 3.13-1, note the pronounced flow splitting at the presented camera frame). Influence of such flow disturbance consisting most likely of attached shock wave was not investigated. However the number of delivered particles is likely to be unchanged. Excluding some questions concerning the direct interaction of a dense jet with the plasma the rod nevertheless is not thought to affect the main conclusions made in the work. A qualitative independence of the sequence of events on the exact way of the gas delivery was confirmed in DIII-D with two configurations of the delivery tube. In the first case the tube was directed to the plasma edge, while in the second case it was aimed towards plasma center [97] (fig. 3.13-2). A direct experimental clarification at TEXTOR is planned for future experiments.

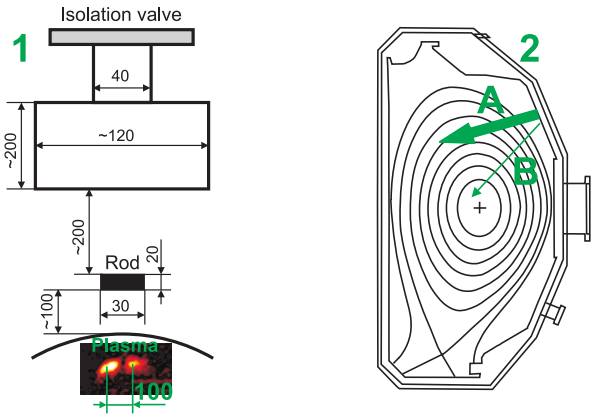


Figure 3.13: Injection port problem. 1- injection port. Under the schematic drawing the camera picture showing splitting of the jet is shown. 2 - the delivery tube configurations tested at DIII-D. The figure is reproduced after [97].

## 3.2 Ultra-fast framing camera

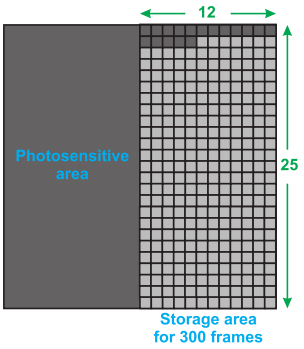


Figure 3.14: Construction of the camera pixel. The storage area consists of 12 columns and 25 rows.

In order to observe dynamics of the injected gas the fast framing CCD[3] camera PSI5 [112] sensitive mainly in the visible range was installed at TEXTOR. This camera has a chip with dimensions of $64 \times 64$ pixels and can run at frame rates up to 500 kHz. The problems with the charge transfer through the whole matrix at high frame rates are circumvented by storing data immediately in a pixel (fig. 3.14). After exposure a charge packet is quickly transferred to the adjacent storage area, the previously stored packets are shifted along the row. If the row designed for twelve frames is full the packets are simultaneously shifted vertically. The full storage area can accommodate up to 300 frames. When the whole frame sequence has been recorded, data are read out in a slow optimized way with typical duration of about a minute. To protect the stored data from illumination during the slow read-out the onboard memory is covered with non-transparent layer. The efficiency of this layer however degrades at high frame rates because of the ratio of the signal integration time to the read-out time being of the order of $10^7$. For this reason a fast mechanical shutter with a reaction time of about 10 ms is installed in front of the chip. Even in that case corruption of the "edge" frames[4] amounting up to 500 counts could be registered at the highest frame rate. The solution is to use an image intensifier as a gate. However this can potentially introduce a strong nonlinearity. Fortunately, for the disruption observation it is not important because of the lower used frame rates and the fast intensity drop on a timescale of several milliseconds. For the typical used frame period of 50 $\mu$s the mentioned effect is at the noise level of 20 counts, at the highest used frame rate of 100 kHz the effect may be as pronounced as 100 counts. It is to pointed out once more that this problem appears only at the "edge" frames. All camera parameters of interest are listed in table 3.3.

| Parameter | Value |
|---|---|
| Frame rate | $\leq$ 500 kHz |
| Spectral range | $\lambda = 300 \div 1000$ nm |
| Chip | $64 \times 64$ pixels |
| Pixel area | $200 \times 200$ $\mu$m$^2$ |
| Photosensitive area | 30.5% |
| Memory | 300 frames |
| Well capacitance | 8400 counts |
| Background | 800 counts |
| $\sigma_{Noise}$ | 20 counts |
| Working temperature | $-40$°C |

Table 3.3: Main parameters of the ultra-fast framing camera.

### 3.2.1 Camera tests

Before installation at TEXTOR the camera was extensively tested. The main tested parameters are actual frame rate, linearity and spatial uniformity of the chip sensitivity.

To test the frame rate a special shift array consisting of 16 fast light emitting diodes

[3] charge coupled device

[4] These frames are literally located at the edge, i.e. at the perimeter of the storage area where the transition from the covered zone to the photosensitive one takes place.

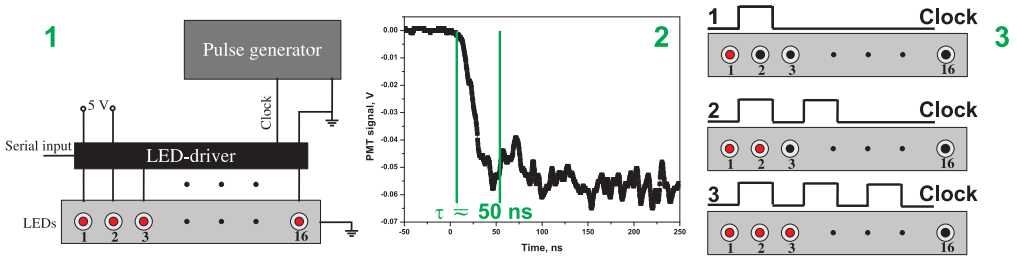


Figure 3.15: Camera testing facility. 1 - principal scheme of the LED shift array; 2 - rise time of the LED intensity as measured by a photomultiplier; 3 - illustration of the LED shift with every clock pulse. An emitting diode is shown in red.

(LED Hamamatsu 7868-02 [113]) was assembled, fig. 3.15. The array was controlled by the shift register Macroblock MBI5026 [114] clocked by a suitable pulse generator. The rise time of the selected photodiodes and the response of the electrical circuit are much shorter than any timescales in question: the growth of the diode intensity as measured by a photomultiplier is of the order of 50 ns only, fig. 3.15-2. When the clock pulse is received by the controlling chip, it turns on the next diode in the row, fig. 3.15-3. By appropriate choice of the clock frequency $f_{clock} < f_{frame}$ it was possible with this setup to measure the average frame rate. The measured frequencies are in very good correspondence with actual settings, fig. 3.16-1. Later in the experiments at TEXTOR the frequency was not controlled and the frame time was recovered under the assumption that the discrepancy between camera and TEXTOR clocks is negligible for 300 frames. In fact the last statement was confirmed once by recording the available strobe signals for every frame (signal "jdaq/DED/AUR14/5/PSI5" for TEXTOR shots 100926 ÷ 100940).

The linearity of the intensity scale was tested by illuminating one selected frame by a LED pulse of variable duration $T_{pulse} < T_{frame}$ and additionally by a variation of a gray filter in front of the camera. Figure 3.16-2 presents an example of the dependence of registered counts on the intensity expressed for convenience also in counts for the frame rate of 500 kHz. When the registered counts reach about 5000 (half of the full well), strong nonlinearity becomes evident. As it was found in more detailed investigations this phenomenon is related to the charge transfer inefficiency mainly in the vertical direction. For slower regimes $T_{frame} \geq 3$ $\mu$s the camera was found to be linear up to the full well.

Finally the spatial uniformity of the chip sensitivity was approved. The camera chip was

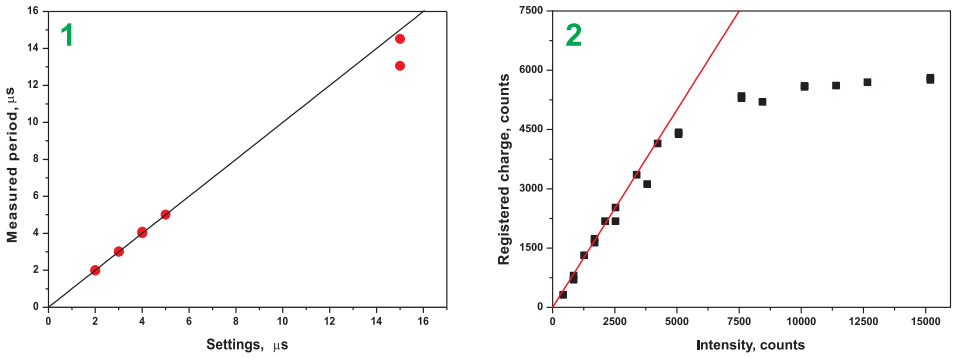


Figure 3.16: Camera testing results. 1 - comparison of the measured frame period with the settings. The discrepancy of the last two points is mainly due to bad determination of the driving clock for LED. The slower frequencies (as for example usually used in experiments 50 $\mu$s) were not tested, as it is believed that the problems, if they exist, should appear at the fastest frame rates. 2 - camera scale nonlinearity at the frame rate 500 kHz.

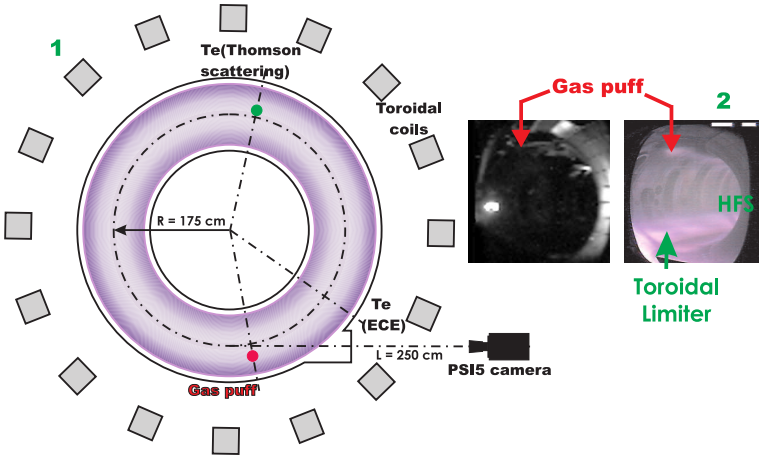


Figure 3.17: Camera view. 1 - top view of the tokamak. Indicated are positions of the injection port and temperature measurements diagnostics; 2 - comparison of the fast camera view (vessel is illuminated by the lamp) and the picture from the standard color camera during TEXTOR discharge.

illuminated by a uniform radiation field (Ulbricht sphere). The results indicated a 10% variation of the chip sensitivity from the top to the bottom. The data presented in the following chapters are corrected for this variation.
During the tests it was found that every twelfth frame has lower intensity and every frame with number $12 \cdot n + 1$ has higher intensity than the others. The half-sum of these two "edge" frames almost coincides with the average. The phenomenon is thought to be related to the timing problems during the vertical shift of charge packages taking place exactly at every twelfth frame: the exposure time of the last frame in the row is shorter than the average one and vice versa for the following frame. These two frames are substituted by their half-sum.

### 3.2.2 Fast camera at TEXTOR

The camera was installed to view the gas injection port tangentially, fig. 3.17. To reconstruct geometry of the view, e.g. to trace the $q = 2$ flux surface, parameters of the optical system have to be determined. In reality the optical system is very complex and has too many parameters to be extracted. The light first passes through an objective positioned immediately behind the vacuum window, afterwards the horizontal direction is rotated by a mirror and the light is collected by a field lens. At the distance of about 3 m from the field lens a vertical mirror is located. The final image is formed by the objective mounted on the camera. To facilitate the task the whole optical system was substituted by one "effective" thin lens. The parameters of this lens (focus distance, position, inclination angles) were chosen in such way as to match known points in the physical space with their image, an example of such mapping is given in figure 3.18. The reconstructed elements are the inner wall, the fifth blade of toroidal limiter, port in the liner section 20 and the ICRH antenna. Positions of these elements predicted by the chosen set of lens parameters are highlighted by the cyan dots. Since the camera was removed after each shot day the fitting procedure had to be repeated for every configuration.
To observe dynamics of a particular ionization stage the camera was equipped with interference filters. The list of used interference filters can be found in table 3.4.

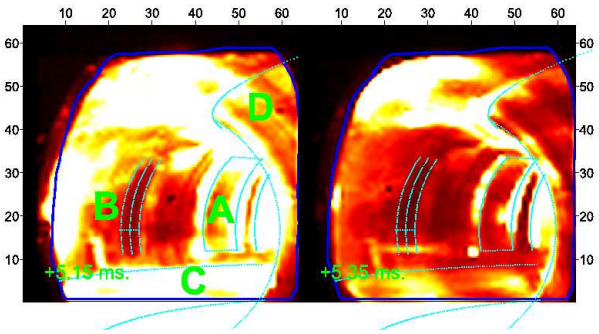


Figure 3.18: Geometry matching by choosing the lens parameters. With letters the following components are marked: A - ICRH antenna; B - port in the liner, the TEXTOR section 9/10, the liner section 20; C - the toroidal limiter ALT-2, blade 5; D - the bumper limiter. Cyan dots represent mapping of the physical space onto the image plane.

| $\lambda_{filter}$, nm | $\lambda_{Ion}$ | Ion | Transitions | Designation |
|---|---|---|---|---|
| 656 | 656.3 | D | 2 [s $^2$S, p $^2$P] - 3 [s $^2$S, p $^2$P, d $^2$D] | $D_\alpha$ |
| 465 | 465 | C III | $1s^2 2s3s\ ^3S$ - $1s^2 2s3p\ ^3P$ | CIII |
| 706.5 | 706.5 | He I | $1s2p\ ^3P$ - $1s3s\ ^3S$ | HeI 706.5 |
| 728 | 728.1 | He I | $1s2p\ ^1P$ - $1s3s\ ^1S$ | HeI 728 |
| 468.5 | 468.5 | He II | $3p\ ^2P$ - $4d\ ^2D$ | HeII |
| 442 | 442.6 | Ar II | $3s^2 3p^4(^2P)4s\ ^4P$ - $3s^2 3p^4(^3P)4p\ ^4D$ | ArII 442 |
| 610.9 | 611.5 | Ar II | $3s^2 3p^4(^1D)3d\ ^2G$ - $3s^2 3p^4(^1D)4p\ ^2F$ | ArII 611 |
| 696.5 | 696.5 | Ar I | $3p^5(^2P_{3/2})4s\ ^2[3/2]$ - $3p^5(^2P_{1/2})4p\ ^2[1/2]$ | Ar I |

Table 3.4: List of used interference filters. $\lambda_{filter}$ - central wavelength of the filter; $\lambda_{Ion}$ - wavelength of the observed transition. Transitions and wavelengths are listed according to NIST and CHIANTI databases [115, 116]

## 3.3 Essential diagnostics and their limitations

In the following chapter it will be shown that the MGI experiments can be subdivided into four main stages: propagation of gas through the delivery tube, cooling of the plasma edge (predisruptive phase), thermal quench (TQ), current quench (CQ). The extreme nature of disruption limits the applicability of many standard tokamak diagnostics only to the predisruptive phase or requires some unusual processing techniques. On the other hand, for example analysis of runaway electrons requires such special techniques as detection of the synchrotron emission and registration of the neutron fluxes. To explain the limits and interpretation of the data the most essential diagnostics are considered below.

### 3.3.1 Electron cyclotron emission (ECE)

Emission of electrons at the harmonics of their cyclotron frequency $\omega = eB_t/(\gamma mc)$ is widely used for temperature measurements [117]. The variation of the toroidal magnetic field with radius allows measurements of the local temperature by sensing a suitable frequency:

$$r = R_0 \cdot \left( n \cdot \frac{eB_t(R_0)}{\gamma mc\omega} - 1 \right) \tag{3.14}$$

Where $n$ is the number of the used harmonic and $\omega$ is the sensed frequency. The measurements at TEXTOR are conducted at the second harmonic.
If the emitting region is optically thick, the temperature can be easily extracted from the Rayleigh-Jeans approximation:

$$I_\omega = \frac{\omega^2 T_e}{4\pi^3 c^2} \tag{3.15}$$

To correct for the finite thickness in the opposite case complimentary density measurements are required. The second harmonic is usually thick, while the third one is not. Note also, that the data presented in the thesis are always normalized to the predisruptive values. The absolute values of temperatures from the ECE measurements are not used.
During the massive gas injections the ECE measurements can fall into cut-off. The cut-off was unambiguously confirmed in the experiments with helium by comparing the second and the third ECE harmonics. In the other experiments the problem does not seem to show up at least in the predisruptive phase. To exclude any mistakes the ECE measurements are not used in the thermal quench phase. In the predisruptive phase the conclusions drawn from the ECE data are supported by measurements with Thomson scattering. For a more detailed discussion of the cut-off see section C.

### 3.3.2 Thomson scattering

Thomson scattering is scattering of the light on free charged particles [118]. By sending a laser beam through the plasma it is possible to extract both the local electron temperature and electron density. The electron temperature can be determined from the Doppler broadening of the spectrum, while the density measurements are based on the absolute calibration of the system.
At TEXTOR the multi-pulse Thomson scattering system working with ruby laser is available [129]. The system provides profiles over the full plasma extent along the line passing vertically 9 cm away from the geometrical vessel center (towards low field side). Profiles are taken every 200 $\mu$s, with an exposure time of one frame being about 2 $\mu$s. Between two frames the plasma light is recorded which is subtracted in the post-pulse analysis. This scheme works reliably provided the signal/noise ratio is high enough after the substraction of background.
In disruption mitigation experiments the plasma light should be considered properly. Cooling of the plasma and the presence of a large amount of impurities result in the plasma emission varying in time and make the usual substraction of the frame following the signal one inapplicable. For this reason the plasma light to be subtracted from the signal frame

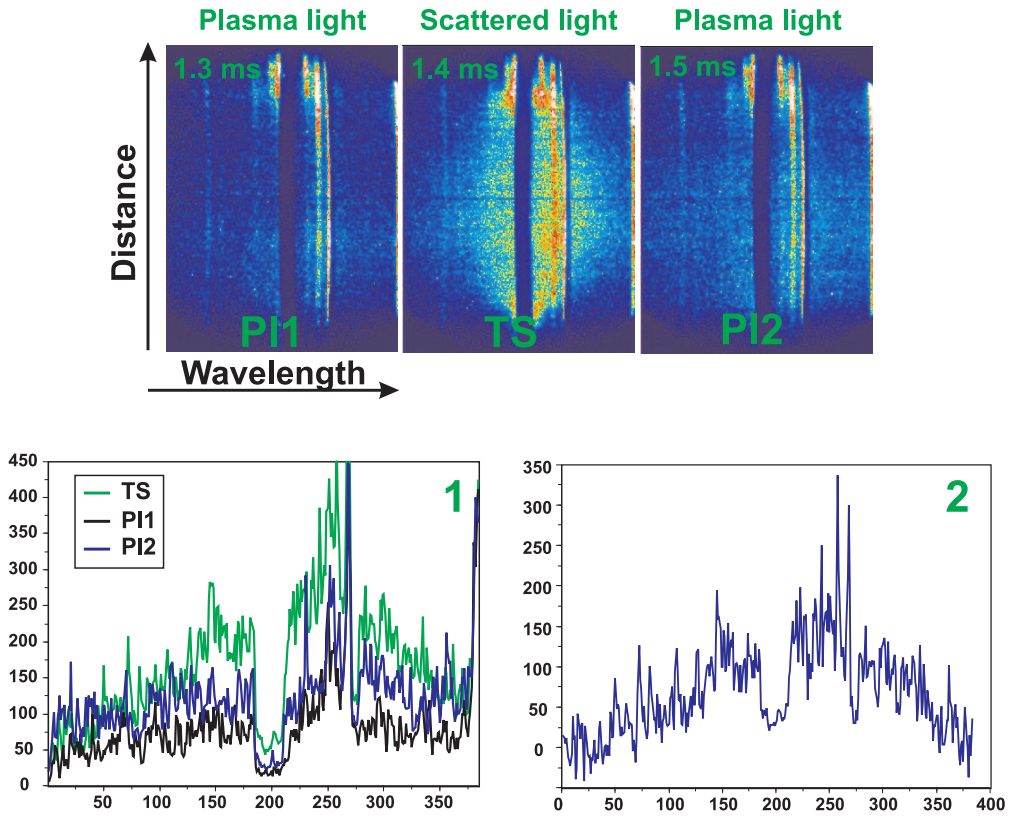


Figure 3.19: An Example of the raw Thomson scattering data. TEXTOR shot 102517, injection of 20 bar of He "x4". "TS" - scattered signal; "PL" - plasma light. 1 - 1D scans of: the plasma light taken at $t$ = 1.3 ms, plasma light taken at 1.5 ms and the frame containing useful scattered laser light. 2 - Thomson scattering signal corrected for the plasma light. The plasma light was averaged over the frame preceding and the frame following the signal frame.

was determined from linear interpolation between the frame preceding and the frame following the signal one. Such algorithm fails if the detector (camera pixel) falls into saturation. The last frame allowing reliable measurements is usually taken at the onset of thermal quench.
An example of the raw Thomson scattering data is presented in figure 3.19. The plots marked as "PL1" and "PL2" show the varying plasma light and the plot "TS" shows the Thomson scattered signal. The horizontal direction represents wavelengths, while the vertical one is the spatial position. Two vertical black stripes are due to the notch filters eliminating the light at the laser wavelength and the $H_\alpha$ plasma line. The variation of the plasma light is seen in subfigure 1 showing the 1D scans taken at the center of the discussed frames in spectral direction. The scan corrected for the plasma light interpolated linearly is plotted in subfigure 2.

### Energy content

The electron temperature and density are used to calculate the energy content of the discharge and the energy lost in the predisruptive phase. Under the assumption that the ion and electron temperatures are equal the thermal energy $E_{th}$ is given by:

$$E_{th} = \int_v 3 n_e T_e d^3 V \tag{3.16}$$

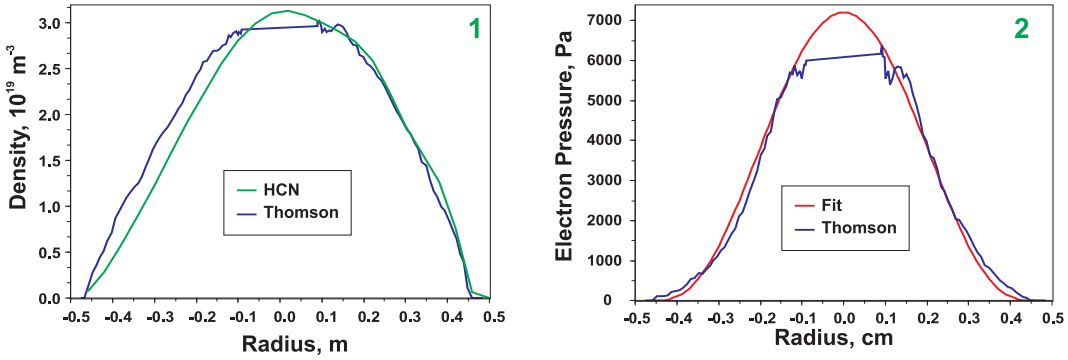


Figure 3.20: Estimation of the stored energy. 1 - comparison of the densities measured by Thomson scattering by Abel inversion of the data from the HCN interferometer. 2 - electron pressure. "blue" - Thomson scattering measurements, "red" - fit in the form $p(0)\cdot(1-(r/a)^2)^3$

To correct for the uncertainties in the absolute calibration, the density profiles obtained with Thomson scattering were rescaled to match the line integrated density measured by the HCN interferometer at $R$ = 185 cm in the stable phase of the discharge. The profiles obtained with the Thomson scattering are in a good agreement with those extracted by Abel inversion from the multichannel HCN interferometer (fig. 3.20-1). It is to be noted that the radius in figure 3.20 is defiened relative to the center of the vessel (major radius $R_0$ = 175 cm). The resulting electron pressure $p_e = n_e T_e$ is plotted in figure 3.20-2. In view of the absence of the measurements in the center and to facilitate calculations, the experimental profile is fitted by $p_e(r) = p(0)\cdot(1-(r/a)^2)^3$, where $a$ = 0.46 m is the plasma minor radius. The straightforward calculation results in the energy content of 40 kJ. About 5 kJ of this energy is localized outside of the $q = 2$ flux surface ($r \geq 30$ cm).

### 3.3.3 Soft X-ray camera

Emission from plasma in the soft X-ray range (100 eV $\gtrsim \hbar\omega \lesssim$ 10 keV) arises from the Bremsstrahlung of thermal electrons on ions, recombination and line emission. The SXR emissivity is strongly peaked in the plasma centre, e.g. the emissivity $\epsilon_\omega$ of the Bremsstrahlung for the plasma having Maxwellian distribution function is given by [5, 119, 120]:

$$\epsilon_\omega \sim n_e n_i Z^2 T^{-1/2} e^{-\frac{\hbar\omega_f}{kT}}, \tag{3.17}$$

where $\hbar\omega_f$ is the lower registerable energy that is specified by the filter ($\hbar\omega_f \approx$ 1000 eV for 10 $\mu$m Be filter at TEXTOR). That is why this spectral range is suitable for reliable diagnosing of the plasma center.

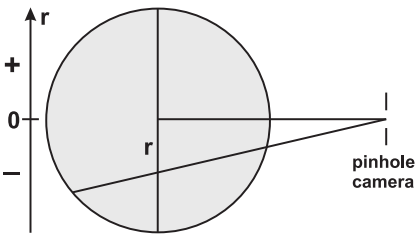


Figure 3.21: SXR camera geometry. "r" is the radius found in figures later.

During the disruption mitigation experiments the soft X-ray system at TEXTOR included two horizontal pinhole cameras providing in total 32 spatial channels for the plasma cross section $r \lesssim$ 40 cm [121]. Since the data are line integrated along the line of sight, the "radius" to be found in figures later designates intersection of the chord with the vertical diameter (fig. 3.21).

The system has a superior time resolution of about 20 $\mu$s. However, in the experiment the absolute timing had to be corrected for an uncontrolled jitter of the system clock. To correct the timing the SXR signal was shifted to match the last sawtooth crash before the gas puff. The accuracy of such a method is of the order of 100 $\mu$s.

### 3.3.4 Synchrotron emission

A charge rotating toroidally experiences a constant acceleration and consequently emits electromagnetic waves referred to as synchrotron radiation [122]. Synchrotron emission of runaway electrons has been known and used for their diagnostics since long time [54, 123, 124, 125]. If the velocity of the particles is relativistic the light is emitted in forward direction in a thin cone with angle of the order of $1/\gamma$ [118, 126], where $\gamma$ is the energy expressed in masses $\gamma = \varepsilon/(m_e c^2)$. This allows one to obtain a poloidal distribution of the particles, since the signal is formed only in a very narrow region and the problem of convolution (line integration) does not appear.
At TEXTOR the measurements of synchrotron emission are conducted with the aid of the fast framing infrared ($\lambda = 3 \div 5$ $\mu$m) camera viewing tangentially the central part of the discharge. The observable region of the discharge is about $30 \times 30$ cm. At present only the relative uncalibrated intensity is used. It is to be noted that the frame also contains some poorly understood reflections on the vessel structures, which however does not affect the main conclusions to be drawn later.
Emission in the range $\lambda = 3 \div 5$ $\mu$m is typical for high energy electrons. Indeed, the spectral distribution of synchrotron emission is given by [122, 126]:

$$I(\omega) = \sqrt{3} \cdot \frac{e^2}{c} \cdot \gamma \cdot x \cdot \int_x^\infty \mathrm{K}_{5/3}(\xi) d\xi$$
$$x = 2\frac{\omega}{\omega_{cr}}, \quad \omega_{cr} = 3\gamma^3 \frac{c}{R_0} \tag{3.18}$$

where $K_{5/3}(x)$ is the modified Bessel function of the second kind. The appearance of the term $\gamma^3$ in the critical frequency is explained by the fact that the radiation emitted by a fast moving electron is registered by a detector only for a short time $\sim 1/\gamma$. After transformation to the laboratory frame of reference this results in a strongly widened spectrum $\sim \gamma^3$ [126]. The emission is at maximum at $\omega/\omega_{cr} \approx 0.29$ and decays exponentially at larger values of the argument (fig. 3.22-1). Assuming that the emission is significant at most at one e-folding length one can estimate the energy required for an electron to be visible in the range $\lambda = 3 \div 5$ $\mu$m: $\varepsilon \approx 40$ MeV. Because of the relation $\gamma \sim (y)^{1/3}$ the resulting energy has only a weak dependence on the exact value of $\omega/\omega_{cr}$ assumed in the estimation. A more thorough analysis should take into account the sensitivity of the detector and also the change of the trajectory curvature due to the gyration around the field line [123]. The found value is, however, representative within a factor of 2. The time for an electron to

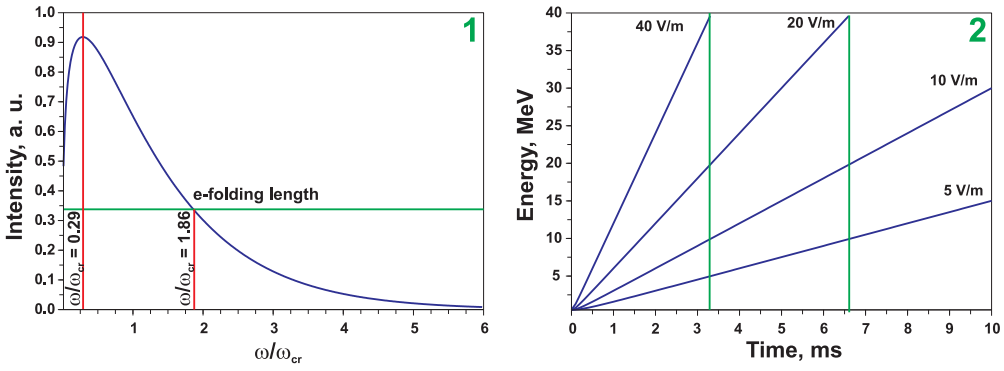


Figure 3.22: 1 - spectral distribution of synchrotron emission (eq. 3.18); 2 - dependence of the electron energy on time in uniform electric field.

reach such energy can be found from (fig. 3.22-2):

$$\varepsilon = \sqrt{\varepsilon_0 + (ceEt)^2} \approx ceEt \tag{3.19}$$

For typical fields of the order of $20 - 40$ V·m$^{-1}$ to be expected in the current quench the time is of the order of $3 \div 6$ ms. This estimation is in correspondence with the experiment: the observed signal doubling time is about 4 ms (section 4.3.2). Such high electric fields remain only for a few milliseconds, so that this diagnostics is sensitive only to the high energetic part of the runaway population formed mainly at the very beginning of the CQ.

### 3.3.5 Neutron detectors

An alternative way of registering fast electrons is to use standard neutron detectors. The TEXTOR detectors are of liquid scintillator type in which a neutron produces a recoil proton. The fluorescence light from the molecules excited by that proton is registered by a photomultiplier. The diagnostics is also sensitive to hard $\gamma$ photons that are able to release electrons. Since both types of events are not discriminated, the final signal represents the sum of neutron and $\gamma$ fluxes. It is to be stressed that the $\gamma$ flux is attenuated by a lead shielding.
As for the origin of $\gamma$ and neutron emission, hard electromagnetic emission is produced as the Bremsstrahlung radiation in collisions of fast electrons with heavy atoms. If the energy of the produced quantum is higher than the binding energy in a nucleus, a neutron can be knocked out - nuclear photoeffect. The mean binding energy in nuclei is about 8 MeV and consequently this diagnostics is sensitive to the high energetic part of the runaway population $\varepsilon \geq 10$ MeV.
These processes along with K-shell vacancies production can take place in the plasma owing to the presence of impurities. Consequently they can be used for the direct diagnostics of runaway electrons in flight [135, 136]. However, because of the much higher density of the matter the signal is much stronger if a runaway electron is lost to the wall. That is the detected signal mainly reflects the loss rate of runaway electrons. The integral of the signal approximately gives the total number of produced runaway particles with high energies. It is worth mentioning that the characteristic $\gamma$-spectrum of walls activated by runaway electrons can be used for the diagnostics of electrons energy [134]. This possibility was not used in this thesis.
The main disadvantage of this diagnostics is its proneness to the saturation at high count rates. To be aware of it two detectors having different sensitivities (the TEXTOR signals "star/neu_3" and "star/neu_4") have to be compared. If both signals reveal the same trend the linearity is thought to be confirmed. Otherwise the interpretation of the data is troublesome.
In this work only a relative variation of the signals is discussed. The calibration of detectors was obtained for a uniform toroidal distribution of neutron source, which is not fulfilled fot runaway discharges. Due to the variation of distance and the presence of transformer yokes and other thick elements the toroidal position of the source is known to have a large influence on the absolute signal [137].

## 3.4 Position of the $q = 2$ flux surface

The $q = 2$ flux surface turns out to be important for the destabilization of plasma by the massive gas injection. In this section the position of this surface is determined.
In principle, one has to distinguish the position of $q = 2$ in the stable discharge and that in the discharge with the cooled edge. For the MGI experiments it is the second option that is more relevant. In this case the current has sufficient time to diffuse into the core (see discussion of the skin time in section 4.2.4). Thus, the position of $q = 2$ is in fact the radius of the plasma column carrying the full plasma current and having the edge safety

factor equal to 2 (SI units):

$$r_{q=2} = \sqrt{\frac{qR_0\mu_0 I}{2\pi \cdot B_t}} \approx 33 \text{ cm} \tag{3.20}$$

The accuracy of the measurements done with the fast camera is of the order of the spatial resolution 1.5 cm. The statement that the gas emission is registered at $q = 2$ is to be understood with this error bars. With the same accuracy the ECE channel corresponding to $q = 2$ is chosen to be the one at $r = 31$ cm.

# Chapter 4

# Experimental results

Main results obtained during experimental campaign are presented and discussed.

## 4.1 Predisruptive phase

This stage is characterized by cooling of the outer plasma region being in the direct contact with injected atoms. The plasma core remains unaffected as long as the $q = 2$ flux surface is preserved.

To confirm dynamics of the cold front in the predisruptive phase, the Thomson scattering measurements are analyzed, fig. 4.1. The data for helium, argon and 10% mixture of argon puffs are presented in dependence on the distance along the laser beam relative to the equatorial plane. The negative distances correspond to the points below midplane and the positive ones represent points above. In all cases the temperature profile shrinks towards the center. At the same time the central temperature remains at high level, this fact has already been confirmed by ECE measurements. The data taken just prior to the TQ reveal that the cold front is located around the $q = 2$ flux surface ($r \approx 33$ cm). The onset of TQ (profiles "TQ") is characterized by abrupt changes in the region $q < 2$. The following dynamics can not be traced reliably because of the overwhelming plasma light and the associated large error bars $\delta T_e > T_e$. The described sequence of events is typical for all experiments without any exceptions. Thus, the propagation of the cold front at the plasma edge and its penetration only up to $q = 2$ are confirmed.

As for the density dynamics, in the cases of the pure argon and 10% argon mixture injections the density remains alsmost unchanged before the thermal quench. In the helium case and only in that case "ears" appear at the plasma edge. These peaks are located at the $q = 2$ flux surface before the TQ and decay in few centimeters towards the plasma center. The difference in density dynamics between experiments with different gases can be explained by two facts. Firstly, the cold cloud can be more localized toroidally for the havier argon: the Thomson scattering system is almost 180 degrees toroidally away from the injection port, fig. 3.17. And secondly, argon and 10% mixture possess high radiative cooling capability, while helium cools the plasma mainly by dilution, consequently a big fraction of helium should be kept ionized. In any case, the injected gas does not penetrate deep inside the $q = 2$ flux surface before the disruption.

It is worth noting that in the argon experiments the central electron density decreases by about 15% before the final collapse. That is, in spite of preserving the temperature the core seems to loose about 5 kJ out of 35 kJ stored thermal content. In principle, one can not exclude a contribution of the plasma light to this effect, nevertheless, to exclude any mistakes this lost energy is taken into account in the energy balance discussed in section 4.1.3. If the injected gas is helium or a 10% mixture of argon, this phenomenon is not pronounced.

The cooling is likely to be a result of the direct contact of hot plasma with the injected atoms. A qualitative correlation between the cooling front and the emission front of singly ionized species is illustrated in figure 4.2. The equivalence of the emission front and gas penetration will be discussed later (section 4.1.3). Only upper parts of the frames, where the emission is observed, are shown. Since at the beginning it is impossible to discriminate the toroidal and poloidal motion of the cloud, for every frame the flux surfaces $r = 43$ cm ("green") and $r = 37$ cm ("cyan") are indicated at two toroidal positions. The bigger circle of a particular color corresponds to the toroidal position of the injector and the inner one is located in the plane parallel to the lens. In all cases, at the moment when the flux surface $r = 43$ cm is cooled down (the exact times are listed in the caption), the maximum of registered intensity lyes at $r = 43$ cm at the toroidal position of the injector or somewhere between that position and the plane parallel to the lens. Later when the surface $r = 37$ cm is cooled down, the emission front extends to this surface, with this fact being most pronounced for the shot shown in figure 4.2-2. A more precise conclusion about position of the emission front can be drawn for the cooling of the $q = 2$ flux surface. The delay between arrival of the cold and emission fronts to $q = 2$ is as short as the time resolution of the ECE diagnostics - 100 $\mu$s, see section 4.1.4.

The camera images also confirm that the injected atoms stay outside of the $q = 2$ flux

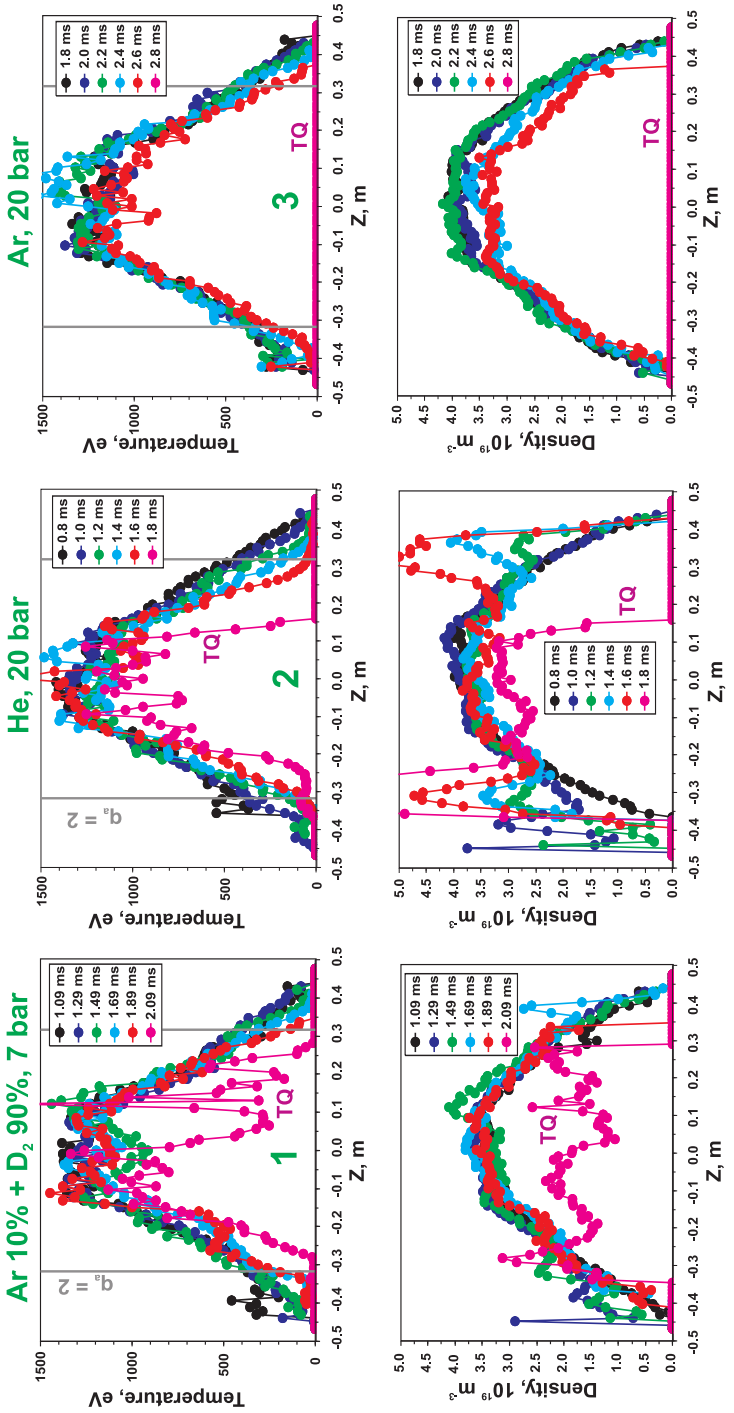


Figure 4.1: Results of Thomson scattering measurements in predisruptive phase. $Z$ is distance along the laser beam relative to the equatorial plane. 1 - TEXTOR shot 102510, injection of 7 bar of Ar10%+$D_2$90% "x4". Gas arrived to the plasma edge at $t_G$ = 0.84 ms, TQ started at $t_{TQ}$ = 2.1 ms. 2 - TEXTOR shot 102517, injection of 20 bar of He "x4". Gas arrived at $t_G$ = 0.76ms, TQ started at $t_{TQ}$ = 1.7 ms. 3 - TEXTOR shot 102526, injection of 20 bar of Ar"x4". Gas arrived at $t_G$ = 1.6 ms, TQ started at $t_{TQ} \approx$ 2.7 ms.

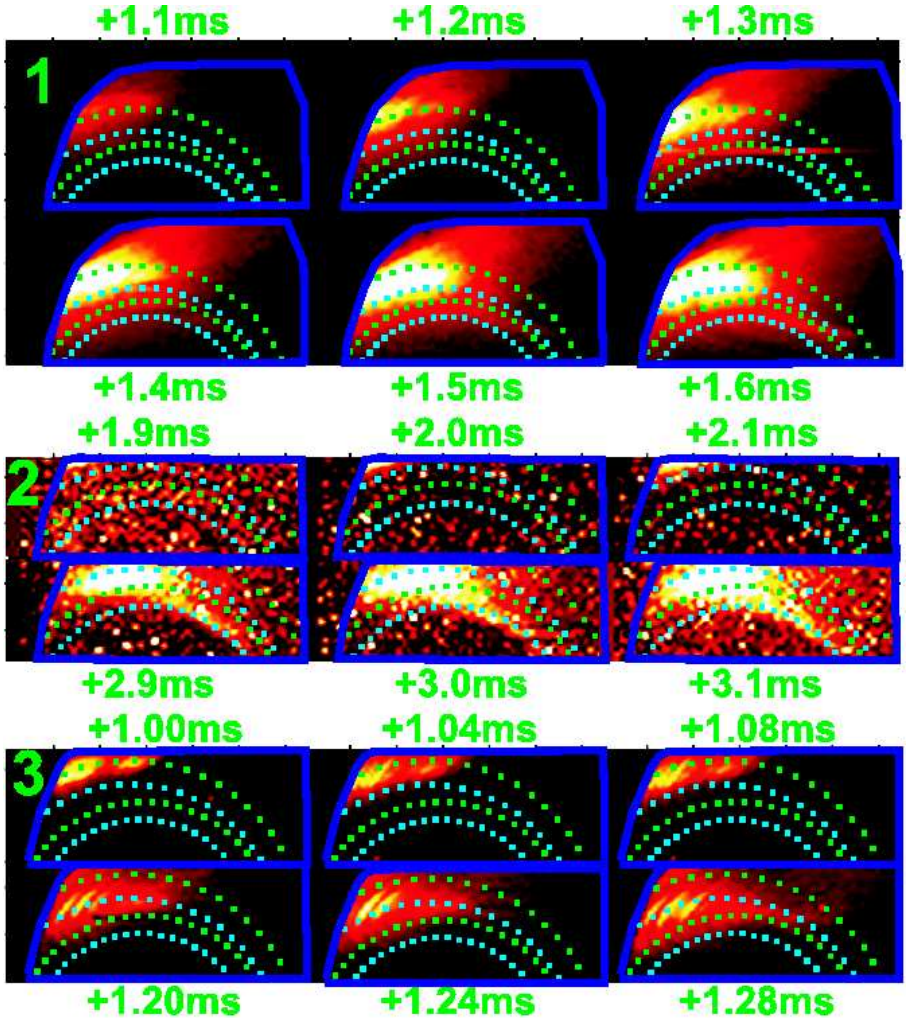


Figure 4.2: Emission in predisruptive phase. 1 - TEXTOR shot 99688, injection of 1.5 bar of He "x1". Observations were made in HeII light. The temperature started to drop at: 1.2 ms for $r = 43$ cm and 1.49 ms for $r = 37$ cm. 2 - TEXTOR shot 100930, injection of 3 bar of Ar "x1". Observations were made in CIII light. The temperature started to drop at: 1.95 ms for $r = 43$ cm and 3.03 ms for $r = 37$ cm. 3 - TEXTOR shot 102519, injection of 10 bar of Ar10%+$D_2$90% "x4". Observations were made in ArII 611 light. The temperature started to drop at: 1.03 ms for $r = 43$ cm and 1.23 ms for $r = 37$ cm. Dark blue mask outlines window. Green points designate the flux surface $r = 43$ cm at two toroidal positions. The first position (larger circle) is at the location of the injection port and the second one (smaller circle) is in the plane parallel to the lens. Cyan points are the same as green ones but for $r = 37$ cm.

surface before the thermal quench. Just before the disruption the emission front surrounds the $q = 2$ flux surface, which corresponds to the deepest penetration of the emission front, fig. 4.3. The structure of the figure is essentially the same as described above, but the flux surface plotted here is $q = 2$. The precise location of the emission could be extracted owing to a more uniform poloidal as well as toroidal gas spreading. This conclusion was drawn from the analysis of about 50 discharges terminated by different gases and has only few exceptions (see section 4.1.1). However, as low intensity is also registered in the center of the image, especially in subfigures 1,2 ,4, it could be argued that the determined penetration depends on the system sensitivity. To answer this question the camera frames were reconstructed for a model distribution of the injected gas.

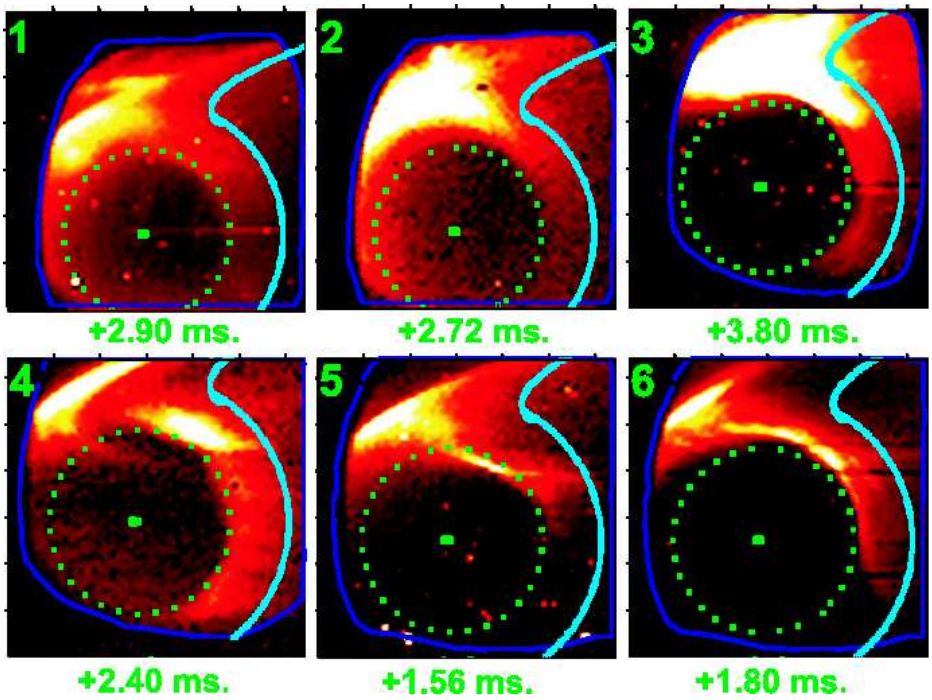


Figure 4.3: Position of the emission front at the onset of TQ. 1 - TEXTOR shot 99681, injection of 1.7 bar of He "x1". Observations were made in $D_\alpha$ light. TQ started at 3.2 ms. 2 - TEXTOR shot 99683, injection of 1.9 bar of He "x1". Observations were made in HeI 706.5 light. TQ started at 3.0 ms. 3 - TEXTOR shot 100165, injection of 3 bar of Ar "x1". Observations were made in ArII 442 light. TQ started at 4.1 ms. 4 - TEXTOR shot 101147, injection of 3 bar of Ar5%+$D_2$95% "x1". Observations were made in CIII 465 light. TQ started at 2.5 ms. 5 - TEXTOR shot 102518, injection of 20 bar of He "x4". Observations were made in HeII 468 light. TQ started at 1.6 ms. 6 - TEXTOR shot 102520, injection of 6.4 bar of Ar10%+$D_2$90% "x4". Observations were made in ArII 611 light. TQ started at 2.0 ms. Cyan points outline position of the inner wall. Green points mark position of the $q = 2$ flux surface in the plane parallel to the lens.

### 4.1.1 Reconstruction of camera images

In this section the emission front is confirmed to be at $q = 2$ at the onset of the thermal quench. A detectable intensity registered in the center of the discharge appears because of the toroidal geometry. To draw these conclusions camera images are reconstructed for a model distribution of the injected gas. The simplest configuration of the emissivity to be examined is that with light emitted from the region that is uniform poloidally and toroidally but is $\delta$-like in the radial direction.

The task of finding intensities in the image plane is strongly simplified by noting that the light emitted by a certain volume element in the physical space is collected exclusively by one pixel in the image plane. This rule is violated only for the volume elements located at the boundary between two pixels. The latter is obviously negligible if the chosen volume size is sufficiently small. The statement follows from two facts: (i) the depth of field of the optical system is larger than the extensions of the torus and (ii) the diffractive blurring does not introduce any complications.

The depth of field is defined as a distance from the plane of focusing to the plane in which points are imaged with the blur circle equal to some characteristic size of the image. The

characteristic size of the image is obviously the pixel size. With typical parameters of the optical system the depth of field $\delta Z$ is estimated to be [128]:

$$\delta Z = \frac{Z^2}{fd} r_{pix} \approx 4 \text{ m} \gg L \sim R_0 = 1.75 \text{ m}, \tag{4.1}$$

where the distance from the lens to the plane of focusing $Z$ is about 2 m, the most unfavorable $f/d \sim 4$ is assumed and the maximal distance from the plane of focusing $L$ is of the order of the major radius $R_0$. Equation 4.1 states that the optical system images the whole physical space in focus, i.e. without blurring. The statement is confirmed experimentally: the whole tokamak wall is reproduced sharply.
Because of the large pixel size the diffraction does not introduce any significant blurring either:

$$f\frac{\lambda}{d} \sim 30\ \mu m \ll 200\ \mu m, \tag{4.2}$$

where again the most unfavorable $f/d \sim 30$ was taken.
If that is the case, for an optically thin plasma the problem is reduced to estimating the integral:

$$I \sim \int_V \Omega d^3V \sim \int_V \frac{\cos\alpha}{D^2}\delta(r - r_0)\cos\phi(R_0 - r\cdot\cos\theta) r dr d\phi d\theta = \int_V \frac{\cos\alpha}{D^2}\cos\phi(R_0 - r_0\cdot\cos\theta) d\phi d\theta, \tag{4.3}$$

where the light is emitted from the region that is $\delta$-like in the radial direction, the region $V$ is the volume imaged to the chosen pixel $(x,y)$, $\Omega$ is the solid angle based on the lens diameter and $\alpha$ is the angle of incidence (fig. 4.4). For the sake of convenience the integral was transformed to toroidal coordinate system $r,\theta,\phi$. Since only the relative distribution is of importance, the plasma emissivity and the lens diameter were omitted.

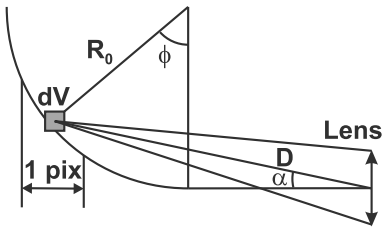


Figure 4.4: Illustration of geometry.

The results of estimating integral 4.3 are compared with the experimental measurements for two discharges in figure 4.5. At the top the 2D images are shown (subfigures 1, 2, 5, 6). Plotted below are the two horizontal and two vertical 1D scans taken at the positions marked by arrows at the 2D frames. Note that the chip dark current was subtracted from the experimental data. Both the experimental and simulated 1D profiles were normalized to the value at the same position, which however can be different from figure to figure.
While the subtle details, like the relative intensities of pixels at the poloidally opposite points, differ between the experiment and simulation, the qualitative distribution of intensity is predicted rather well. The experimental positions of the intensity peaks, their decay towards the plasma center and an appreciable intensity in the center of the discharge are reproduced. The relative intensities disagree because of the ploidal/toroidal asymmetry of the emissivity and not a $\delta$-like radial profile. The last fact is especially pronounced in subfigures 4 and 8, where the experimental peaks are broader and transition between their subpeaks is very smooth.
The conclusion holds for all experimental data obtained in HeI, HeII, ArII and CIII lines. The only exceptions are the observations of deuterium injections in $D_\alpha$ light (discharges 100169, 100939 and 101144) and the observations of argon injections in ArI light (discharges 100932 and 100933). The ArI emission in the discharges terminated by argon puff is highly localized to the injection port. The strong noise similar to that seen in figure 4.2-2 precludes more detailed studies. In the case of the observations of massive deuterium puffs in $D_\alpha$ light (including argon mixtures) the emission front is registered close to or a few centimeters away from the $q = 2$ flux surface but the front is very wide, fig. 4.6. If the $D_\alpha$ observations are made in the discharges terminated by pure helium or argon, the results do obey the general rule.

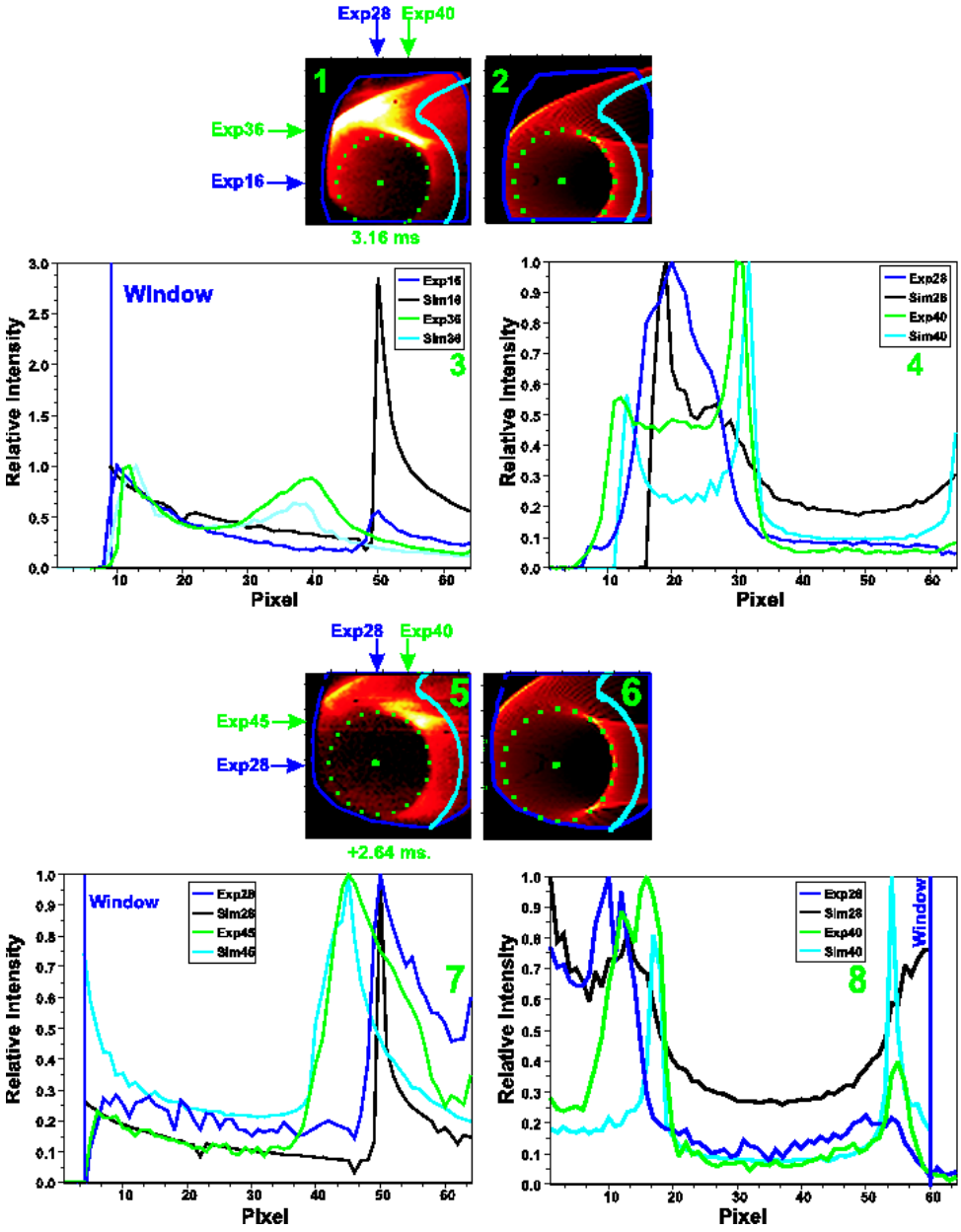


Figure 4.5: Comparison of the simulated images with the experimental result. 1 - 4: TEXTOR shot 99688, injection of 1.5 bar of He "x1". Observations were made in HeII light. 1- experimental observations. Cyan points outline position of the inner wall. Green points mark position of the $q = 2$ flux surface in the plane parallel to the lens. Arrows indicate positions of the scans shown in figures 3, 4; 2 - the intensity distribution simulated for $\delta$-like emissivity at $q = 2$. 3 - horizontal scans. 4 - vertical scans. 5 - 8 the same as 1-4 but for TEXTOR shot 101152, injection of 1.5 bar of Ar5%+$D_2$95% "x1". Observations were made in CIII light.

Despite omitting such effects as a realistic $(r,\theta,\phi)$–distribution of the gas, a possible plasma thickness and imperfections of the optical system (vignetting, etc.) the proposed simple model (eq. 4.3) does confirm that the emission front at the onset of TQ is localized at the $q = 2$ flux surface. Being based on the qualitative behaviour of profiles and similarity of the images this conclusion does not depend on the system sensitivity at all. The exact position

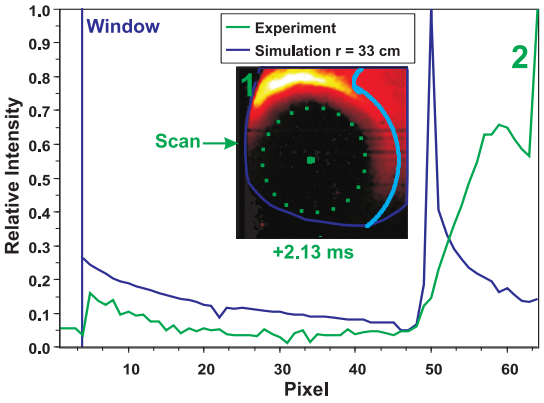


Figure 4.6: Comparison of the simulated image with the experimental result. TEXTOR shot 101144, injection of 4.5 bar of Ar5%+$D_2$95% "x1". Observations were made in $D_\alpha$ light. 1- 2D frame. Cyan points outline position of the inner wall. Green points mark position of the $q = 2$ flux surface in the plane parallel to the lens. Arrow indicates position of the scan shown in figure 2; 2 - horizontal scans.

of the emission front can be found at the high field side, where the toroidal "smearing" is negligible.

### 4.1.2 Fraction of injected gas

The fraction of the gas injected prior to the thermal quench is an important parameter. Only the particles introduced before the disruption are available for the mitigation of the heat loads and can be mixed into the plasma core. And consequently only these particles will participate in suppressing runaway electrons. In addition, this fraction helps to analyze the energy balance in the predisruptive phase (see the following section).
The fraction of the gas injected in time $\tau = t_{TQ} - t_G$ is given by:

$$f_{inj}(t_{TQ}) = 1 - \exp(-\alpha \cdot (t_{TQ} - t_G)), \tag{4.4}$$

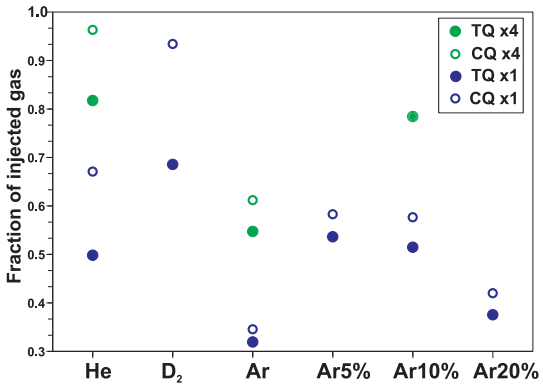


Figure 4.7: Fraction of the gas injected before thermal/current quench. "x1" - configuration of the valve with small orifice; "x4" - valve with the enlarged diameter of the output orifice; solid symbols represent fraction of the gas injected before the TQ; opened symbols - the same up to the CQ.

where the decay rate $\alpha$ is taken from table 3.2, $t_{TQ}$ is the start of the thermal quench and $t_G$ is the start of the predisruptive phase. These data are plotted in figure 4.7 for all used gasses. Note that the dependence of these results on the working pressure is very weak. With the valve configuration having small output orifice ("x1") more than half of the gas is injected in all cases with the exception of argon and mixture of 20% of Ar. A large concentration of argon reduces the fraction of the injected gas almost to 30%. The valve with the increased orifice ("x4") makes it possible to introduce more than half of the reservoir in the case of slow argon and more than 80% for the other used gases (He and mixture Ar 10% + $D_2$ 90%.). In the same figure one finds the fraction of particles delivered before the beginning of the current quench.

### 4.1.3 Interpretation of the emission front

In many cases the emission front in the predisruptive phase can be thought to be equivalent to the penetration of injected atoms. To prove this it is worth comparing the thermal energy lost by the plasma before the thermal quench with the energy consumed by the injected atoms.
The energy lost by the plasma consists of the two parts: the energy stored initially outside of the $q = 2$ flux surface and the energy lost by the plasma core due to the (possible) density decrease. The sum of this two parts $E_{Plasma}$ does not exceed 10 kJ.
If the conduction across the "cold gas mantle" is negligible, the energy $E_{Loss}$ consumed by the injected atoms includes the single ionization with the ionization energy $I_1$, the second-order ionization of some fraction $f_{sec}$ with the ionization potential $I_2$, heating $3T_e/2$ and radiative losses $E_{Rad}$:

$$E_{Loss} = N_{atoms} \cdot f_{inj}(\tau) \cdot (I_1 + 3T_e + I_2 \cdot f_{sec} + \frac{3}{2} T_e \cdot f_{sec}) + E_{Rad} \tag{4.5}$$

where $N_{atoms}$ is the total number of atoms stored in the valve working chamber, $f_{inj}(\tau)$ is the fraction of atoms injected before the thermal quench and $\tau = t_{TQ} - t_G$. The consideration is limited to the second-order ionization since for the mixtures containing argon, which is the only used element that can be ionized more than two times, this turns out to be more than sufficient. The radiative losses are found in the coronal approximation, with the dynamics of the electron density taken into account:

$$n_e = n_{atoms} \cdot (1 + f_{sec}) = \frac{(1 + f_{sec})}{V} \cdot \int_0^t F \exp(-\alpha\xi)\, d\xi = \frac{(1 + f_{sec})}{V} \cdot \frac{F}{\alpha}(1 - \exp(-\alpha t)) \tag{4.6}$$

$$E_{Rad} = VL_{rad}(T_e) \int_0^\tau n_e \cdot n_{atoms}\, dt = \frac{L_{rad}(T_e)(1 + f_{sec})}{V} \left(\frac{\mathrm{F}}{\alpha}\right)^2 \int_0^\tau (1 - \exp(-\alpha t))^2\, dt =$$
$$= \frac{L_{rad}(T_e)(1 + f_{sec})}{V} \left(\frac{\mathrm{F}}{\alpha}\right)^2 \left(\tau - \frac{2}{\alpha} f_{inj}(\tau) + \frac{1}{2\alpha} f_{inj}(2\tau)\right), \tag{4.7}$$

where the volume of the emitting region is assumed to coincide with the plasma volume outside of the $q = 2$ flux surface $V \sim 4$ m$^3$ , the radiative cooling rates $L_{rad}$ for argon and helium can be found in [130, 131] and [132] correspondingly, the peak flow rates F are compiled in table 3.1, the decay rate $\alpha$ is given in table 3.2 and $f_{inj}(\xi) \equiv 1 - \exp(-\alpha\xi)$. $T_e$ was taken to be 3 eV for all gases. This temperature is far from the maximum of the radiative cooling rates, which lyes at about 20 eV for argon and 7 eV for helium.
Argon possessing a high radiative cooling rate, even the smallest used amount of mixtures containing argon $p_w = 1.5$ bar would consume more than the total energy content of the discharge even if the particles were only singly ionized. Thus, not all injected particles can be kept ionized and the emission should arise from the region of interaction between the injected gas and the hot plasma. The emission front coincides with the penetration of

atoms.
For helium and deuterium the situation is very similar to the argon one even despite a three orders of magnitude lower radiative cooling rate. Figure 4.8 presents a comparison of the energy consumed by the injected atoms at different working pressures for helium and deuterium. For the helium case the energy is plotted for single and the second-order ionization. Already for puffs of 2 bar of He or $D_2$ the single ionization is enough to consume the energy lost by the discharge before the thermal quench. Consequently for the most helium experiments the emission front of singly ionized ions can be identified as the position of injected atoms. But the interpretation of the $D_\alpha$ observations of the deuterium puffs is more complicated as it has already been pointed out in discussing figure 4.6.
The speculations are of course qualitative since many factors are not taken into account.

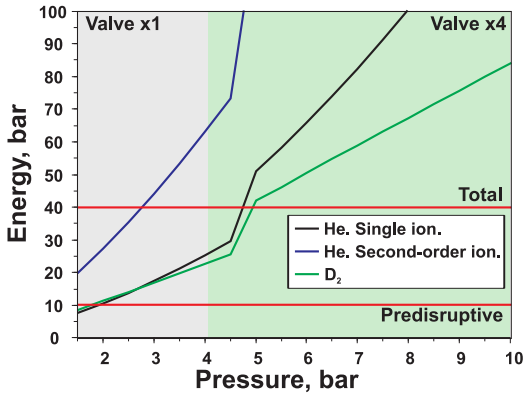


Figure 4.8: Comparison of the energy lost in the predisruptive phase with the available energy. The energy lost by the discharge before the disruption is marked by the red line "Predisruptive". The full plasma thermal energy is indicated by red line "Total".

As important effects one can specify the following: some fraction of the delivered particles stays outside of the plasma; the volume $V$ is certainly overestimated; the assumption of the coronal approximations can be violated for the localized energy sink; the temperature dynamics is unknown. More involved considerations are left for a future work.
The observations performed in $D_\alpha$ light in the discharges terminated by He or Ar puffs obviously show the position of the cold region, the same is true for the CIII line in all experiments.

### 4.1.4 Duration of the predisruptive phase

In the previous sections it was shown that the TQ develops as soon as the $q = 2$ flux surface is cooled and the gas emission is detected in its vicinity. Here the coincidence of these two events with the start of TQ is summarized and the duration of predisruptive phase is determined.
The delay between the start of TQ and the cooling of the $q = 2$ flux surface or the arrival of gas to this surface is presented in figure 4.9-1. Where cooling of the $q = 2$ flux surface is understood as a drop of $T_e$ at $r = 31$ cm by 20% ("squares"). With the exception of low pressure ($p_w < 5$ bar) helium or deuterium injections likely possessing deficient cooling capability the delay between the drop of electron temperature at $q = 2$ and in the center spans from 0.1 up to 0.4 ms. On average this time is about 0.3 ms. Approximately the same delay is typical for the phase lasting from the detection of the emission front at $q = 2$ until disruption, but its mean value approaches 0.2 ms. It is also worth noting here that the difference in time between the arrival of emission front and the detection of cold front constitutes only about 0.1 ms. Summing up, cooling of the $q = 2$ flux surface by the direct contact with injected gas coincides with the accuracy of about $0.2 - 0.3$ ms with the start of

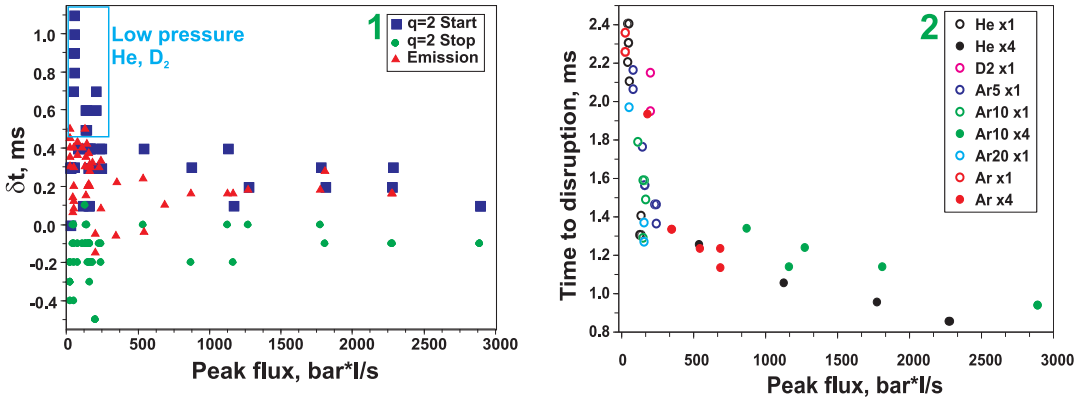


Figure 4.9: Duration of the predisruptive stage. 1 - difference between the start TQ and time moments of several important events. "Squares" - drop of $T_e$ at $q = 2$ by 20%. "Circles" - drop of $T_e$ at $q = 2$ down to 20% of its initial value. "Triangles" - arrival of the emission front to $q = 2$. 2 - duration of the predisruptive phase. Open symbols are for old valve configuration ("x1"), solid ones for "x4" valve. Note that with exception of one point all data "Ar x4" were determined from measurements of the limiter potential.

TQ.

The average velocity of the gas motion in the predisruptive phase is equal to 170 $m \cdot s^{-1}$, which is much lower than even the argon sound speed at room temperature. That is the neutral gas does not stream freely, but the propagation mechanism seems to be more complicated.

Complete cooling of the region around $q = 2$ always takes place together with or only after the start of the disruption. In some cases this fact can be explained by a strong heat outflux from the core, see for example positive spike at the ECE channel located at $q = 2$ in figure 4.11.

Full duration of the predisruptive phase in dependence on the peak particle influx rate is given in figure 4.9-2. In this dependence one can distinguish two different regions. In the first one, the duration of predisruptive phase is determined by the rate of particles influx. Consequently in the first region the time for the gas to destabilize the plasma drops considerably as the influx rate is increased. In the second region the duration is seen to be almost independent on the influx rate. To put it in another way, it is not the rate of particles delivery but rather the dynamics of their propagation through the plasma that is important. In both situations the influence of gas type is weak.

One has to mention that the definition of thermal quench used here is not completely self-consistent. The discussed start of TQ describes cooling of the single ECE channel at $r = 1$ cm, i.e. the very last step of disruption. However the introduced uncertainty about 0.3 ms is not critical for the current purposes, the corrected definition based on the loss of the energy will be used below in discussing duration of the TQ.

## 4.2 Thermal quench

In the thermal quench the energy stored in the plasma core is lost on a short timescale. In the previous section it was shown that the thermal quench is initiated as soon as the $q = 2$ flux surface is cooled. The onset of TQ was determined with ECE diagnostics. The ECE being prone to the cut-off (section C), the start of TQ is confirmed here by the analysis of additional diagnostics. The question of reliability of ECE measurements is especially relevant in the case of helium injections revealing a 2 ms long delay between the TQ and the start of current decay. Afterwards the duration of TQ is determined from the measurements of soft X-ray emission.

### 4.2.1 Start of the thermal quench

To clarify the point the following diagnostics were used: X-ray bursts registered by the fast camera, measurements of the limiter blade potential, fluctuations of the poloidal magnetic field measured by Mirnov coils at the plasma circumference. These diagnostics show distinct bursts or oscillations at the onset of the TQ.

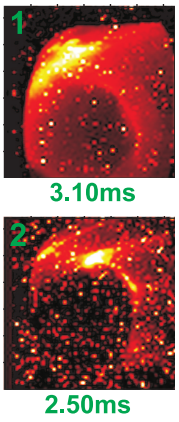


Figure 4.10: X-ray burst at the beginning of TQ. 1 - TEXTOR shot 99681, injection of 1.7 bar of He "x1". Observations were made in $D_\alpha$ light. TQ started at 3.2 ms. 2 - TEXTOR shot 100167, injection of 2.5 bar of Ar10%+$D_2$90% "x1". Observations were made in ArII 442 light. TQ started at 2.6 ms.

The direct contact of the cold gas with the $q = 2$ flux surface is usually, but not always, followed by a $0.1 - 0.3$ ms long burst of X-ray radiation. This burst is pronounced as a snow like noise at the camera data (fig. 4.10) or as an intensity increase at the SXR camera (section 4.2.2). The strength and duration of this burst are rather arbitrary and do not depend on the type and amount of the gas used. The burst is absent in about 30% of the shots, which can be simply due to a different toroidal location of the source. It is to be pointed out that the pure argon experiments are omitted from the analysis being presented here, because one can not distinguish the X-ray burst from the "background" noise caused by the losses of runaway electrons during the current quench. In the last case X-ray photons are captured in the storage area (section 3.2). Since the burst is also registered in the case of pure deuterium injections it is not likely to be purely K-line emission but it should at least partially arise as result of increased Bremsstrahlung radiation. It is also possible that the reason for the burst is the loss to the wall of a small population of runaway electrons existing before the gas puff. At the moment it is not possible to draw a final conclusion about the nature of this phenomenon. However there is a clear correlation of this event with the onset of TQ.

Figure 4.11 illustrates the correlation of the other two signals mentioned above with the start of TQ. Shown are the following two discharges: the low pressure helium injection (subfigures 1 - 4) and the pure argon puff (subfigures 5 - 8). In both cases at the start of TQ (drop of the central $T_e$ by 20%) oscillations of the poloidal field measured by Mirnov coils are observed (subfigures 2, 6). Simultaneously the potential of the limiter experiences a negative spike indicating contact of hot plasma to the wall (subfigures 3, 7). The toroidal limiter consists of 8 separate blades, the signal shown in the figure is the average over all of them. In helium experiments these 1 ms peaks are followed by a "silent" phase of approximately 1.5 ms, while for all other gases even larger fluctuations of $dB_p/dt$ and of the limiter potential appear immediately after the TQ. For helium, due to a probable

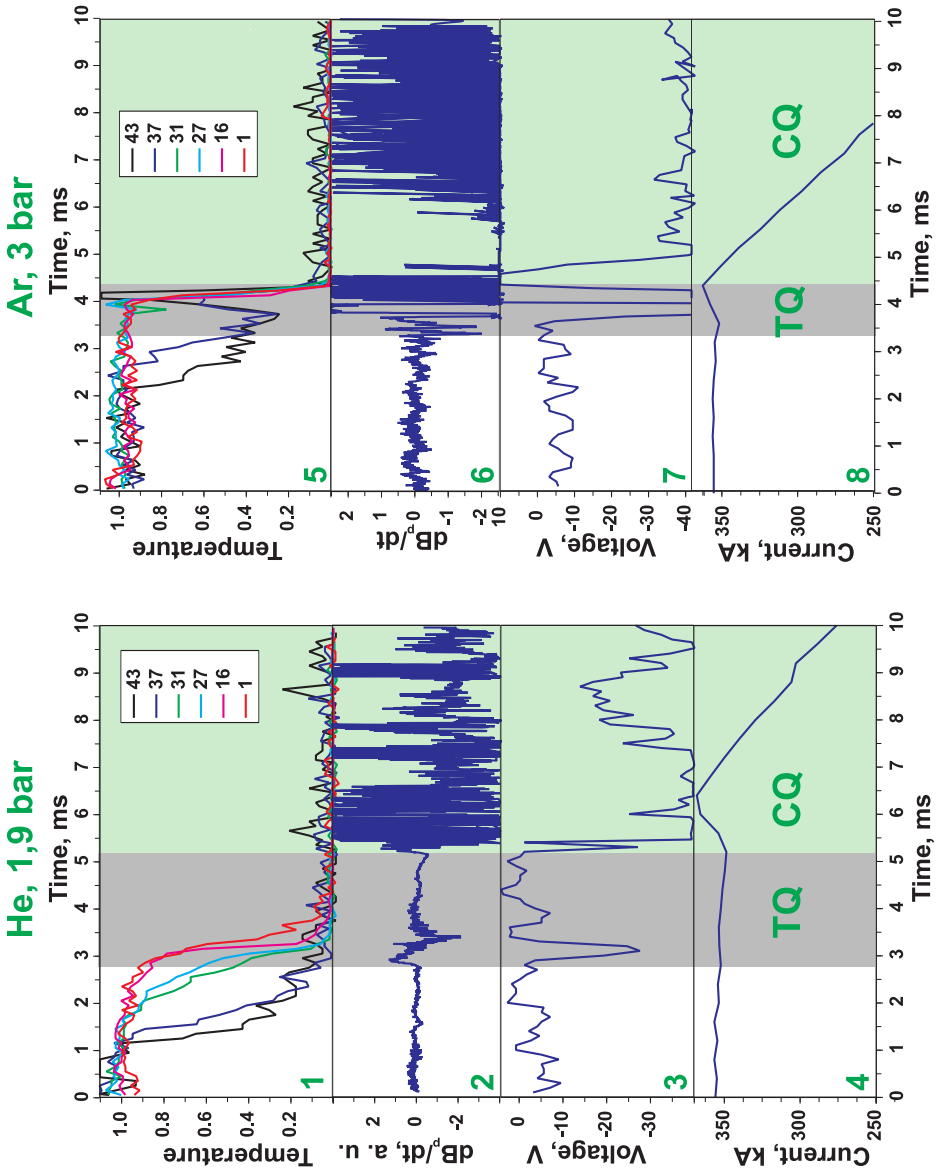


Figure 4.11: Start of the thermal quench. 1 - 4 - TEXTOR shot 99688, injection of 1.9 bar of He "x1". 1 - normalized temperature as measured by ECE system; 2 - $dB_p/dt$ measured by Mirnov coil (TEXTOR signal "star/ti050"); 3 - potential of the limiter averaged over all 8 blades; 4 - plasma current; 5 - 8 the same as 1-4 but for the TEXTOR shot 100165, injection of 3 bar of Ar "x1".

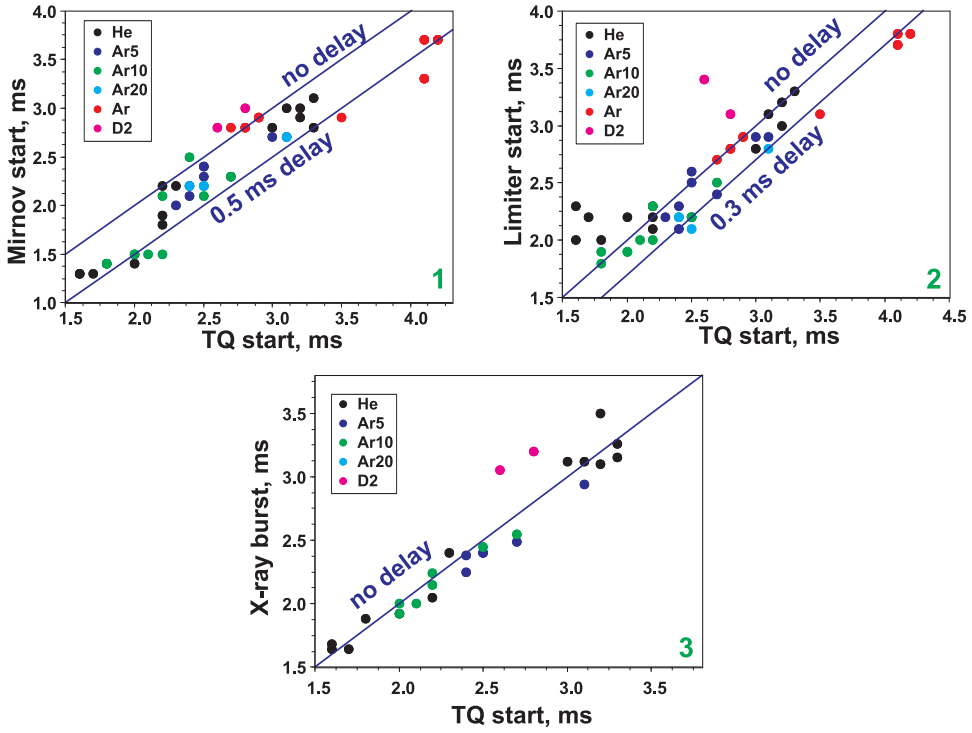


Figure 4.12: Correlations of the auxiliary signals with the start of thermal quench. 1 - fluctuations of magnetic poloidal field measured by Mirnov coil; 2 - variation of the limiter potential; 3 - X-ray burst registered by the fast camera.

ECE cut-off, the temperature dynamics during the "silent" phase can not be traced, but the start of thermal quench seems to be determined correctly as seen from the coincidence of oscillations and of X-ray burst with the drop of central temperature. One has to note that the toroidal and poloidal arrays of Mirnov coils are usually used to determine the mode structure of instabilities, but because of a very short duration of the MHD activity such analysis was impossible in the experiments on massive gas injection.
The correlations demonstrated above for selected shots are summarized for all experiments in figure 4.12. In figure 4.12-1 the start of $dB_p/dt$ oscillations is plotted versus the start of TQ. In the second subfigure the same dependence but for the first distinct change of the limiter potential is presented, and the last one illustrates the X-ray burst.
The linear correspondence is observed for all presented data, however the related accuracy is different from figure to figure. The highest uncertainty of about 0.5 ms is associated with Mirnov signal, while the lowest error bars are typical for X-ray burst. The found regularities provide confidence in determining the start of thermal quench, even more these auxiliary signals can be used to specify the onset of the disruption with associated accuracy of about 0.2 ms if the ECE measurements are not available, as it is the case for high pressure argon injections (TEXTOR discharges 102521 - 102528).

### 4.2.2 Duration of thermal quench

The duration of thermal quench is determined from the soft X-ray (SXR) emission. For the description of the SXR diagnostics see section 3.3.3.

Time traces from several channels of the SXR camera are given in figure 4.13-2. Raw signals represented by "blue" lines have well pronounced pick-up noise. Since all of them demonstrate almost the same pick-up disturbances, the usual technique of noise reduc-

tion is to subtract the most outward channel. But in the DM experiments the outermost channel shows a non-zero signal in thermal quench phase. For this reason the data were smoothed by a moving average procedure over 8 neighboring points ("green" lines).
Since the SXR emission arises mainly in the region inside of $q = 2$, before the direct contact of the gas with the $q = 2$ flux surface the intensity is not affected. Soon after the detection of gas emission around $q = 2$ ("black" vertical line) a strong increase of the SXR signal is observed on all chords. The surplus intensity is likely to be of the same nature as the X-ray burst registered by the fast camera (section 4.2.1) and consists of the thermal part due to increased density and effective charge and of the K-line emission in the case of argon presence. The appreciable thermal contribution is confirmed by the presence of this burst in helium and deuterium experiments. It is to be noted that the structure and the amplitude of the peak considerably vary from shot to shot probably due to the phase of the triggered instability. The simultaneous increase of intensity on all chords may indicate that the emitting region is located close to the boundary. After the peak the SXR signal drops due to cooling of the plasma.
Very strong pick-up is always registered at the moment of the transitive current peak ("yellow" area). In the following current quench phase highlighted by "light green" area a considerable intensity is still registered on all channels. Because of very low temperatures ($T_e \sim 10$ eV) typical for the CQ phase the origin of this signal should be related not to thermal Bremsstrahlung but to the voltage induced by the decaying current.
In figure 4.14 contour plots of the smoothed signals are shown for shots terminated by injection of different gases. These plots are composed of data from both available cameras which are joined along the "cyan" line drawn in the third subfigure. To combine both cameras all channels were normalized to the intensity of the two closest central channels ($r = 0.024$ cm for camera 3 and $r = 0.028$ cm for camera 4) measured in the stable phase of the discharge. Most important events are marked by vertical arrows: "black" arrow - moment when the gas emission front reached $q = 2$; "green" - temperature drop at $q = 2$ cm by 20%; "red" arrow - drop of the central temperature. All these moments usually coincide with the accuracy of 100 $\mu$s with the peak of the SXR intensity. The only exceptions are observed for cooling of $q = 2$ cm in low pressure helium and deuterium puffs, which is illustrated by figure 4.14-1. In these cases the temperature at $q = 2$ drops before

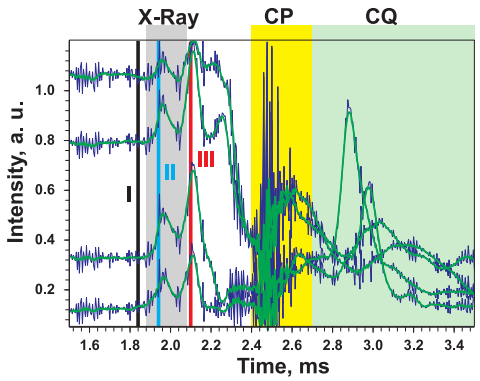


Figure 4.13: Traces of several SXR channels during DM experiment. TEXTOR shot 102510, injection of 7 bar of Ar10%+$D_2$90% "x4". "Blue" lines - raw signals; "green" lines - signal smoothed over 8 neighboring points; "black" vertical line (I) - moment when the emission front reached the $q = 2$ surface; "cyan" vertical line (II) - drop of temperature at $q = 2$ cm by 20%; "red" vertical line (III) - drop of the central temperature; "gray" rectangle (X-Ray) - X-ray burst at the fast camera images; "yellow" rectangle (CP) - the current peak; "light green" rectangle (CQ) - current quench.

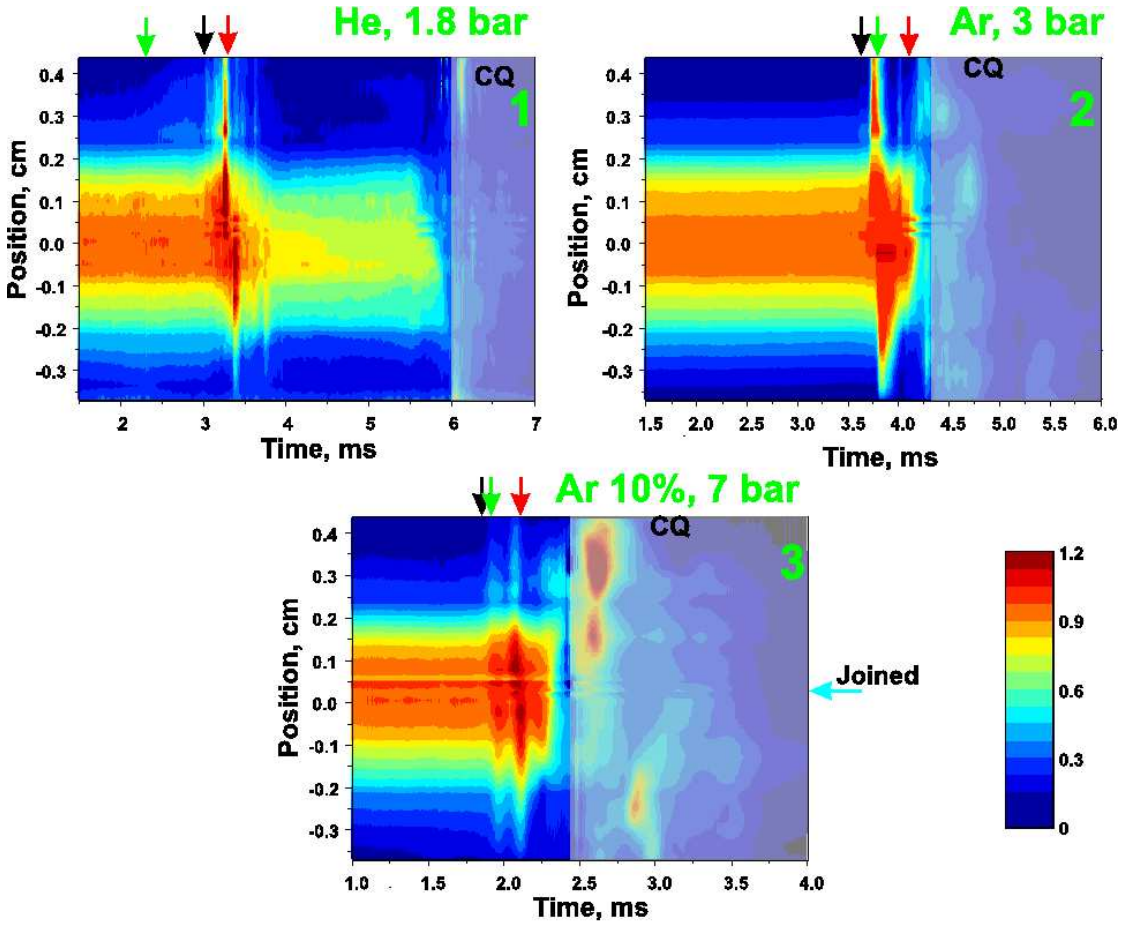


Figure 4.14: Contour plots of SXR intensity for several TEXTOR discharges. 1 - TEXTOR shot 100929, injection of 1.8 bar of He "x1". 2 - TEXTOR shot 100166, injection of 3 bar of Ar "x1". 3 - TEXTOR shot 102510, injection of 7 bar of Ar10%+$D_2$90% "x4". "Black" arrow - the moment when the emission front reached $q = 2$; "green" arrow - drop of temperature at $q = 2$ cm by 20%; "red" arrow - drop of the central temperature; "cyan" horizontal arrow - the line along which the data from two cameras are combined.

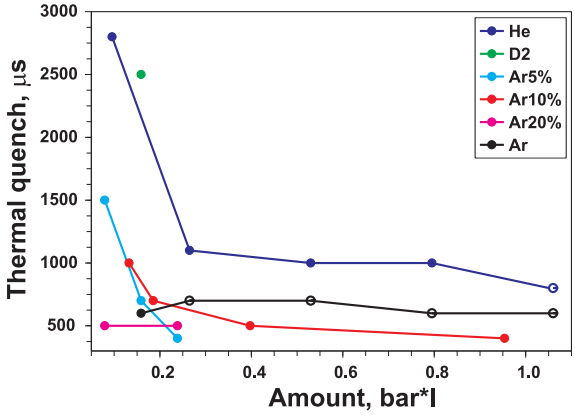


Figure 4.15: Duration of the thermal quench.

the arrival of gas, see also figure 4.9 - 1. The probable reason of such behaviour is cut-off of the ECE channel. The thermal quench in such cases turns out to be also more complicated than usually and to consist of several stages: first the region outside of $r \approx 0.2$ m is cooled down, which is followed by a "silent" phase lasting about 2 ms (in shown case) until the final collapse takes place (compare with the "silent" phase in figure 99683vs100165traces). The current quench phase highlighted by the shaded area does not reveal any significant features unless runaway electrons are present.
By definition thermal or equivalently the energy quench is the phase in which the bulk of the stored energy is lost. Taking this into account one can determine the duration of TQ from the discussion above as the period lasting from the peaking of SXR intensity until the detection of the current peak. The duration of thermal quench calculated in such a way is plotted with solid symbols in figure 4.15. Since not in all shots SXR measurements are available, the data are completed by the difference between the moment of the current peak and the cooling of the $q = 2$ flux surface found either from the ECE signal or from the burst of the limiter potential if ECE is also not available (opened symbols).
The behaviour of TQ duration with increase of the amount of injected gas is different for the gasses possessing a good cooling capability (pure argon, 20% mixture of argon) and for gasses with low cooling rates. For the first group (pure argon, 20% mixture of argon) the TQ duration does not depend on the amount of gas in the whole explored range 0.07 – 1.1 bar·l, while for the second group a lower cooling capability results in the growth of the duration at small amounts of injected particles $\lesssim 0.2$ bar·l. In any case, for the amounts of particles that are larger than $\sim 0.2$ bar·l the TQ duration does not depend on the number of particles and constitutes about 500 $\mu$s for argon and argon mixtures and about 1 ms for helium.
It is worth stressing that the drop of temperature of the central ECE channel, which is often used in the literature to define TQ, proceeds much faster than the duration of TQ given here would suggest, see for example figure 4.11. The maximum of energy density $\sim p \cdot r$ is at the radii between 15 and 20 cm, and the energy stored in the very center is relatively low because of the small volume. For this reason the central temperature alone can fall much faster.

### 4.2.3 Fast camera observations

At the moment of the discussed X-ray burst the whole picture registered by the fast camera starts to change. Details of this process are complex and can include deformation of the initially circular emission front, appearance of separated regions etc. For example, a bent

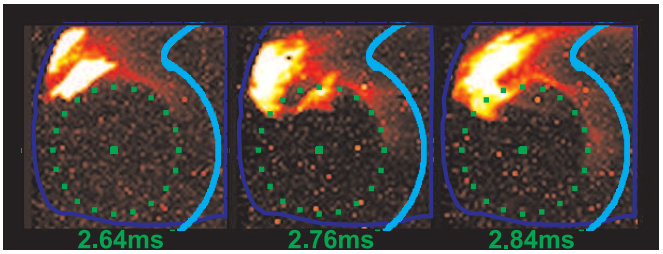


Figure 4.16: Bent structure during the thermal quench. TEXTOR shot 102526, injection of 20 bar of Ar "x4". Observations were made in ArII 611 light. Cyan points outline position of the inner wall. Green points mark position of the $q = 2$ flux surface in the plane parallel to the lens.

like structure in the toroidal direction is observed in massive puffs of 15 and 20 bar of argon fig. 4.16, note that this phenomenon is not seen in the experiments with other gases or with lower pressures of argon. Finally the first changes are followed by the backward motion of the emission front to the wall, which is likely caused by the strong heat outflux from the center of the discharge, fig. 4.17. The front reaches the wall after about 0.4 – 1 ms depending on the particular conditions, the touch moment coinciding with the onset of the current quench.

In low pressure helium and deuterium injections the two stage structure of TQ discovered in SXR data is also pronounced at the fast camera images, fig. 4.18. First the emission front expands as usually and approaches the wall in the period $t = 3.22 - 3.92$ ms. Then the "silent" phase with complicated stripe like pattern is seen at $t = 4.30$ ms, which is followed by a partial restoration of circular like shape $t = 5.30,\ 5.90$ ms. And finally the second wall contact to be attributed to the last step of the thermal quench takes place at $t = 6.40$, discharge turns into current quench. A more precise structure of the "silent" phase is difficult to identify because of the increased overall intensity.

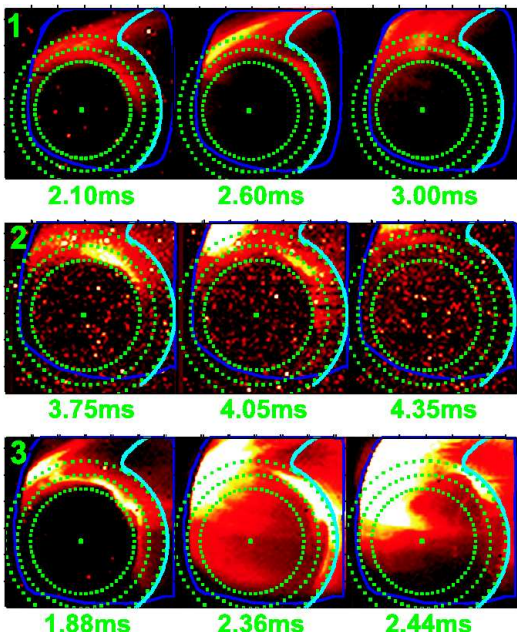


Figure 4.17: Behaviour of the emission during thermal quench. 1 - TEXTOR shot 100168, injection of 4.5 bar of He "x1". Observations were made in HeII light. TQ started at 2.2 ms. 2 - TEXTOR shot 100934, injection of 3 bar of Ar "x1". Observations were made in ArII 611 light. TQ started at 4.1 ms. 3 - TEXTOR shot 102520, injection of 6.4 bar of Ar10%+$D_2$90% "x4". Observations were made in ArII 611 light. TQ started at 2.0 ms. Cyan points outline position of the inner wall. Green points mark position of the flux surfaces $r = 30, 38, 46$ cm in the plane parallel to the lens.

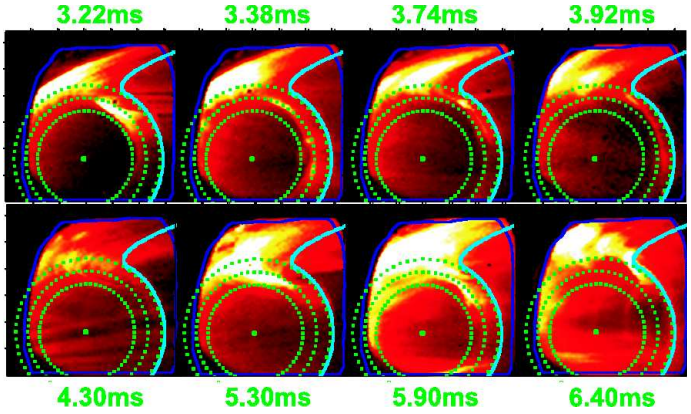


Figure 4.18: Behaviour of the emission during thermal quench for low pressure helium injection. TEXTOR shot 99688, injection of 1.5 bar of He "x1". Observations were made in HeII light. TQ started at 3.3 ms. Current quench started at 6.1 ms. Cyan points outline position of the inner wall. Green points mark position of the flux surfaces $r = 30, 38, 46$ cm in the plane parallel to the lens.

### 4.2.4 Summary

Direct contact of the cold gas with the critical $q = 2$ flux surface results in distinct MHD activity, negative spike of the limiter potential and burst of the X-ray emission registered by both the fast camera and the SXR camera. The direct contact was consistently inferred from the measurements of electron temperature by Thomson scattering and ECE and from the fast visible imaging. Afterwards the whole central region is cooled down without clear cold front propagation on the SXR or fast camera. On contrary, the fast camera shows a backward motion of the emission front to the wall, which is likely to be related to the heat outflux from the core plasma. It is the absence of the gradual cooling and almost simultaneous collapse of the rest of the plasma that allows us to name this phase thermal quench. The disruptive nature of the shutdown is also confirmed by a transient peak of the current just before the current quench.

The duration of the thermal quench turns out to be independent on the number of particles if this number is larger than 0.2 bar·l. In such case argon containing mixtures (including pure argon) cool the core plasma in about 0.5 ms, while in the helium experiments the thermal quench lasts about 1 ms. For smaller amounts of injected atoms < 0.2 bar·l the cooling capability of helium, deuterium and mixtures containing less than 20% of argon is insufficient, which results in the duration of the TQ being dependent on the amount of puffed gas. It is to be mentioned that in the experiments with small amounts of helium or deuterium the thermal quench is characterized by a two step process: first the plasma outside of $r \approx 0.2$ cm is cooled, then the "silent" phase with preserved core inside that radius lasts about 1 – 2 ms until the final crash occurs.

The reason for the onset of disruption after cooling of $q = 2$ is most likely to be the destabilization of the kink/tearing mode by a steep current gradient. Indeed, the intensity of the observed spectral lines is significant at such low temperatures $T_e \lesssim 10$ eV as to provide significant time for the current to diffuse into the core (it was observed experimentally that the current dissipated before the current quench is of the order of 1% of the initial plasma current):

$$\tau \sim \frac{4\pi\sigma\delta r^2}{c^2} \sim 0.7 \text{ ms} \lesssim t_{TQ} - t_G \sim 1 \div 1.5 \text{ ms}, \tag{4.8}$$

where conductivity $\sigma$ is taken to be Spitzer one and $\delta r$ is of the order of 10 cm. Thus, the cooling of the outer regions leads to a critical current gradient around $q = 2$. The found sequence of events is similar to the edge deficiency type of disruptions according to Schüller classification (section 2.1).

The DIII-D experiments also showed a clear dependence of duration of the predisruptive phase on the position of $q = 2$ [98]. It is to be noted that in DIII-D experiments the position of $q = 2$ was defined for the equilibrium current profile. In the current work, in addition, it was shown that gas before thermal quench stays outside of the $q = 2$ flux surface. This is unfavorable from the point of view of runaway electrons generation in the following current quench. This conclusion was drawn from the measurements of the electron density with Thomson scattering and from the fast camera observations. To specify the density of impurities delivered to the center a transport in the TQ has to be considered.

## 4.3 Current quench

At the end of the thermal quench the plasma is too cold and too dirty to sustain current. Consequently the current starts to decay on a resistive time scale:

$$\frac{dI}{dt} = I \cdot \frac{L}{R} \tag{4.9}$$

Where the resistance is based on Spitzer resistivity [133]:

$$R = \frac{2\pi R_0}{\pi a^2} \cdot \eta_{Spitzer} \sim \frac{\langle Z^2 \rangle}{T_e^{3/2}} \tag{4.10}$$

Introduction of impurities accelerates the current decay by changing both effective charge and electron temperature. It is to remembered that fast current quenches are thought to be preferable for minimization of halo currents (section 2.4.2). In natural disruptions impurities are carbon and oxygen released from the wall [26, 20], with their amount being uncontrolled leading to big scatter in the experimental data and making reliable control of the current quench phase impossible. In mitigated disruptions the impurities are supplied by the gas puff determining in such a way both temperature and the effective charge.
One also has to mention that the energy associated with the plasma current is higher than the initially stored thermal energy. But since the magnetic energy is mainly removed by uniform radiation on a slower time scale this dissipation is expected to be acceptable, e.g. for the used TEXTOR discharge the thermal loads are not critical at all:

$$P = \frac{E_{mag}}{S\tau_{CQ}} \sim \frac{3 \cdot 10^5 [\mathrm{J}]}{30[\mathrm{m}^2] \cdot 3 \cdot 10^{-3}[\mathrm{s}]} \approx 3 \quad \frac{\mathrm{MW}}{\mathrm{m}^2} \tag{4.11}$$

$$\phi_d = P \cdot \sqrt{\tau} \approx 0.2 \ \mathrm{MJ \cdot m^{-2} \cdot s^{-1/2}} \ll \phi_{cr} \approx 25 \ \mathrm{MJ \cdot m^{-2} \cdot s^{-1/2}}, \tag{4.12}$$

where damage parameter $\phi_d$ and its critical value $\phi_{cr}$ have been discussed in section 2.4.1.

### 4.3.1 Current decay rate

The plasma current is measured by a Rogowski coil. Due to technical problems reliable measurements are available only for TEXTOR discharges 102509 – 103003. The Rogowskii coil provides the current derivative and numerical integration was used to reconstruct the current itself. Examples of both signals for different types of introduced gases are given in figure 4.19. The fastest current quench is registered in the case of argon injection, while the slowest one is typical for helium experiments.
All such observations are summarized in figure 4.20 as dependence of the maximum decay

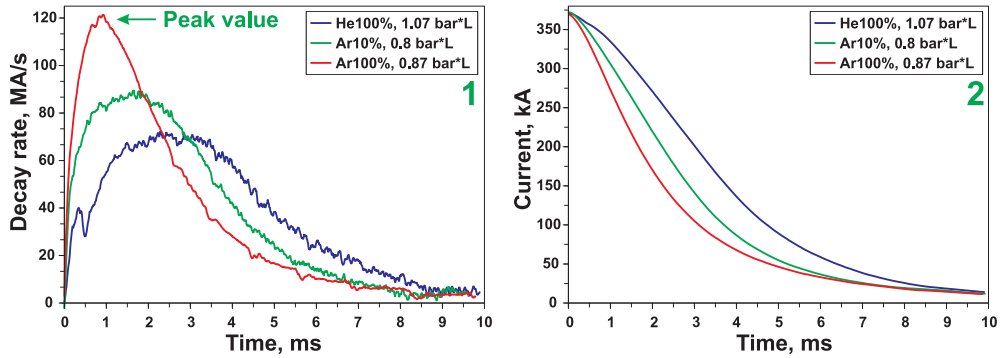


Figure 4.19: Current quench phase for different gases. 1 - derivative of the current - raw signal; 2 - current time traces."Peak value" - the value used for figure 4.20.

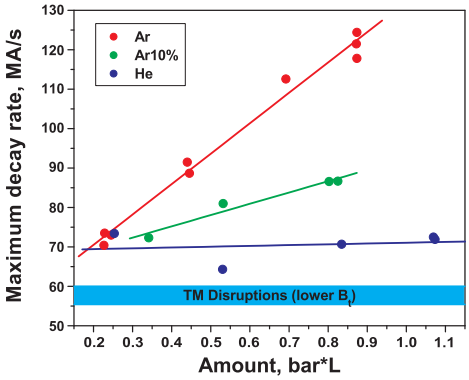


Figure 4.20: Maximum decay rate versus the amount of injected particles for different gases. For comparison the decay rate found in the disruptions initiated by an intentional destabilization of tearing mode is shown.

rate (for definition of the maximum decay rate see figure 4.19) on the amount of injected particles for different gases. Pure argon and mixture containing 10% of argon show a clear trend with the amount of gas, while helium injections seem to be insensitive to the number of introduced atoms. For comparison, the decay rate registered in disruptions initiated by an intentional destabilization of a 2/1-tearing mode is plotted. These disruptions have a much slower current quench.
The presented data are rather qualitative due to the fact that in the experiment the current is measured outside of the vessel, i.e. the signal is smoothed by the vessel resistive time constant. In addition, the argon experiments are to be corrected for the generation of runaway electrons. Both of these question could be to some extent resolved in the course of simple modeling (section 5.6).

### 4.3.2 Runaway electrons

Massive argon puffs were found to provoke strong runaway electrons (RE) generation instead of suppressing it. Evidences of runaway electrons can be found at many diagnostics. Among them there are diagnostics not specially designed for this purpose but recording, for example, hard X-ray noise caused by the losses of runaway electrons (the fast camera, the SXR camera). As standard RE diagnostics the following two are considered: standard neutron detectors and infrared camera for the detection of synchrotron emission.
To begin with, consider the current associated with runaway electrons. This current appears as a long lasting plateau on the current time trace, fig. 4.21. The plateau lasts for about 15 ms until it is finally terminated by a loss of the beam to the wall. The dynamics of the formed runaway beam and the processes leading to its termination are not considered in the present work. Nevertheless it is clear that the beam loss results from some instability. As the amount of injected argon atoms is increased the plateau disappears.
In the case when a plateau of about 100 kA is present the density of runaway electrons is easily estimated:

$$n_{RE} = \frac{I_{RE}}{ecS_{RE}} \approx 3.1 \cdot 10^{16}\ \mathrm{m}^{-3} \tag{4.13}$$

The radius of runaway beam $r_{RE}$ was taken to be of the order of 15 cm. The total number of fast particles is independent on the chosen size $N_{RE} = 2\pi \cdot R_0 S_{RE} n_{RE} \approx 2.4 \cdot 10^{16}$. Since the current carried by relativistic particles is specified only by their velocity $v \approx c$ and not by their energy, the number $N_{RE}$ represents both the low and high energy parts.
The presence of a significant amount of the electrons with energies exceeding 10 MeV is evidenced by their synchrotron emission in the near IR range ($\lambda = 3 \div 5\ \mu$m) and by the pronounced neutron flux.

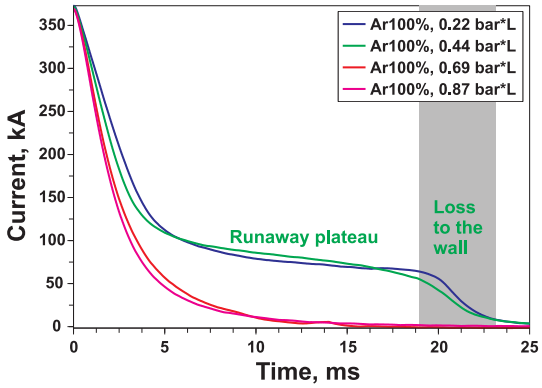


Figure 4.21: The current carried by runaway electrons in massive argon puff experiments.

An example of the "raw" 2D data from the infrared camera ($\varepsilon \geq 20$ MeV) is shown in figure 4.22-3. The runaway beam occupies the central region with dimensions of $\sim 30 \times 30$ cm. Dependence of the intensity of synchrotron emission averaged over the frame on time is given in figure 4.22-1 for several argon shots. The intensity starts to grow at the beginning of current quench and reaches the maximum after 10 – 12 ms. The doubling time of the signal is of the order of 5 ms which coincides with the time required for an electron to gain energy of $20 \div 40$ MeV (section 3.3.4). As the amount of injected gas is increased the synchrotron intensity dramatically decreases, i.e. the number of high energy electrons is diminished, fig. 4.22-2.
In addition, in the runaway discharges significant neutron fluxes (evidence for the electrons with energies $\varepsilon \geq 10$ MeV) are registered, fig. 4.23-1. The temporal behaviour of the neutron fluxes is similar to that of the synchrotron emission. Since neutron fluxes arise mainly from the loss of electrons to the wall (section 3.3.5), the integral of the signal represents the total number of RE accelerated to the appropriate energies. The integrated values are plotted in figure 4.23-2. Again, increasing the amount of injected atoms results in the reduced number of RE. Note that, for the cases when small amounts of argon are injected (< 0.5 bar·l) the neutron detectors are likely to be saturated: at certain moment the curve corresponding to the more sensitive detector (dashed line) drops to zero, while

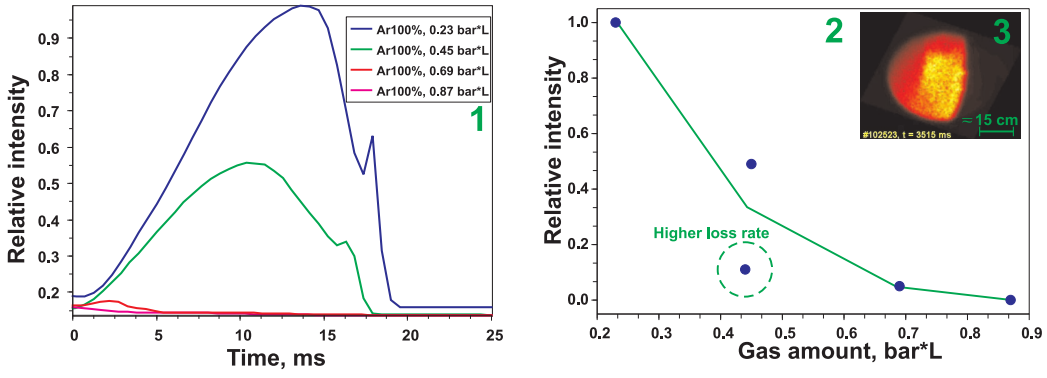


Figure 4.22: Experimental observation of the synchrotron emission. 1 - the intensity of synchrotron emission averaged over the frame for the different amounts of injected gas. Intensities were normalized to the maximum value found in the case of 0.23 bar·l injection; 2 - summary of part 1, dependence of the maximum observed synchrotron intensity on the amount of injected gas. The green line is to guide the eye only.; 3 - insertion showing example of 2D data.

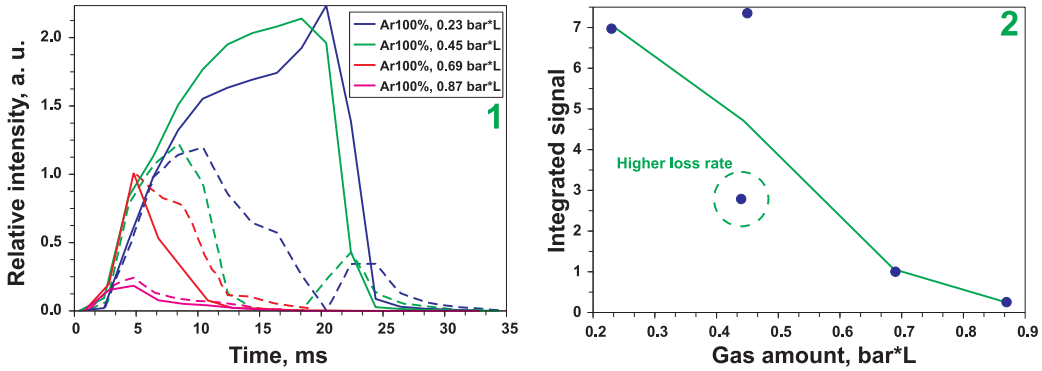


Figure 4.23: 1 - data from neutron detectors normalized to the maximum value of the red curve ($1.45 \cdot 10^{13}$ s$^{-1}$ for the detector "neu_ 3" and $4.45 \cdot 10^{14}$ s$^{-1}$ for the detector "neu_ 4"). Dashed curves correspond to detector "neu_ 3", the solid curves represent data from detector "neu_ 4"; 2 - integrated signal from neutron detector 4 normalized to the value $1.9 \cdot 10^{12}$ corresponding to 0.69 bar·l. The green line is to guide the eye only.

the second signal keeps growing (fig. 4.23-1). For this reason, all values are normalized to the first unsaturated case (injection of 0.69 bar·l).

To sum up, low pressure injections of argon provoke generation of runaway electrons carrying up to 30% of the initial plasma current. The population of these electrons has a considerable amount of high energetic particles ($\varepsilon \gtrsim 10$ MeV). As the amount of injected atoms is increased the total number of accelerated particles decreases, with this statement holding for low energy RE as well as for the high energetic tail. For the first time not only the generation of RE in disruption mitigation experiments was observed, but also the systematic study of their suppression was conducted. To understand qualitative reasons of these phenomena a simple 0D model of the current quench is implemented in the next chapter.

### 4.3.3 Dynamics of the plasma column

After expansion of the emission zone and the wall contact associated with the flattening of the profile in transitive current peak the current channel starts to shrink and its center moves towards high field side during the CQ phase, fig. 4.24. The inward motion of the plasma center is explained by the loss of plasma pressure and the reduction of the inductivity. The control system can not follow changes that are faster than ~ 1.5 ms (skin time of the vessel) and consequently the vertical field determining the plasma horizontal position becomes excessive. The velocity of the radial contraction can be determined from the dependence of the radius on time (fig. 4.24-3) and for this particular case constitutes about 60 m·s$^{-1}$, with the value varying by a factor not more than two between experiments with different gases. The mechanisms able to explain the narrowing of the plasma cross section are: (i) scraping of the outer regions of the plasma by the wall as the column moves horizontally; (ii) initially nonuniform distribution of the impurity atoms in radial direction, which makes the current decay faster at the periphery; (iii) preferential cooling of the outer regions by continuing diffusion of the cold gas staying outside of the plasma. The feasibility of the last mechanism is seen from the following considerations. The ionization rate of, for example, argon at $T_e \sim 10$ eV and $n_e \sim 5 \cdot 10^{13}$ cm$^{-3}$ is about $10^6$ s$^{-1}$ [138], so that the free path of an atom is of the order of several mm only and the preferential cooling should take place.

In the case of low pressure ($p_w < 3$ bar) helium or deuterium injections the current quench is not smooth: transient expansions of the plasma column developing on the time scale of the order of 0.1 ms are registered, fig. 4.25. As the working pressure is increased the

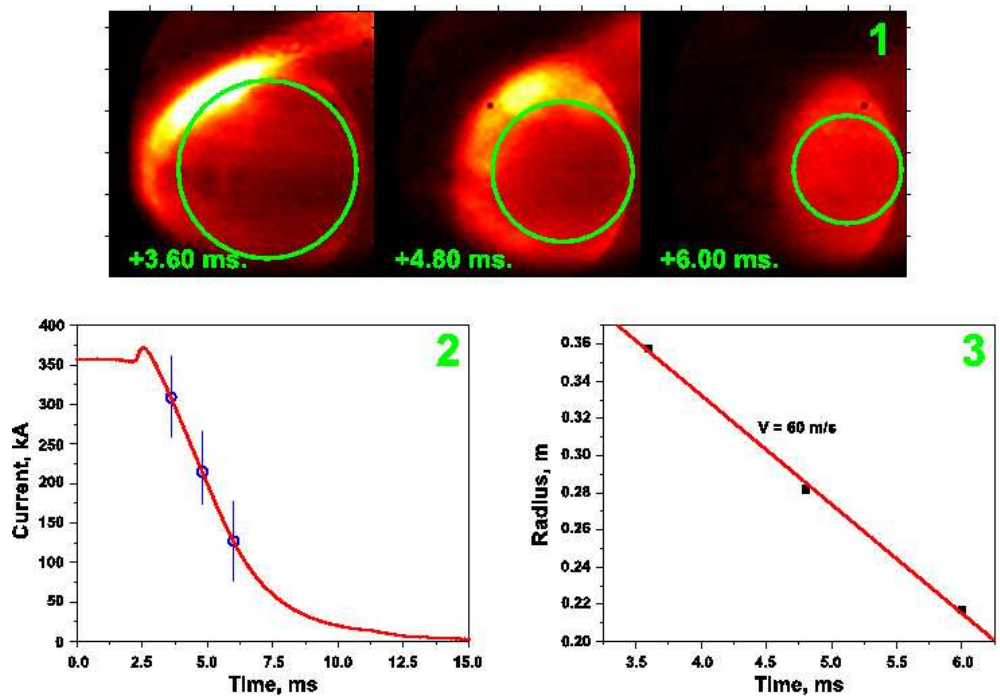


Figure 4.24: Contraction of the plasma channel during current decay. TEXTOR shot 102519, injection of 10 bar of Ar 10% + $D_2$ 90% "x4". Observations were made in ArII 611 light. 1 - the frame sequence obtained with the aid of the fast camera. 2 - plasma current time trace. Indicated are the moments for which the camera frames are shown. 3 - an approximate dependence of the current channel radius on time. The contraction velocity is about 60 $m \cdot s^{-1}$.

MHD activity disappears. The nature of this phenomenon is not understood, but it can be related to high temperatures in the CQ phase. If the temperature of the plasma is sufficiently high, the radial diffusion of the current can be not complete, which could lead to some unstable configuration. Being important for the plasma-wall interaction this effect should be investigated further in future experiments. It is to be noted that Mirnov coils can not be used during this phase because of the strong signal induced by the decaying current.

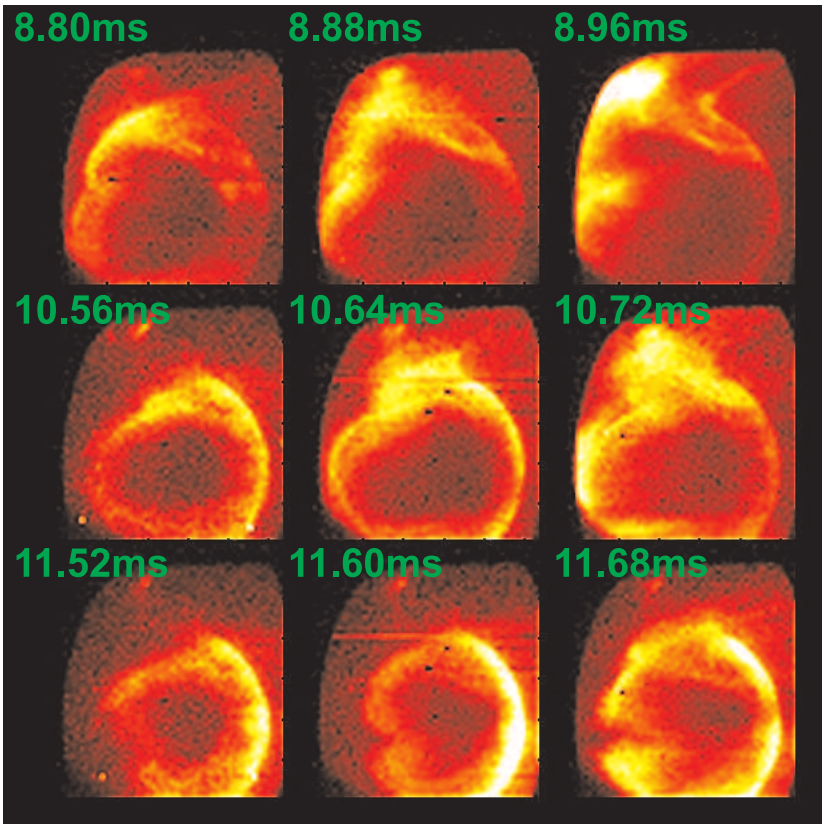


Figure 4.25: Transient expansion of the plasma channel during current decay. TEXTOR shot 99683, injection of 1.9 bar of He "x1". Observations were made in HeI 706.5 light.

# Chapter 5

# Current quench model

This chapter is devoted to the zero dimensional model describing the evolution of the plasma current, plasma temperature and generation of runaway electrons in the current quench phase. Results of the simulations lead to important conclusions concerning decay rate of the current and reasons for the appearance of runaway electrons in argon experiments. For the first time such consideration is systematically applied to the generation of runaway electrons in the experiments on disruption mitigation by massive gas injection.

To understand the main phenomena during the current quench phase, a simple 0D model is developed in what follows. System is described by four coupled equations: an equation for the generation of runaway electrons, an equation for the plasma current evolution, an equation for currents induced in the vessel and an equation for the evolution of plasma temperature. The first one dealing with RE population consists of a combination of eq. 2.27 and eq. 2.34 with an additional general loss channel $\gamma_{loss}$ (for more detailed discussion of generation rates see section 2.3):

$$\frac{dn_{RE}}{dt} = f_{primary}(E, n_e, T_e) + (\gamma_{RE}(E, n_e) - \gamma_{loss}) n_{RE} \tag{5.1}$$

For convenience, formulas for generation rates are listed once more with numerical coefficients expressed in SI units:

$$f_{primary} = 3.82 \cdot \ln\Lambda \frac{\left(n_e[\mathrm{cm}^{-3}]\right)^2}{(T_e[\mathrm{eV}])^{3/2}} \cdot \left(\frac{E_D}{E}\right)^{3\zeta/8} \cdot \exp\left(-\frac{E_D}{4E} - \sqrt{2\zeta}\left(\frac{E_D}{E}\right)^{1/2}\right) \ [\mathrm{m}^{-3}\mathrm{s}^{-1}]$$

$$\gamma_{RE} = 59.975 \cdot \sqrt{\frac{\phi(A_{RE})}{\langle Z^2\rangle + 5}} \cdot (E - E_c) \cdot \left(1 - \frac{E_c}{E} + \frac{4.189 \cdot (\langle Z^2\rangle + 1)^2}{\phi(A_{RE})(\langle Z^2\rangle + 5)(E^2/E_c^2 + 4/\phi(A_{RE})^2 - 1)}\right)^{-1/2} \ [\mathrm{s}^{-1}]$$

$$E_D = 2.61 \cdot 10^{-11} \ln\Lambda \frac{n_e[\mathrm{cm}^{-3}]}{T_e[\mathrm{eV}]} \ [\mathrm{V} \cdot \mathrm{m}^{-1}]$$

$$E_C = 5.091 \cdot 10^{-16}(n_e[\mathrm{cm}^{-3}] + n_{e,bound}[\mathrm{cm}^{-3}]) \ [\mathrm{V} \cdot \mathrm{m}^{-1}]$$

$$\phi(A_{RE}) \approx \frac{1}{1 + 1.46\sqrt{a_{RE}/R_0} + 1.72 a_{RE}/R_0} \approx 1$$

$$\zeta = \frac{1 + \langle Z^2\rangle}{2}$$

$$\langle Z^2\rangle = \sum_j n_j Z_j^2 / n_e$$

$$\ln\Lambda = \ln\left(5.16 \cdot 10^9 \frac{(T_e[\mathrm{eV}])^{3/2}}{(n_e[\mathrm{cm}^{-3}])^{1/2}\langle Z^2\rangle^{1/2}}\right) \tag{5.2}$$

Since the growing runaway population starts to carry an appreciable part of the plasma current, the induced electric field decreases in time - substitution effect. For this reason, the electric field entering these expressions has to be calculated self-consistently. In the 0D case the electrodynamic part reduces to two lumped circuits: the first one describes the plasma current consisting of ohmic and runaway parts and the other is for the currents induced in the vessel structures. It is to be noted that the inclusion of vessel currents is a must due to two reasons. Firstly, because of a non-zero resistive time the vessel screens the outer part of the flux decreasing the induced electric field. This can be seen from the presence of $L - L_v$ instead of $L$ in the expressions given below. Secondly, in the experiment the current is measured outside of the vessel, i.e. it includes both plasma and vessel contributions. Consequently in order to compare with the measurements, one has to simulate the vessel part. As obvious from purely geometrical considerations the mutual inductance between plasma column and vessel can be to a good approximation taken equal to the vessel selfinductance $L_v$:

$$\begin{aligned} \frac{d}{dt}(LI_\Omega + L_{RE}I_{RE} + L_v I_v) &= -2\pi R_0 E_{ind} \\ \frac{dI_v}{dt} + \frac{dI_\Omega}{dt} + \frac{dI_{RE}}{dt} &= -\frac{I_v}{\tau_v} \end{aligned} \tag{5.3}$$

The Ohmic current is related to the electric field by $I_\Omega = SE/\eta$, with $\eta$ being the Spitzer resistivity [133] and the electric field being the sum of the induced field and the field applied by the external transformer: $E = E_{ind} + E_{tr}(t)$. However, the externally applied loop voltage is set to zero in the simulations presented here since the dedicated runs taking

into account measured temporal evolution of the external voltage indicate unimportance of this parameter $E_{tr} \lesssim 1\ \mathrm{V \cdot m^{-1}} << E_{ind} \sim 20\ \mathrm{V \cdot m^{-1}}$.
With a sufficient accuracy the runaway current can be found according to $I_{RE} = ecn_{RE}S_{RE}$, where the velocity of electrons is assumed to equal speed of light $c$. The time for an electron to reach a velocity of $\upsilon \sim 0.9c$ corresponding roughly to $\varepsilon \approx 1.2$ MeV is easy to find from [118]:

$$ceEt = \sqrt{\varepsilon^2 - \varepsilon_0^2} \approx 1\mathrm{MeV} \tag{5.4}$$

For the expected electric field of $E \sim 20\ \mathrm{V \cdot m^{-1}}$ this gives the value of $t \approx 0.15$ ms which is much shorter than the typical time scale of the current decay of about 2 ms. So that the choice of $\upsilon = c$ is reasonable, with exception maybe of the very end of current quench when the runaway current is likely to be overestimated. However, even then the associated inaccuracy is likely to be smaller than variations of the other parameters considered in section 5.3. A more consistent treatment would require a description of the energy of runaway electrons .
The reformulation of the equations for the current decay in terms of the full electric field leads to:

$$\begin{gathered}
\frac{d}{dt}\left(1.9417 \cdot 10^4 (L - L_v) S E \frac{(T[\mathrm{eV}])^{3/2}}{\ln\Lambda \langle Z^2 \rangle} + 4.8 \cdot 10^{-11} S_{RE}(L_{RE} - L_v) n_{RE}\right) = \frac{L_v I_v}{\tau_v} - 2\pi R_0 (E - E_{tr}) \\
\frac{dI_v}{dt} = -\frac{dI_\Omega}{dt} - \frac{dI_{RE}}{dt} - \frac{I_v}{\tau_v} \\
L = \mu_0 R_0 \cdot \left(\ln\left(\frac{8R_0}{r}\right) - \frac{7}{4}\right)
\end{gathered} \tag{5.5}$$

Where the ohmic current is assumed to be uniformly distributed over the whole plasma cross section $S$ and the corresponding internal inductance is 0.25. Nominal values of $\tau_v$ and $L_v$ are $\approx 1.65$ ms and $\approx 2.75\ \mu$H, however in the course of simulations the best results were achieved with 1.45 ms and 2.9 $\mu$H, which are therefore used throughout the rest of the chapter.
The current decay rate and consequently the induced electric field are functions of the plasma temperature and density. As the current decays so does the ohmic heating and the electron temperature accelerating the loop: $I \downarrow \Rightarrow T_e \downarrow \Rightarrow \gamma_I \uparrow$. Substitution effect of runaway electrons worsens the situation even further. For these reasons, self-consistent calculation of the electron temperature is an essential part of the model.
During the current quench the diffusion losses can be safely neglected. Indeed even if the transport were turbulent with $D \sim 1\ \mathrm{m^2 \cdot s^{-1}}$, the characteristic time of such a process would be of the order of tens of milliseconds to be compared with the time scale in question $\tau \sim 2$ ms. Thus, the energy balance is determined by the ohmic heating and radiation of impurity ions:

$$\begin{gathered}
\frac{d}{dt}(n_e T_e) = \frac{2}{3}\left(5.15 \cdot 10^{-5} \frac{\ln\Lambda \left\langle Z^2 \right\rangle}{(T[\mathrm{eV}])^{3/2}} \frac{I_\Omega^2}{S^2} - n_{atoms} n_e \cdot L_{rad}(T_e) - n_e(n_i[\mathrm{cm^{-3}}])\gamma_{ei}(T_e - T_i)\right) \\
\frac{d}{dt}(n_i T_i) = \frac{2}{3} n_e(n_i[\mathrm{cm^{-3}}])\gamma_{ei}(T_e - T_i) \\
\gamma_{ei} = \frac{4e^4\sqrt{2\pi m_e}}{m_p}\left\langle\frac{Z^2}{M}\right\rangle \frac{\ln\Lambda}{T_e^{3/2}} \approx 4.75 \cdot 10^{-9}\left\langle\frac{Z^2}{M}\right\rangle \frac{\ln\Lambda}{(T_e[\mathrm{eV}])^{3/2}} \left[\frac{\mathrm{cm^3}}{\mathrm{s}}\right] \\
\left\langle\frac{Z^2}{M}\right\rangle = \sum_j \frac{n_j Z_j^2}{n_\Sigma M_j}
\end{gathered} \tag{5.6}$$

The energy exchange frequency between electrons and ions is taken according to [55]. The value $\left\langle Z^2/M \right\rangle$ is averaged over all ions and mass the $M$ is expressed in masses of proton. The radiative cooling rate $L_{rad}$ for argon can be found in coronal limit in [130, 131], the same data for helium are presented in [132].

The ionization is assumed to be in coronal equilibrium, so that the electron density $n_e$ is related to the temperature $T_e$ by the expression $n_e = n_D + n_{at}\langle Z\rangle$. To assess the deuterium density $n_D$, it is assumed that the initial particle content of a discharge is evenly redistributed over the whole plasma volume giving rise to $n_D \sim N_{e,tot}/V = 1.4 \cdot 10^{13}$ cm$^{-3}$. The ionization state distribution used to calculate of $\langle Z\rangle$, $\langle Z^2\rangle$ are taken from the same references as the cooling rates.

It is to be noted that for the particular task being considered here the energy equilibration time is shorter than the other typical time scales (see the discussion of the initial conditions below). Consequently the equations 5.6 are equivalent to the balance between the Ohmic heating and the radiative cooling. This equivalance was proved in the dedicated runs. However the solution of the equation 5.6 is preferable from the point of view of the computational time.

All equations of the introduced model 5.1, 5.5, 5.6 have the form $\dot{y} = f(y,t)$ and are easily integrated numerically by the substitution $\dot{y} \approx (y_i - y_{i-1})/h$, where $f$ is estimated at the previous step and the time step $h$ is sufficiently small. To extract the density and temperature from the found pressure $(n_eT_e)^{i+1} = f^i$ this equation is solved iteratively until the desired convergency is achieved: the change of the values in one iteration does not exceed $10^{-7}$.

The chosen initial conditions are:

$$\begin{gathered} n_{RE}(0) = 0 \\ I_\Omega(0) = I_{pl}(0),\ I_{RE}(0) = 0,\ I_v(0) = 0 \\ T_e(0) = T_i(0) = T \\ n_D \sim 10^{13}\ \text{cm}^{-3} \end{gathered} \tag{5.7}$$

The initial value of the temperature is a free parameter to be varied for the best matching of the experimental results. The initial electron density is related to the initial temperature by the condition that at $t = 0$ the radiation is balanced by the ohmic heating. Since calculations are started at the moment when the current starts to decrease (fig. 5.1) and duration of the preceding current peak $\tau_{peak} \sim 200$ $\mu$s is longer than the temperature equilibration time $\tau_T \lesssim 50$ $\mu$s at $T_e \sim 10$ eV, such simplification seems to be justified (compare figures 5.1 and 5.2). In fact it is easy to estimate order of magnitude of time $\tau_T$ by reformulating the energy balance equation to $\tau \sim E/(W_\Omega - W_{rad})$. In the region of interest the energy $E$ is about 10 J·m$^{-3}$ and the radiation power $W_{rad}$ is of the order of 100 MW·m$^{-3}$, so that $\tau_T \sim 10$ $\mu$s. Looking at the problem from the other side, if the introduced initial density is different from an equilibrium one, the plasma quickly relaxes to a new state having the current decay rate different from the experimental one. Even if impurities are introduced in the peak the proposed initial conditions are reasonable. The same considerations are applicable for the electron-ion equilibration time (5.2-2).

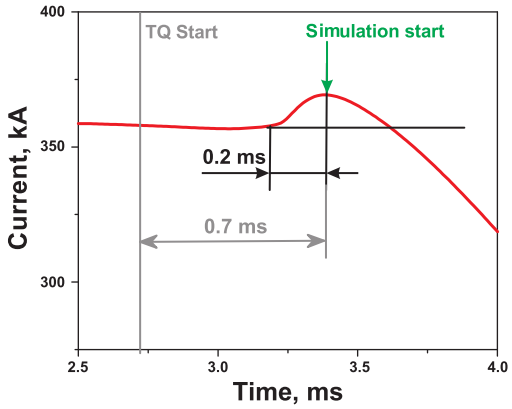


Figure 5.1: Typical duration of the transient current peak.

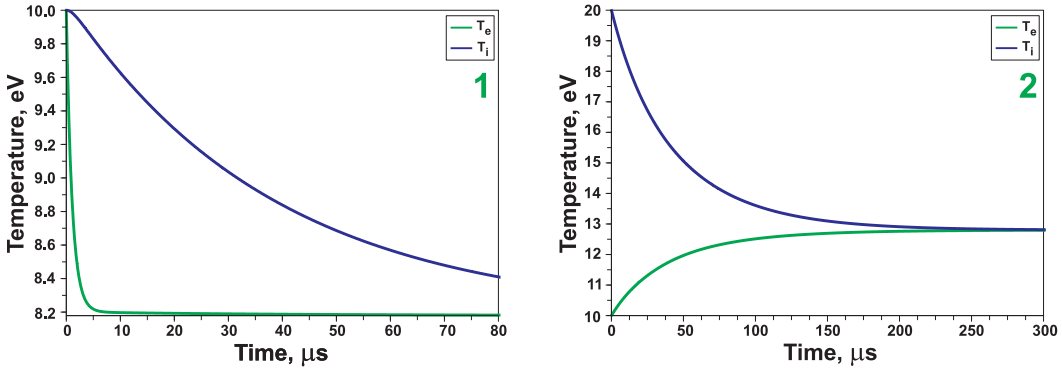


Figure 5.2: Temperature equilibration times. 1 - initial density is chosen to be three times higher than that required by equilibrium. 2 - initial ion temperature is chosen to be twice the electron one. Heating and radiation were switched off. Note, that the total energy is precisely conserved in the system: $\delta E / \langle E \rangle \sim 3 \cdot 10^{-7}$.

To sum up, the model contains a few free parameters to be chosen for the best fitting of the experiment. Among them the density of deuterium $n_D$ and density of injected atoms $n_{atoms}$ are the most important.

## 5.1 Current channel size and contraction

The area $S$ entering the model is to be determined from the experiment. In the positive current peak, the current profile is flattened, therefore it is reasonable to assume a uniform current density over the initial plasma cross section $r \approx 0.4$ m. As shown later (section 5.3) the choice of a plasma radius of 0.3 m instead of 0.4 m strongly reduces the extent of solution region in the 2D space $n_D$, $n_{Ar}$) and increases the found values by a factor of 2. Smaller radii are improbable because $r \approx 0.3$ m corresponds to the predisruptive $q = 2$ flux surface, where the current density before the thermal quench is known to be significant.
In reality, as it has been discussed in section 4.3.3, the current channel is observed to shrink during the current quench. Whatever the reasons for this phenomenon are, the process results in an increase of the plasma current in the hot central region. If the resistivity of the cold region is much higher than that of the plasma center almost all flux is dissipated in the central region. Indeed, let's consider two lumped circuits, with the resistance of one of them being negligible:

$$L_1 \frac{dI_1}{dt} + M \frac{dI_2}{dt} = 0 \tag{5.8a}$$

$$L_2 \frac{dI_2}{dt} + M \frac{dI_1}{dt} = -RI_2 \tag{5.8b}$$

The solution of the system with the given initial conditions $I_1(0)$ and $I_2(0)$ is easily found:

$$L_1 I_1 = L_1 I_1(0) + M I_2(0) \cdot \left(1 - \exp\left(-\frac{R}{L_2 - M^2/L_1} t\right)\right) \tag{5.9a}$$

$$I_2 = I_2(0) \cdot \exp\left(-\frac{R}{L_2 - M^2/L_1} t\right) \tag{5.9b}$$

In the limit of long time the first equation states that the flux is dissipated by the circuit with small resistance:

$$L_1 I_1(\infty) = L_1 I_1(0) + M I_2(0) \tag{5.10}$$

The process is in its nature one dimensional and requires corresponding treatment. In a zero dimensional model it is introduced artificially through a linear in time reduction of the current channel cross section. The contraction rate is determined from the experiment (section 4.3.3). This narrowing of the channel effectively increases the current density and, at the same time, accelerates the current decay due to enhanced resistance $R \sim 1/S$. The value of inductance is recalculated as well, but its effect is weaker owing to the logarithmical dependence on the radius. The introduction of the contraction allows a finer fitting to be performed, but it does not affect the argon and deuterium densities determined from the model.

## 5.2 Simulation of argon injection discharges

Results of the simulation of the TEXTOR discharge 102521 showing a significant runaway plateau are presented in fig. 5.4. The free parameters $T_e(0)$, $n_D$, $\gamma_{loss}$ were chosen to provide the best fit. The Ohmic part of the plasma current decays on a short resistive timescale, at the same time runaway current is generated and significant currents are also induced in the vessel structures. The total current agrees with the experimental measurements reasonably well until the created runaway beam is lost to the wall. The processes related to the beam collapse are not considered in the model. As for the generation mechanism, the third plot (fig. 5.4-3) compares magnitudes of the Dreicer ("primary") and avalanching ("secondary") generation mechanisms. The curves are normalized to the maximum value of the primary mechanism. The Dreicer mechanism prevails for a short time at the very beginning of the CQ, where the induced electric field is relatively high. After less than half a millisecond the primary generation is overtaken by the RE exponentiation. Though staying always lower in magnitude than the peak Dreicer generation the secondary mechanism acts ten times longer leading to a fivefold multiplication of the initial primary population. The found multiplication is in a good agreement with the simple estimation from eq. 2.46. The modeled runaway loss rate is presented along with experimental measurements of neutron flux in figure 5.4-4. In addition the modeled data were resampled to the experimental time resolution of 2 ms (the curve "reduced") with an arbitrary chosen offset. The simulated growth rate of RE losses is similar to that measured by the neutron detectors.

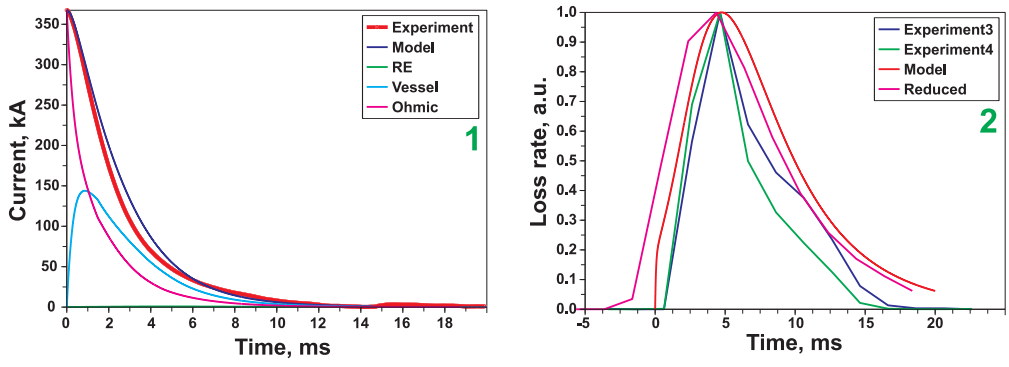


Figure 5.3: Modeling of TEXTOR discharge 102526. 1 - current time traces. Ohmic, runaway and vessel parts of the full current are shown; 2 - comparison of the modeled loss rate with the experimental neutron fluxes. All signals are normalized to their maximum values."Experiment3" is TEXTOR signal "star/neu_3" and "Experiment4" is "star/neu_4". "Reduced" was obtained by averaging simulation result over 2 ms (the time resolution of experimental measurements).

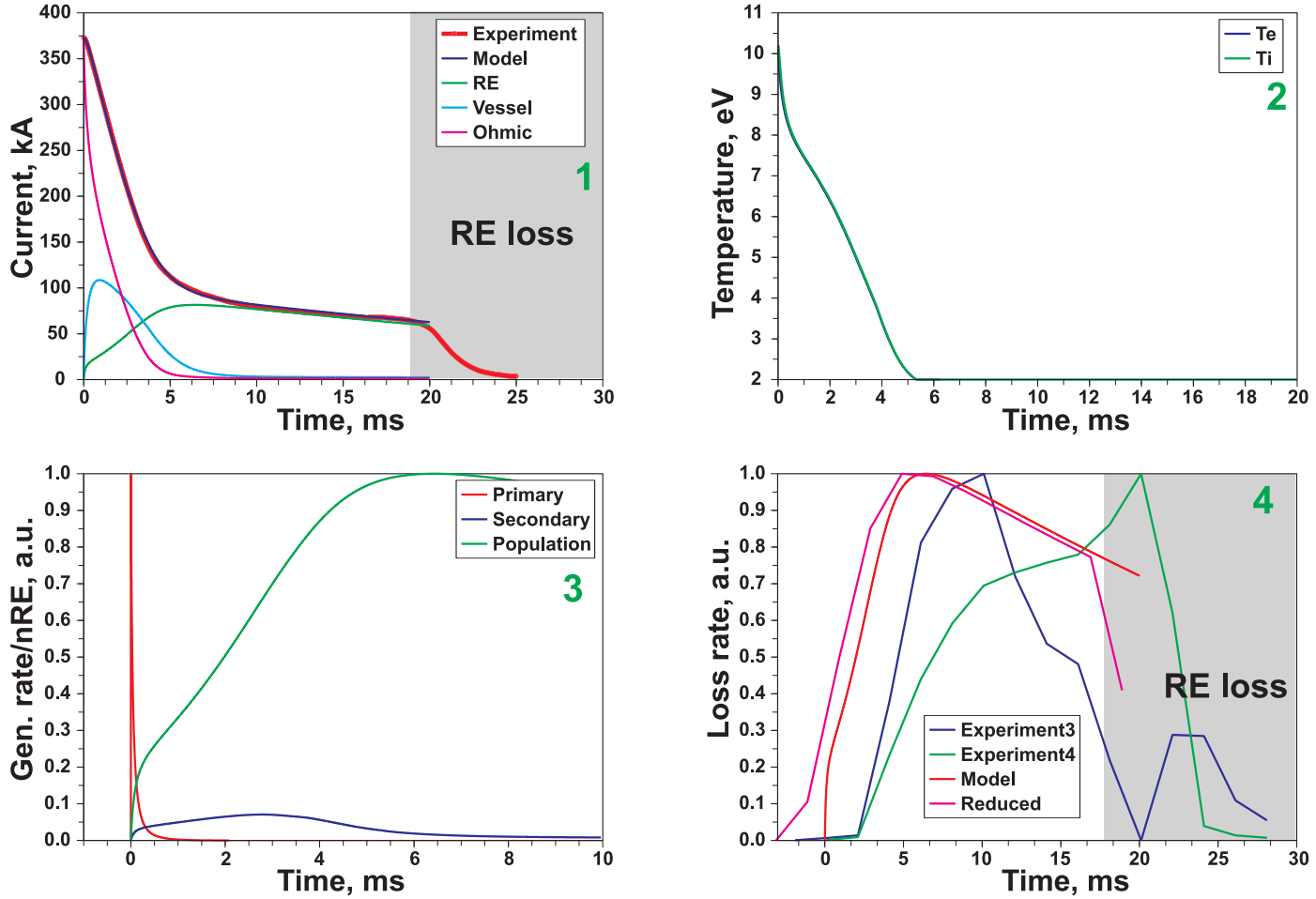


Figure 5.4: Modeling of TEXTOR discharge 102521. The free parameters were chosen to achieve the best coincidence. 1 - current time traces. Ohmic, runaway vessel parts of the full current are shown. 2 - evolution of the electron and ion temperatures; 3 - comparison of the primary and secondary generation mechanisms (normalized to the maximum value of the primary mechanism). Runaway population curve is normalized to its maximum; 4 - comparison of the modeled loss rate with the experimental neutron fluxes. All signals are normalized to their maximum values."Experiment3" is TEXTOR signal "star/neu_3" and "Experiment4" is "star/neu_4". "Reduced" was obtained by averaging simulation result over 2 ms (time resolution of experimental measurements).

| Shot | r, m | $v_r$, m·s$^{-1}$ | $r_{RE}$, m | $\gamma_{loss}$, s$^{-1}$ | $n_D$, $10^{13}$cm$^{-3}$ | $T_e(0)$, eV | $n_e(0)$, $10^{13}$cm$^{-3}$ | $n_{imp}$, $10^{13}$ cm$^{-3}$ | Gas | $N$, bar·l |
|---|---|---|---|---|---|---|---|---|---|---|
| 102514 | 0.4 ÷ 0.25 | 50 | 0.13 | 0 | 1.2 | 18 | 95.2 | 47.3 | He100% | 0.25 |
| 102516 | 0.4 ÷ 0.27 | 70 | 0.13 | 0 | 1.2 | 17.5 | 92.0 | 45.8 | He100% | 0.83 |
| 1025[17,18] | 0.4 ÷ 0.24 | 75 | 0.13 | 0 | 1.2 | 17 | 90.8 | 45.2 | He100% | 1.07 |
| 102519 | 0.4 ÷ 0.23 | 45 | 0.13 | 0 | 1.2 | 4.8 | 21.2 | 19.1 | Ar10% + $D_2$90% | 0.53 |
| 102520 | 0.4 ÷ 0.23 | 45 | 0.13 | 0 | 1.2 | 5.7 | 15.9 | 13.9 | Ar10% + $D_2$90% | 0.34 |
| 102521 | 0.4 ÷ 0.25 | 40 | 0.13 | 52 | 1.2 | 10.2 | 3.5 | 0.77 | Ar100% | 0.23 |
| 102523 | 0.38 ÷ 0.3 | 40 | 0.13 | 60 | 1.2 | 9.6 | 4.16 | 1.01 | Ar100% | 0.45 |
| 1025[24,25,26] | 0.38 ÷ 0.33 | 35 | 0.13 | 210 | 1.2 | 6.1 | 7.57 | 2.71 | Ar100% | 0.87 |
| 102527 | 0.4 ÷ 0.32 | 40 | 0.13 | 50 | 1.2 | 6.5 | 6.33 | 2.1 | Ar100% | 0.69 |
| 1030[03,04] | 0.4 – 0.28 | 45 | 0.13 | 0 | 1.2 | 4.3 | 25.8 | 23.7 | Ar10% + $D_2$90% | 0.85 |

Table 5.1: The best fit values in the massive gas puff experiments. $n_{imp}$ - density of injected atoms. $N$ - number of injected particles expressed in bar·l (note that in the case of deuterium this value corresponds to the number of molecules and not to the number of atoms). Discharge 102528 was excluded due to spontaneous loss of the runaway beam in the initial phase.

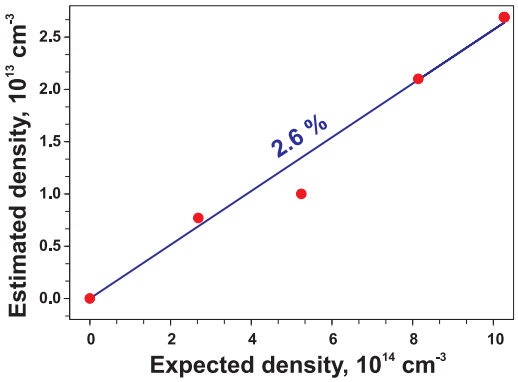


Figure 5.5: Scaling of densities extracted from the model with the expected density. Expected density is the amount of injected particles divided by the vessel volume $n = N/V_v$.

Nevertheless, it is to be remembered that in this shot the neutron detectors are close to the saturation and that the energy of runaway electrons has to be analyzed to make further conclusions. The plot 5.4-2 shows the evolution of the temperature. Even though both electron and ion temperatures are given they are hardly distinguishable. The main finding of such parametric modeling is that the observation of runaway electrons and the energy balance self-consistently require a low argon density of $n_{atoms} = 0.77 \cdot 10^{13}$ cm$^{-3}$.
It is also possible to achieve a good agreement between the experimental and simulated current for discharges without runaway plateau, fig. 5.3 for discharge 102526. Even a better than for shot 102521 similarity is achieved between model loss rate of RE and that measured with the aid of neutron detectors. However a certain care should be taken: the used temperature $T_e \sim 2-4$ eV and electron density $n_e(0) \approx 10^{14}$ cm$^{-3}$ being likely at the limit of the coronal approximation calls for refinement of the used atomic data in future. All parameters found in fitting different argon shots are compiled in table 5.1.
The densities of argon extracted from the modeling (tab. 5.1) are plotted in figure 5.5 in dependence on the density to be expected for a uniform distribution of injected atoms $n_{exp} = N/V$, where $V$ is volume of the vessel. The found densities scale linear with the amount of injected atoms. But only about 2.6% of the introduced atoms reach the central regions critical for the current decay and generation of runaway electrons. It is in fact this low mixing efficiency (the ratio of estimated to expected density) that is responsible for the appearance of a large runaway population in the argon experiments. The inefficient mixing of argon is likely to be explained by a short duration of the thermal quench $\sim 0.5$ ms combined with a large mass of argon atoms. Below it is shown that this efficiency is much higher for the injections of helium and mixture containing 10% of argon.
One has to note that for the argon puffs without a runaway plateau (the last two points in figure 5.5), the current decay rate measured experimentally is limited by the vessel time constant $\tau_v \approx 1.5$ ms. The confidence in the result is provided by the fulfilled energy balance and by the registered neutron fluxes. In spite of being one order of magnitude lower than in shots with RE plateau the neutron fluxes are still much higher than in the case of helium injections. Thus, the suppression of runaway electrons is rather marginal. The overall error in the found mixing efficiency does not exceed a factor of $2-4$ as analyzed in the following section.

## 5.3 Sensitivity analysis

To assess the accuracy of determined densities a simple sensitivity analysis is performed in this section. The analysis is based on the representation of calculation results in 2D

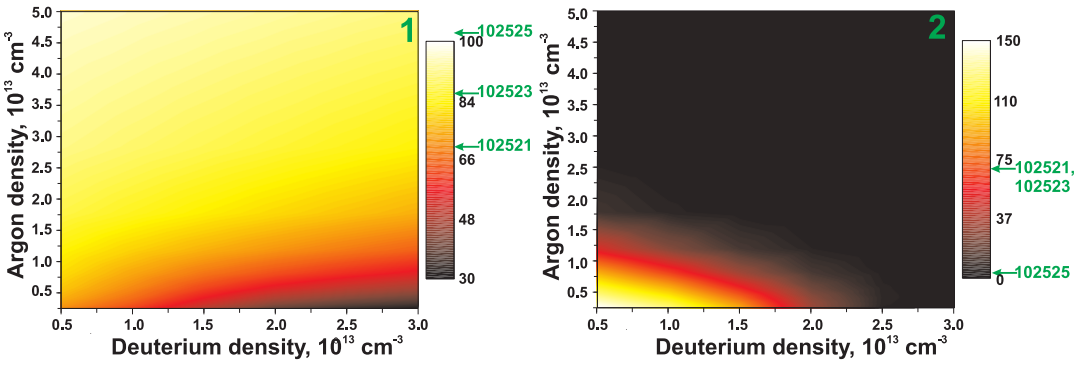


Figure 5.6: Contour plots in $n_D/n_{Ar}$ space with $\gamma_{loss} = 0$, $v_r = 0$, $r = 0.4$ m. 1 - decay rate of the full current [MA·s$^{-1}$]. 2 - runaway current during the plateau phase [kA]. The values measured in several TEXTOR discharges are marked on the colorbars.

space $n_D/n_{Ar}$ (deuterium density/argon density).
For comparison with the experiment two characteristic values are chosen: (i) decay rate of the full current averaged over the period $0.5 \div 1$ ms and (ii) the runaway current during the plateau phase. The variation of simulated current between these two limits is not considered for the purposes of this section, since exactly this behaviour is influenced by the other parameters like contraction velocity, loss rate etc. The values of $\gamma_{loss}$ and $v_r$ are set to zero, the former one would require a slightly lower argon density and the latter one does not influence found results considerably.
The starting point is the case with all theoretical rates as used before and the plasma current profile flat over $r = 0.4$ m. These results are given as colored contour plots in figure 5.6, on colorbars values measured in several TEXTOR discharges are designated. The current decay rate increases with argon density, while the runaway plateau decreases. In addition, as it is obvious from the plot, the full current decay rate saturates at the value specified by the vessel time constant $\tau_v$, i.e. error bars in determined densities grow in that region. The maximum value of decay rate found in the plot is about 15% lower than that obtained from the experiment. A better agreement is easy to obtain by finer adjustment of the vessel parameters, but this way is not followed here.
It is the balance between decay rate and runaway plateau that determines densities listed in the table 5.1. Assuming accuracy of current measurements to be about 10 kA one can find solution region $n_D/n_{Ar}$ by superimposing contours for decay rate and runaway current - the shaded region in figure 5.7-1. The accuracy of found argon density determined by the extension of the solution region is not worse than 50%. The "motion" of the solution region in the 2D space with a change of the other model parameters characterizes the overall accuracy of the extracted densities.
It is worth while noting that deuterium densities lower and higher than shown in figure 5.7-1 are improbable. Even if the whole deuterium content of a discharge were uniformly redistributed over 17 m$^3$ vessel it would require final density about $0.6 \cdot 10^{13}$ cm$^{-3}$. While the maximum limit on $n_D$ is specified by the initial central density $3 \cdot 10^{13}$ cm$^{-3}$.
To determine sensitivity of the result on the other parameters the latter were varied in wide limits:

1. The vessel time constant $\tau_v = 1 \div 2$ ms. Variation around used value of 1.45 ms shows negligible effect of this parameter.

2. The vessel self inductance $L_v = 2 \div 3.5$ $\mu$H. Decrease of $L_v$ and consequently of the mutual inductance plasma-vessel releases more energy to drive runaway current. To keep number of runaway electrons at constant value particle density should be increased. Found influence is not more than 20%.

3. Plasma minor radius $r_{pl} = 0.3 \div 0.4$ m. Poloidal size of the plasma column affects both ohmic current decay rate by changing resistance $R \sim 1/S$ and the energy balance by changing ohmic heating $\sim j^2 \sim 1/S^2$. Decrease of plasma radius to 0.3 m raises best fit argon density twice. Further decrease does not look feasible due to reasons mentioned in section 5.1 and to the fact that solution region shrinks unnaturally (fig. 5.7). To keep solution region below $n_D = 3 \cdot 10^{13}$ cm$^{-3}$, the lower limit is assumed to be about 0.35 m. Experimental refinement of the current distribution is invaluable.

4. Runaway beam minor radius $r_{RE} = 0.05 \div 0.2$ m. Evidently more runaway electrons are required to carry the same total current through smaller area (current density is higher). At $r_{RE} = 0.05$ m found argon density is decreased and vice versa for $r_{RE} = 0.2$ m. The changes are of the order of $20 - 30\%$.

5. Radiative cooling rate is multiplied by a factor $0.5 \div 2$. At both limits the required argon density is slightly reduced.

6. Primary generation rate is multiplied by a factor $1 \div 10$. Primary runaway generation rate is confirmed experimentally only within an order of magnitude [54]. An order of magnitude increment of the preexponential factor raises argon density by $20 - 30\%$.

7. Secondary generation rate is multiplied by a factor $1 \div 2$. In spite of the secondary mechanism being more determined than the Dreicer one its rate is also adjusted by a factor of 2 for generality. Since most of electrons are produced in avalanche (fivefold multiplication), moderate change of the corresponding growth rate $\gamma_{RE}$ in two times shifts limit on argon density upwards by 30%. This increase is unlikely to be realistic, particle trapping in toroidal geometry tends rather to reduce secondary generation rate than to enhance it.

8. Initial conditions on currents $I_{pl} = I(0) + 100$ kA, $I_v = I(0) - 100$ kA. In calculations before the initial value of the plasma current was set to experimental total current at the peak. In reality the measured value is the sum of the vessel and plasma parts. Therefore initial values are varied by 100 kA, while the sum is kept equal to the experiment. In such case the argon density is shifted upwards by a factor of 1.4. The used increment of 100 kA seems to be exaggerated. As change of inductance in full flattening of the results in about 30% variation of inductance $L(-\infty)/L(0) = 1.3$, variation of the current preserving energy is given by $I(0)/I(-\infty) = \sqrt{(L(-\infty)/L(0))} \sim 1.13$, i.e. increment of 50 kA for the discharge under investigation. It would be possible to refine initial conditions if experimental measurements of currents flowing in the vessel were available.

9. The "worst case". The worst case is constructed by combining all variations tending to increase argon density, this includes: $L_v = 2\ \mu$H, $r_{pl} = 0.35$ m, $r_{RE} = 0.2$ m, $f_{primary} \times 10$, $E_c \times 0.5$, $\gamma_{RE} \times 2$, $\gamma_{loss} = 0$. The density change is limited by a factor of 4.

The outcome for several listed cases is represented in figure 5.7-2. It can be concluded from the plot that the absolute values of the argon density are known within a factor $2 - 4$, with deuterium density being in fact undetermined. To refine densities a better knowledge of plasma current profile and/or of the vessel currents is required.

Summing up, if all essential processes are considered in the model, then the modeling can be brought into good agreement with the experiment under the assumption, that the inward mixing of argon is ineffective providing less than 10% of injected argon in the central part of plasma. With high probability the amount of argon in the center reaches only several percents, fig. 5.5.

There is still another fundamental restriction of the model. While the average nature of the found densities is obvious, the zero dimensional treatment employed here also excludes the possibility of the electromagnetic screening of the central regions. The estimated skin time $\tau \sim (4\pi\sigma\delta r^2)/c^2$ for $\delta r \sim 15$ cm is of the order of the typical duration of the CQ or even longer in the helium case. From this point of view the densities are to be considered as the upper limit since screening would reduce the energy to drive runaway current.

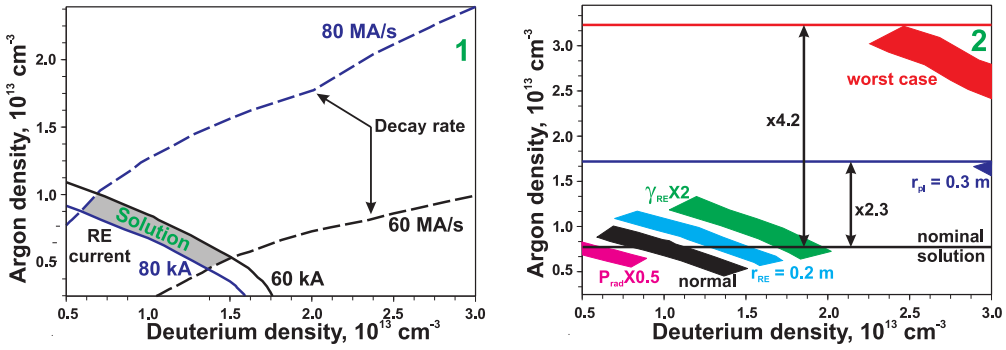


Figure 5.7: Sensitivity analysis. 1 - superimposed contour plots of the decay rate and runaway current for the experimental values taken from the TEXTOR discharge 102521, the accuracy of the current measurements is assumed to be 10 kA. The shaded region gives the solution of the problem. 2 - position of the solution region for different input parameters. "$P_{rad} \times 0.5$" - radiative cooling rate reduced by a factor of 2; "normal" - the solution displayed in the plot 1; "$r_{RE} = 0.2$" - radius of runaway beam 0.2 m; "$\gamma_{RE} \times 2$" - the secondary generation rate enhanced by a factor of 2; "$r_{pl} = 0.3$" - plasma minor radius 0.3 m; "worst case" - the worst case solution, $L_v = 2$ $\mu$H, $r_{RE} = 0.2$ m, $r_{pl} = 0.35$ m, $f_{primary} \times 10$, $\gamma_{RE} \times 2$, $E_C \times 0.5$

## 5.4 Simulation of mixture injection discharges

Simulations of injections of the 10% argon mixture (for the other mixtures current measurements are not available due to the saturation of the integrators) are performed under two major assumptions: (i) the energy is lost only through radiation of argon and (ii) the mixture composition, i.e. the ratio argon/deuterium, is preserved in the central part of the plasma. Figure 5.8-1 shows colored contour plots of the current decay rate averaged over the period $0.5 \div 1$ ms for different combinations of the background deuterium density and the density of injected atoms including both argon and deuterium (two atoms per molecule). The values of the decay rate from a number of discharges are indicated at the colorbar. Runaway current is not presented because of its being many orders of magnitude less than the current carried by the thermal electrons. The density of injected atoms still can be estimated on basis of the decay rate with an expected accuracy about a factor

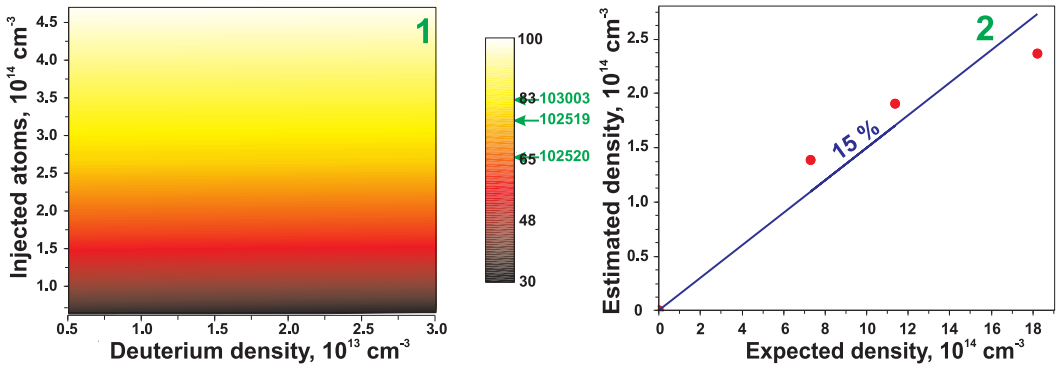


Figure 5.8: Simulations of mixture (Ar 10%+$D_2$ 90%) injection experiments. 1 - contour plots of the current decay rate [MA·s$^{-1}$]. 2 - scaling of the densities extracted from the model with the expected density. Expected density is the amount of injected particles divided by the vessel volume $n = N/V_v$.

of $1.5 \div 2$. The background density $n_D$ on the other hand can not be found owing to the order of magnitude higher amount of puffed deuterium. The fitting results are listed in table 5.1 and are summarized in figure 5.8-2 in dependence on the expected density. The mixing efficiency of 15% is much higher than that for the pure argon experiments, which can be explained by a lower average cooling capability per atom of mixture and/or by a lower average mass.
The strongest assumption made above is that of the preserved mixture composition. The hypothesis is likely to be violated if free streaming along field lines in radial direction takes place. In that case the composition should change according to the mass ratio, however the drag force would tend to preserve the ratio. While leaving out quantitative discussion we note that a lower ratio of argon would only mean even better efficiency of deuterium delivery, since the decay rate depends mainly on the argon amount. That is the given efficiency of the mixture injection is to be considered at least as a lower limit.

## 5.5 Simulation of helium injection discharges

Simulations of helium experiments are conducted as described for argon or mixture cases with exception that argon atomic data are substituted by those for helium. An example of a fitted experimental current time trace for a typical shot with helium injection is given in fig.5.9-1. The runaway current is again negligible, so that determination of the mixing efficiency is once more based only on the decay rate of the plasma current providing an accuracy of about a factor of 2. The current decay rate in helium experiments turned out to be fairly constant for all used working pressures $p_w = 5 \div 20$ bar (see figure 4.20 and its discussion). As a consequence helium densities found from parametric modeling are also almost constant for all considered discharges (table 5.1). The tendency of the number of atoms to increase with electron temperature is related to the proximity of the peak of helium radiative cooling rate. The chosen starting temperatures are higher than the value at the maximum of cooling rate. In this case the lower temperatures required for higher current decay rates correspond to a lower density of helium. Since these variations are much lower than any of the related uncertainties this tendency was not investigated further. The number of impurity atoms extracted from the fitting procedure is shown in figure 5.9-2 in terms of the mixing efficiency. It is to be noted that despite remaining within claimed accuracy the density found for low pressure injection (point marked as "overestimated") can be overestimated due to the presence of intrinsic impurities. The radiative cooling rate of helium is three orders of magnitude lower than that of argon, consequently a presence of small amount of intrinsic better radiating impurities like carbon or oxygen in the center

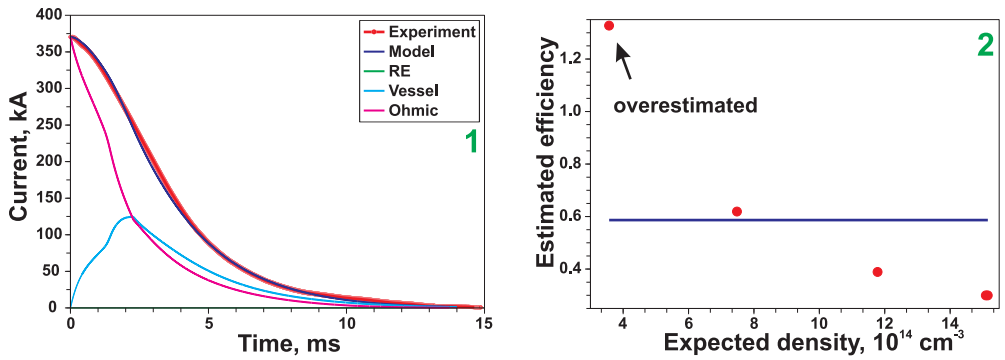


Figure 5.9: Simulations of helium injection experiments. 1 - an example of the fitted data; 2 - mixing efficiency, i.e. the ratio of the estimated density to the expected value. Expected density is the amount of injected particles divided by the vessel volume $n = N/V_v$.

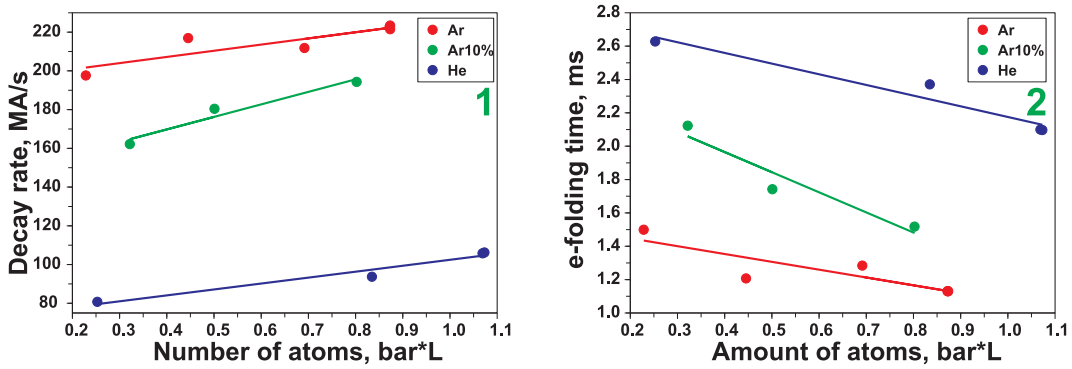


Figure 5.10: Decay of the ohmic plasma current according to simulations. 1 - the decay rate averaged over the first millisecond of the process; 2 - e-folding time, i.e. time for the current to decrease in 2.72 times.

of the plasma can strongly affect the result. Due to the lack of information concerning concentration of such impurities, they are not included into the model. Nevertheless, the presented results indicate that the delivery efficiency of helium reaches about 50% and is again much better than that in the case of pure argon puffs.

## 5.6 Current decay rate

Returning to the questions raised in section 4.3.1 about measurements of the current decay, the performed modeling allows the decay rate of purely ohmic part of the plasma current to be extracted. The behaviour of this ohmic part is characterized in figure 5.10 by two parameters: decay rate averaged over the first millisecond of the process (the first subfigure) and one e-folding time (the second subfigure). Argon clearly results in the highest decay rate, which is partially caused by the runaway substitution effect, while the slowest quench is observed in the discharges terminated by helium. In spite of being strongly diluted, the argon mixture (Ar 10%+$D_2$ 90%) closely approaches the pure argon in terms of the decay rate. However, care should be taken in interpreting this proximity because of the poor accuracy of the results at the limit 230 MA·s$^{-1}$ specified by the vessel time constant $\tau_v \approx 1.5$ ms. It is also worth noting that with exception of the slow helium experiments the peak decay rate of the purely ohmic part extracted from the model (fig. 5.10-1) is a factor of 2 higher than the decay rate of the full current measured experimentally (fig. 4.20). The same conclusions as done above can be drawn from the dependence of the e-folding time on the amount of injected gas (fig. 5.10-2). To conclude, control of the current decay rate required for optimization of electromagnetic stresses on the vessel (sec. 2.4.2) and in particular acceleration of the CQ phase for reduction halo currents can be easily achieved by a careful choice of the working gas. Due to good cooling capabilities high-$Z$ materials provide the fastest current quenching. The amount of injected atoms, on the other hand, has a weaker influence on the decay rate.

## 5.7 On the nature of runaway electrons suppression

The other important point to be addressed is the reason for the appearance and suppression of runaway electrons in argon puff experiments. The theory of RE generation (sec. 2.3) predicts a dependence on two main parameters $E/E_c$ and $E_D/E$. The ratio of the induced field to the critical one $E/E_c$ characterizes the possibility of runaway electrons acceleration, with values above 1 corresponding to the generation of runaway electrons and those below 1 to unconditional suppression. While the ratio of the Dreicer field to the induced one

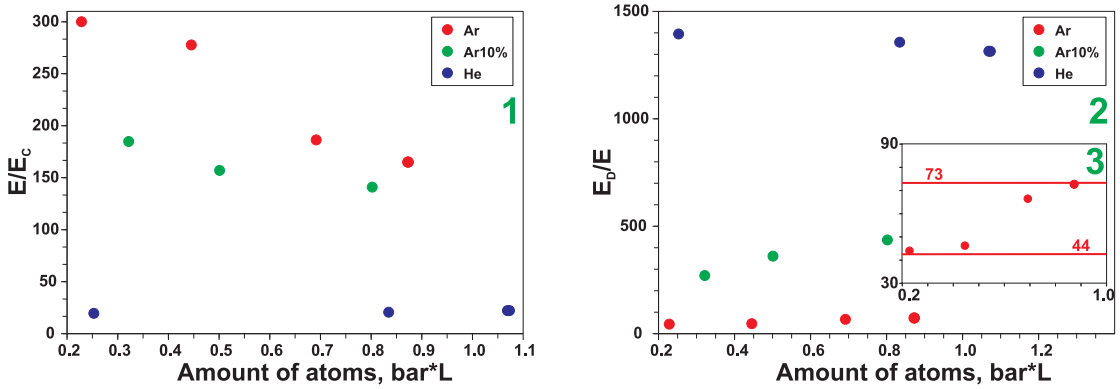


Figure 5.11: Comparison of critical and Dreicer fields with the induced one. 1 - $E/E_C$, the value more than 1 indicates that the generation of runaway electrons is possible; 2 - $E_D/E$, the higher the value the lower the amount of primary electrons; 3 - insertion showing the enlarged lower portion of the graph 2.

$E_D/E$ enters exponentially into the rate of the primary generation mechanism (eq. 2.27). Results of the parametric fitting described in the previous sections reveal that $E/E_c$ stays always above 1 (fig. 5.11-1), i.e. the generation is in principle possible and is determined by the seed population resulting from the primary mechanism and by the competing loss channels. If the secondary multiplication factor were comparable to ITER ($\exp(50)$) even small seed populations would be enormously enhanced. Nevertheless, the advantageous tendency of lowering the ratio $E/E_c$ with the increased amount of injected gas is obvious. The lowest critical ratio is observed in helium injections. As for the primary mechanism, in helium and argon mixture puffs the ratio $E_D/E$ is at least by one order of magnitude higher than in the pure argon case (fig. 5.11-2), which makes the primary mechanism proportional to $\exp(-E_D/E)$ ineffective. In low pressure argon experiments the ratio $E_D/E$ is low enough to initiate RE creation. The increase of injected amount of argon results in increase of $E_D/E$ in modest 1.65 times (fig. 5.11-3) corresponding to the fivefold drop of the generation rate. Comparing the current decay rates and the delivered density one can conclude: it is the low mixing efficiency of the pure argon that is responsible for the generation of runaway electrons and it is the low multiplication factor of avalanching that leads to the absence of RE in experiments with other gases and disappearance of RE at larger amounts of injected argon.

# Chapter 6

# Conclusions

Disruptive instabilities represent a threat for tokamak experiments and reactors to come. In this thesis the studies related to disruption mitigation by massive gas injection were presented.

In the first part of the work the fast valve activated by eddy currents was analyzed. Because of the immunity to high static and slow varying magnetic fields this valve is a good choice for tokamak applications. It was demonstrated that such vital characteristics of the valve as throughput (efficiency) strongly depend on the valve configuration. Use of helium in the back chamber and of overpressure $q = 1.5$ in the working one gives rise to a $2 \div 4$-fold increase of the valve throughput. The novel direct video observations revealed the interplay between these improvements and the piston motion. Piston deceleration by gas in the back section was proposed to be the reason for the shallower valve opening and shorter injection duration at higher pressures and/or with heavier gases in the back section. The improvement of the throughput arises mainly from the prolongation of the injection duration $t^*$.

The knowledge of the injection duration allowed the measurements of the gas outflow rates. The outflow rates are two times smaller than expected for the outflow of gas with particle density $n$ at sound speed $c_s$ through a hole with area $S$: $nc_sS$. But the flow rates do follow the linear scaling with the square root of mass $\sqrt{m}$. In the TEXTOR experiments the maximum flow rates are about 200 bar·l·s$^{-1}$ ($4.8 \cdot 10^{24}$ particles/s) for argon and more than 500 bar·l·s$^{-1}$ ($1.2 \cdot 10^{25}$ particles/s) for helium. The outflux rates vary only by modest 20% in response to a more than an order of magnitude increase of the valve opening $h$. The latter fact has purely geometrical reason: the gas outflow is limited by the area $\pi r^2$ of the output nozzle $h \gg r$. To exploit the stroke $h$ effectively the modified valve with the diameter of orifice enlarged twice was proposed and used in the experiments at TEXTOR. For the modified valve the maximum flow rates are correspondingly four times larger than given above for the standard valve.

One of the central questions of the present work was to determine the phenomenology of plasma quenching by massive gas injection. To perform this task an ultra-fast framing CCD camera sensitive in the visible range was installed at TEXTOR. Different spectral lines of neutral and singly ionized atoms were observed. A separate word is to be said about the applicability of standard tokamak diagnostics to disruption mitigation discharges, the point that is sometimes omitted. Because of the background plasma light leading to the saturation of detector, the Thomson scattering system is reliable only before the triggered disruption. The temperature measurements based on the second ECE harmonic are restricted by the cut-off resulting from high electron density. For these reasons the Thomson scattering and ECE diagnostics were used only at early stages. To trace plasma evolution during the thermal quench the soft X-ray pinhole cameras were employed.

Terminations of stable discharges were performed by massive gas injections of $(1 \div 20) \cdot 10^{21}$ atoms of different gases (50 discharges in total). The investigated gases are deuterium, helium, argon, mixtures of argon and deuterium with argon content of 5, 10 and 20%. Because of the presence of a toroidal plasma current in the tokamak, the plasma shutdown by massive gas injection is always of disruptive type. That is the energy is removed not only by radiation but also by the convective transport caused by large scale instabilities. The disruption is initiated as soon as the edge safety factor $q_a$ becomes equal to 2, i.e. the effective plasma boundary is moving together with the cold front inwards and the disruption occurs at the time when $q_a$ at this boundary is 2. This fact was confirmed with an accuracy of 1 – 2 cm by the observations of the cold front with ECE and Thomson scattering diagnostics and by the observations of the emission front with the fast framing camera. The position of the emission front was inferred from the comparison of the experimental images with the images simulated for the optically thin plasma. In addition, simple comparison of the energy lost by the discharge with the energy consumed by the injected atoms showed that in all experiments, with the exception of maybe low pressure injections of deuterium, the position of the emission front has to coincide with the penetration depth of injected particles.

The thermal quench is characterized by bursts of X-ray emission, MHD fluctuations and a

negative spike of the limiter potential. Neither the cold front nor the emission front propagates into the center of the plasma, the discharge collapses simultaneously. The duration of the thermal quench does not depend on the number of particles if this number is larger than 0.2 bar·l ($4.8 \cdot 10^{21}$ particles). Mixtures containing argon cool the core plasma in about 0.5 ms, while in the helium experiments this phase lasts about 1 ms. For less than 0.2 bar·l ($4.8 \cdot 10^{21}$ particles) of atoms of helium, deuterium or mixtures containing less than 20% of argon the duration of the thermal quench drops as the number of particles is increased. It is to be noted that for such injections (< 0.2 bar·l) of helium or deuterium the thermal quench consists of two steps.

The disruptive nature of the massive gas injections was also confirmed by the presence of the positive current peak at the beginning of the current quench. This peak is known to be the disruption feature related to flattening of the current profile with conserved magnetic energy $LI^2/2$. The instability leading to the disruption is likely to be a 2/1 kink/tearing mode.

The current decay rate is affected by the choice of gas type and number of injected particles. The slowest decay rates of about 70 MA·s$^{-1}$ and in addition a weak dependence on the number of atoms are typical for helium experiments. While shots terminated by argon showed decay rates of up to 120 MA·s$^{-1}$. The acceleration of the current quench is known to be advantageous for the reduction of halo currents. If the plasma current decays faster than the vertical displacement develops, the current directly (not induced eddies) transferred to the wall, known as halo current, is reduced. The acceleration of the current decay, that was found in this thesis in circular plasmas, does not itself depend on the plasma elongation. It is specified by the energy balance in the cold plasma after thermal quench, i.e. by the amount of impurities delivered to the plasma core. In contrast, a direct comparison of the current decay rate with the VDE growth rate is possible only in elongated configurations and should be performed experimentally in the future. In addition, as it is discussed below, the bulk of the injected gas remains at the plasma periphery. Consequently, preferential cooling of the edge plasma is achieved, which is also advantageous for the reduction of halo currents because of the higher plasma resistivity in the halo region.

Injections of less than $10^{22}$ atoms of argon provoked the generation of runaway electrons carrying up to 30% of the initial plasma current. The population of runaway electrons contains a considerable high energy ($\varepsilon \gtrsim 10$ MeV) tail. This can be concluded from the observations of synchrotron emission in the near IR range ($\lambda = 3 \div 5\ \mu$m) and strong neutron/$\gamma$ fluxes. Increasing the number of injected atoms diminishes the density of both low energy and high energy runaways: for the first time not only the generation of runaway electrons during disruptions but also their suppression by massive gas injection was demonstrated. In the experiments with other gases including mixtures with different fractions of argon runaway electrons were not registered.

The current quench was systematically analyzed in the framework of a 0D model. The model consisted of equations for the plasma current, the currents induced in the vessel, the generation of runaway electrons and the evolution of plasma thermal energy in coronal equilibrium. The major free parameters of the model are the density of deuterium $n_D$ and density of injected atoms $n_{atoms}$. These parameters were chosen in such a way as to provide the best matching between the modeled current evolution and that measured experimentally. The necessary condition for the appearance of runaway electrons proved to be low density of injected argon atoms. The mixing efficiency, i.e. the ratio of atoms delivered to the plasma center to the number of injected atoms, constitutes about 3%. The sensitivity analysis of the model indicated that the uncertainty of the determined argon density is not more than a factor between 2 and 3. The strongest source of the errors is the unknown current density profile. Similar modeling of argon mixture and pure helium injections resulted in a mixing efficiency of about 15% and 40% correspondingly.

Runaway electrons are generated by two different mechanisms: (i) the primary mechanism, in which small angle collisions between thermal particles move an electron towards the runaway region; and (ii) the secondary avalanche mechanism, in which an existing

runaway electron knocks out a thermal one immediately into the runaway region. In the case of TEXTOR experiments ($I_p$ = 350 kA), the secondary mechanism does amplify the primary one by a factor of 5. But the leading role is played by the primary mechanism. If the primary mechanism is suppressed, the runaway electrons are absent.

The generation rate of runaway electrons by the primary mechanism is exponentially small $S \sim \exp(-E_D/E)$, where $E_D$ is the Dreicer field characterizing collisional friction. $E_D$ is proportional to the electron density and is inversely proportional to the electron temperature. The induced field $E$ is determined by the plasma resistivity, i.e. by the electron temperature only. It is to be noted that the effective charge $Z$ entering the resistivity is also a function of the temperature and varies between 1 and 2 in the temperature range in question. The temperature is given by the power balance between the impurity radiation and the ohmic heating. As the electron temperature decreases further than the value at which the maximum of radiation is reached (10 – 20 eV), the radiative cooling rate of any impurity drops very quickly. To put it in another way, to cool the plasma further more and more particles are required. As a consequence, the Dreicer field $E_D \sim n_e$ grows much faster than the induced one, and runaways can be suppressed with sufficient amount of injected atoms.

In the experiments with helium or mixtures of argon with deuterium the condition $E_D \gg E$ is achieved even with the smallest used number of injected atoms ~ $10^{21}$. While because of the mixing efficiency of argon being five times smaller than that of mixture of argon with deuterium, in experiments with pure argon the condition $E_D \gg E$ is fulfilled only when the number of injected atoms exceeds about $10^{22}$. The suppression of runaway electrons by an increased amount of argon and the absence of the generation in the experiments with other gases is explained by the inefficiency of the primary mechanism ($E_{ind} \ll E_D$) and a small multiplication factor of about 5 for the generation of secondary runaway electrons.

In ITER the situation will be completely different. The primary mechanism will be effectively suppressed, but due to the enormous secondary multiplication factor of about exp(50) even a single background electron, that can be produced, for example, by Compton scattering, will result in a strong runaway beam. For this reason, to prevent the formation of a runaway beam, the possibility of running away has to be eliminated. The minimal collisional friction has to exceed the induced field. This condition is conveniently expressed in terms of the critical field: $E < E_C$. The critical field $E_C$ is proportional to the density of free and bound electrons. The electron density needed to achieve $E << E_C$ is significantly higher than the density required to suppress the primary mechanism.

Potentially argon has the largest amount of electrons (18) and the full mixing could provide electron density required for the unconditional suppression of runaway electrons. However, the found inward mixing of argon is incomplete and of the order of 3%. To approach the condition $E = E_C$ the total number of introduced atoms has to be increased by more than an order of magnitude. Scaling of the required number of atoms towards larger tokamaks requires more detailed understanding of the reasons for this limited mixing and knowledge of dependence of the mixing efficiency on the main parameters of terminated discharge. But already now it is clear that the massive gas injections of mixtures of heavy, good radiating atoms with deuterium can be preferable because of the better mixing efficiency (~ 15%). Of course, the verification of these results in a larger tokamak like JET is desirable.

In spite of the made progress it is still not possible to draw a final conclusion about the applicability of the disruption mitigation by massive gas injection in the next step experiment ITER. From the technical point of view, according to the findings of this thesis the system of several fast valves should be able to inject as much atoms as can be tolerated by the vacuum system of tokamak. The injected atoms provide acceleration of the current decay and preferential cooling of the halo region. Consequently the electromagnetic loads on the vessel due to halo currents are reduced. However the disruptive nature of the shutdown calls for a more detailed analysis of the thermal energy dissipation. Only the energy stored outside of the position where the edge safety factor $q_a$ is equal to 2 is consumed by the dilution and radiation before the disruption. The fraction of energy radiated during the

induced thermal quench, as well as the toroidal symmetry of the radiation, has still to be determined. A better understanding of the poor mixing is also required.

Apart from scaling the data towards ITER, one has to verify some findings of the presented work in a more direct or solid way. From the experimental point of view, to confirm the used model it is necessary (i) to measure the density and temperature during the current quench and (ii) to determine the current density profile that was shown to be the most critical for the accuracy of modeling. Theoretical studies of the gas penetration before the thermal quench can explain the reasons for plasma disruption. Such simulations could be directly compared with the experimental observations of the atoms dynamics with the fast camera. The development of an 1D model of the current quench will help to make a more consistent analysis and to take into account a nonuniform distribution of the injected atoms and screening of the central plasma.

Finally, it is worth mentioning that because of the reliable triggering, good reproducibility and well controlled parameters the massive gas injection experiments can be conveniently used for investigation of general physical problems related to tokamak disruptions.

# Appendix A

# Plasma Stability

In this section the energy integral applicable for analysis of the plasma stability is derived. The derivation is based on the ideas that can be found in [14, 15, 17].
Let's consider the plasma column surrounded by a vacuum region and enclosed into a perfectly conducting wall. In the linear approximation perturbations evolve according to the system 1.8, which is easily reduced to the following one by introducing the displacement vector $\vec{\xi}$ and by integrating some of the equations (since the equilibrium values do not depend on time):

$$\rho_0 \frac{\partial^2 \vec{\xi}}{\partial t^2} = \frac{1}{c}\vec{j_1} \times \vec{B_0} + \frac{1}{c}\vec{j_0} \times \vec{B_1} - \vec{\nabla} p_1 \tag{A.1a}$$

$$\rho_1 = -\vec{\nabla} \cdot (\rho_0 \vec{\xi}) \tag{A.1b}$$

$$p_1 = -\gamma p_0 \vec{\nabla} \cdot \vec{\xi} - \vec{\xi} \cdot \vec{\nabla} p_0 \tag{A.1c}$$

$$\vec{\nabla} \times \vec{B_1} = \frac{4\pi}{c}\vec{j_1} \tag{A.1d}$$

$$\vec{B_1} = \vec{\nabla} \times [\vec{\xi} \times \vec{B_0}] \tag{A.1e}$$

These equations have to be supplied by the corresponding boundary conditions. The first of them is that describing the pressure balance:

$$p_0 + p_1 + \frac{1}{8\pi}\left(\vec{B_0} + \vec{B_1}\right)^2 = \frac{1}{8\pi}\left(\vec{B_{v0}} + \vec{B_{v1}}\right)^2 \tag{A.2}$$

where subscript "v" refers to the vacuum region. This expression is fulfilled on the disturbed surface. To obtain condition on the equilibrium surface it should be expanded to give in the first order:

$$\xi_n \frac{\partial p_0}{\partial n} + p_1 + \frac{1}{4\pi}\vec{B_0} \cdot \vec{B_1} = \frac{1}{4\pi}\vec{B_{v0}} \cdot \vec{B_{v1}} + \frac{\xi_n}{8\pi}\left(\frac{\partial B_{v0}^2}{\partial n} - \frac{\partial B_0^2}{\partial n}\right) \tag{A.3}$$

The other boundary condition to be used later results from the fact that the electric field in the plasma framework is zero $\vec{E} + [\vec{v} \times \vec{B}]/c = 0$. Since the tangential component of the electric field is continuous, it follows that:

$$\vec{n} \times \vec{E} = \frac{1}{c} v_n \vec{B_{v0}} \tag{A.4}$$

By using the Maxwell equation $\partial\vec{B}/\partial t = -c\ rot\ \vec{E}$ and integrating the equation one arrives to the final boundary condition at the plasma-vacuum interface ($\vec{A}$ is the vector potential of disturbance of the vacuum magnetic field $\vec{B_{v1}} = rot\ \vec{A}$):

$$(\vec{n} \cdot \vec{B_{v1}}) = \vec{n} \cdot rot[\vec{\xi} \times \vec{B_{v0}}] \Rightarrow [\vec{n} \times \vec{A}] = -\xi_n \vec{B_{v0}} \tag{A.5}$$

As both terms are small values the condition is fulfilled at the equilibrium boundary. At the vacuum-wall interface this condition is modified to:

$$[\vec{n}\times\vec{A}] = 0 \tag{A.6}$$

The potential energy of perturbations is:

$$\delta W = -\frac{1}{2}\int \vec{\xi}\cdot\vec{F}dV \tag{A.7}$$

where the operator $\vec{F}$ is the combination of the corresponding expressions in system A.1.

$$\delta W = -\frac{1}{2}\int \vec{\xi}\cdot\vec{F}(\vec{\xi})\,dV = -\frac{1}{2}\int \vec{\xi}\cdot\left(-\vec{\nabla}p_1 + \frac{1}{c}\vec{j}_1\times\vec{B}_0 + \frac{1}{c}\vec{j}_0\times\vec{B}_1\right)\,dV = -\frac{1}{2}\int\Big(-\vec{\nabla}\cdot(\vec{\xi}\cdot p_1)+$$
$$+p_1\vec{\nabla}\cdot\vec{\xi} - \frac{1}{4\pi}\Big(\vec{\nabla}\cdot\left[\vec{B_1}\times\left[\vec{\xi}\times\vec{B}_0\right]\right] + \vec{B_1}\cdot\left[\vec{\nabla}\times\left[\vec{\xi}\times\vec{B}_0\right]\right]\Big) - \frac{1}{c}\vec{j}_0\cdot\left[\vec{\xi}\times\vec{B_1}\right]\Big)\,dV = \frac{1}{2}\int\Big(\gamma p_0(\vec{\nabla}\vec{\xi})^2+$$
$$+\frac{1}{4\pi}B_1^2 + (\vec{\xi}\cdot\vec{\nabla}p_0)\cdot(\vec{\nabla}\cdot\vec{\xi}) + \frac{1}{c}\vec{j}_0\cdot\left[\vec{\xi}\times\vec{B_1}\right]\Big)\,dV + \frac{1}{2}\int\left(p_1\vec{\xi} + \frac{1}{4\pi}\left[\vec{B_1}\times\left[\vec{\xi}\times\vec{B}_0\right]\right]\right)\cdot d\vec{S} \tag{A.8}$$

In simplifying this expression properties of the triple and vector products were used and in the last transition the Gauss theorem was employed. The surface integral can be transformed by applying the well known rule $[\mathbf{a}\times[\vec{b}\times\vec{c}]] = \vec{b}(\vec{a}\cdot\vec{c}) - \vec{c}(\vec{a}\cdot\vec{b})$ and by noting that the equilibrium magnetic field lyes in the interface $((B_0\vec{\cdot}\,\vec{n}) = 0)$:

$$\frac{1}{2}\int\left(p_1\vec{\xi} + \frac{1}{4\pi}\left[\vec{B_1}\times\left[\vec{\xi}\times\vec{B}_0\right]\right]\right)\cdot d\vec{S} = \frac{1}{2}\int\left(p_1 + \frac{1}{4\pi}\vec{B}_0\cdot\vec{B}_1\right)\xi_n\,dS - \frac{1}{2}\int(\vec{\xi}\cdot\vec{B_1})\cdot(\vec{B}_0\cdot\vec{n})\,dS =$$
$$= \frac{1}{2}\int\left(p_1 + \frac{1}{4\pi}\vec{B}_0\cdot\vec{B_1}\right)\xi_n\,dS \tag{A.9}$$

The term under the integral is the pressure on the plasma-vacuum interface which can be expressed from the boundary condition A.3:

$$\frac{1}{2}\int\frac{1}{4\pi}\vec{B_{v0}}\cdot\vec{B_{v1}}\,\xi_n\,dS + \frac{1}{2}\int\left(\frac{1}{8\pi}\frac{\partial B_{v0}^2}{\partial n} - \frac{1}{8\pi}\frac{\partial B_0^2}{\partial n} - \frac{\partial p_0}{\partial n}\right)\xi_n^2\,dS \tag{A.10}$$

On applying conditions A.5 and A.6 one leads the first of the last two integrals to the form:

$$\frac{1}{8\pi}\int\xi_n\vec{B_{v0}}\cdot\vec{B_{v1}}\,dS = -\frac{1}{8\pi}\int\left(\left[\vec{n}\times\vec{A}\right]\cdot\vec{B_{v1}}\right)dS = \frac{1}{8\pi}\int_{vac}(\vec{\nabla}\cdot\left[\vec{A}\times\vec{B_{v1}}\right])dV = \frac{1}{8\pi}\int_{vac}B_{v1}^2\,dV \tag{A.11}$$

where the condition of the zero current in the vacuum region $rot\,\vec{B} = 0$ was used. The last two integrals in eq. A.11 are taken over the vacuum region and represent the energy of the magnetic oscillations. The final expression for the potential energy is:

$$\delta W = \frac{1}{2}\int\left(\gamma p_0(\vec{\nabla}\vec{\xi})^2 + + \frac{1}{4\pi}B_1^2 + (\vec{\xi}\cdot\vec{\nabla}p_0)\cdot(\vec{\nabla}\cdot\vec{\xi}) + \frac{1}{c}\vec{j}_0\cdot\left[\vec{\xi}\times\vec{B_1}\right]\right)dV + \frac{1}{8\pi}\int_{vac}B_{v1}^2\,dV +$$
$$+\frac{1}{2}\int\left(\frac{1}{8\pi}\frac{\partial B_{v0}^2}{\partial n} - \frac{1}{8\pi}\frac{\partial B_0^2}{\partial n} - \frac{\partial p_0}{\partial n}\right)\xi_n^2\,dS \tag{A.12}$$

# Appendix B

# On the kinetic equation for runaway electrons

## B.1 Non-relativistic case

The kinetic equation for fast electrons is a simplified form of the general kinetic equation for plasma that is written here in the Landau form [55, 139]:

$$\frac{\partial f}{\partial t} + \vec{\upsilon}\frac{\partial f}{\partial \vec{r}} - \frac{e\vec{E}}{m}\frac{\partial f}{\partial \vec{\upsilon}} = -\nabla_p \cdot \vec{s}_p \tag{B.1}$$

The collision integral could be expressed by the flux gradient because of the dominant role of small angle collisions. The flux $\vec{s_p}$ should be summed over all species with which an electron is colliding, i.e. electrons and protons in the case considered here. For one species of mass $m$ this flux is given by the formula[1]:

$$s_\alpha = 2\pi(ee')^2 \ln\Lambda \int \left( f\frac{\partial f'}{\partial p'_\beta} - f'\frac{f}{\partial p_\beta} \right) \cdot \left( \frac{\delta_{\alpha\beta}}{\left|\vec{\upsilon} - \vec{\upsilon}'\right|} - \frac{(\upsilon_\alpha - \upsilon_\alpha')(\upsilon_\beta - \upsilon_\beta')}{\left|\vec{\upsilon} - \vec{\upsilon}'\right|^3} \right) d^3p' \tag{B.2}$$

The prime describes values of a "partner" particle. Expression B.2 can be linearized and simplified for runaway electrons (RE) since in the region that is close to the critical velocity $\upsilon_c$: (i) density of particles is so small as to neglect collisions of the type RE-RE, and (ii) the critical velocity (eq. 2.19) is much larger than the thermal one $\upsilon_T$:

$$\upsilon_c = \left(\frac{T_e}{m}\right)^{1/2} \cdot \left(\frac{E_D}{E}\right)^{1/2} \gg \upsilon_T \tag{B.3}$$

The distribution function $f'$ for thermal particles is the Maxwell one for both electrons and ions ($m = m_e$ for electrons and $m = M$ for ions):

$$f' = A \cdot \exp\left(-\frac{p'^2}{2mT}\right) \tag{B.4a}$$

$$\frac{\partial f'}{\partial p'_\beta} = -\frac{p'_\beta}{mT} f' \tag{B.4b}$$

Expansion of eq. B.2 in powers of $\upsilon'/\upsilon$ is restricted up to the second order ($|\vec{\upsilon} - \vec{\upsilon}'| = (\upsilon^2 + \upsilon'^2 - 2\upsilon_\gamma\upsilon_\gamma')^{1/2}$):

$$\frac{1}{\left|\vec{\upsilon} - \vec{\upsilon}'\right|} \approx \frac{\upsilon^2}{\upsilon^3}\left(1 - \frac{\upsilon'^2 - 2\upsilon_\gamma\upsilon_\gamma'}{2\upsilon^2} + \frac{3}{2}\frac{\upsilon_\gamma\upsilon_\delta\upsilon_\gamma'\upsilon_\delta'}{\upsilon^4}\right) \tag{B.5a}$$

[1] Silent summation is assumed over repeating Greek indexes.

$$\frac{1}{\left|\vec{v}-\vec{v}'\right|^3} \approx \frac{1}{v^3}\left(1-\frac{3}{2}\frac{v'^2-2v_\gamma v_\gamma'}{v^2}+\frac{15}{2}\frac{v_\gamma v_\delta v_\gamma' v_\delta'}{v^4}\right) \tag{B.5b}$$

After simple transformations the flux vector in the momentum space assumes the form:

$$s_\alpha = -\frac{\nu_v m_e^2}{2n'}\int\Big(\underbrace{f\frac{p_\beta'}{mT}f'}_{1}+\underbrace{f'\frac{\partial f}{\partial p_\beta}}_{2}\Big)\cdot B_{\alpha\beta}d^3p', \tag{B.6}$$

where $\nu = (4\pi(ee')^2 n' \ln\Lambda)/(m_e^2 v^3)$ is collision frequency, $n'$ is particle density and $B_{\alpha\beta}$ is the sum of expansions B.5.
Because of the evenness of the Maxwell distribution function, the first integral containing $p_\beta' f'$ is composed only by the terms having even powers of $p_\beta'$, i.e. in the second order:

$$(1) \approx \frac{f}{mT}\int p_\beta' f'\left(\delta_{\alpha\beta}v_\gamma v_\gamma' - 3\frac{v_\alpha v_\beta}{v^2}v_\gamma v_\gamma' + v_\alpha v_\beta' + v_\alpha' v_\beta\right)d^3p' \tag{B.7}$$

This integral is easily evaluated by noting that $\int p_\beta' v_\gamma' f' d^3p' = Tn'$, so that this part is ($v_\beta v_\beta = v^2$):

$$(1) \approx \frac{fn'}{mT}\left(\delta_{\alpha\beta}v_\gamma\delta_{\gamma\beta}T - 3\frac{v_\alpha v_\beta}{v^2}v_\gamma\delta_{\beta\gamma}T + 3v_\alpha T + v_\beta\delta_{\alpha\beta}T\right) = 2\frac{v_\alpha f n'}{m}$$

Similarly one can handle the second term standing under the integral in eq. B.6:

$$\begin{aligned}(2) \approx \frac{\partial f}{\partial p_\beta}\int f'\Big(&\delta_{\alpha\beta}v^2 - \frac{1}{2}\delta_{\alpha\beta}v'^2 + \frac{3}{2}\frac{v_\gamma v_\delta}{v^2}v_\gamma' v_\delta'\delta_{\alpha\beta} - v_\alpha v_\beta + \frac{3}{2}v_\alpha v_\beta\frac{v'^2}{v^2} - \frac{15}{2}v_\alpha v_\beta\frac{v_\gamma v_\delta}{v^4}v_\gamma' v_\delta' - 3\frac{v_\alpha v_\gamma}{v^2}v_\beta' v_\gamma' \\ &-3\frac{v_\beta v_\gamma}{v^2}v_\alpha' v_\gamma' + v_\alpha' v_\beta'\Big) = n'\frac{\partial f}{\partial p_\beta}\Big(\delta_{\alpha\beta}v^2 - \frac{3}{2}\frac{T}{m}\delta_{\alpha\beta} + \frac{3}{2}\frac{T}{m}\frac{v_\delta v_\gamma}{v^2}\delta_{\alpha\beta}\delta_{\delta\gamma} - v_\alpha v_\beta + \frac{9}{2}\frac{v_\alpha v_\beta}{v^2}\frac{T}{m} - \frac{15}{2}\frac{v_\alpha v_\beta}{v^4}v_\gamma v_\delta\delta_{\gamma\delta}\frac{T}{m} \\ &-3\frac{v_\alpha v_\gamma}{v^2}\delta_{\beta\gamma}\frac{T}{m} - 3\frac{v_\beta v_\gamma}{v^2}\delta_{\alpha\gamma}\frac{T}{m} + \delta_{\alpha\beta}\frac{T}{m}\Big) = n'\frac{\partial f}{\partial p_\beta}\left(\delta_{\alpha\beta}\left(v^2-\frac{T}{m}\right) - v_\alpha v_\beta\left(1-3\frac{T}{mv^2}\right)\right)\end{aligned} \tag{B.8}$$

Since the particles running away obtain the velocity mainly along the electric field, the distribution function can be expected to be axisymmetric. For this reason it is reasonable to transform equations to the polar system with $z$ axis antiparallel to the electric field and two angle coordinates $\theta$, $\phi$, with $\theta$ being the polar angle relative to the $z$-axis and $\phi$ being the angle in the plane perpendicular to that axis. Some derivatives to be used below are expressed in such coordinate system like ($\partial/\partial\phi = 0$ owing to the symmetry):

$$\frac{\partial v}{\partial v_\alpha} = \frac{v_\alpha}{v} \tag{B.9}$$

$$\frac{\partial\theta}{\partial v_\alpha} = -\frac{1}{\sin\theta}\left(\frac{\delta_{\alpha z}}{v} - \frac{v_\alpha v_z}{v^3}\right) \tag{B.10}$$

$$\frac{\partial}{\partial v_\alpha} = \frac{\partial v}{\partial v_\alpha}\frac{\partial}{\partial v} + \frac{\partial\theta}{\partial v_\alpha}\frac{\partial}{\partial\theta} \tag{B.11}$$

Obviously, any convolution of the type $v_\alpha\partial/\partial v_\alpha$ cancels the angular part:

$$v_\alpha\frac{\partial}{\partial v_\alpha} = v\frac{\partial}{\partial v} - \frac{v_\alpha}{\sin\theta}\left(\frac{\delta_{\alpha z}}{v} - \frac{v_\alpha v_z}{v^3}\right) = v\frac{\partial}{\partial v} - \frac{1}{\sin\theta}\left(\frac{v_z}{v} - \frac{v_z}{v}\right) = v\frac{\partial}{\partial v} \tag{B.12}$$

This simplifies equation B.8:

$$\begin{aligned}&\frac{n'}{m_e}\left(\frac{\partial f}{\partial v}\frac{v_\alpha}{v} - \frac{1}{\sin\theta}\frac{\partial f}{\partial\theta}\left(\frac{\delta_{\alpha z}}{v} - \frac{v_\alpha v_z}{v^3}\right)\right)\cdot\left(v^2-\frac{T}{m}\right) - \frac{n'}{m_e}v v_\alpha\frac{\partial f}{\partial v}\left(1-\frac{3T}{mv^2}\right) = \\ &\qquad = \frac{n'}{m_e}\left(\frac{2T}{m}\frac{\partial f}{\partial v}\frac{v_\alpha}{v} - \frac{1}{\sin\theta}\frac{\partial f}{\partial\theta}\left(\frac{\delta_{\alpha z}}{v} - \frac{v_\alpha v_z}{v^3}\right)\left(v^2-\frac{T}{m}\right)\right)\end{aligned} \tag{B.13}$$

It is left to calculate the divergency of the obtained flux vector. We proceed with the same designation of terms (1) and (2) multiplied by the pre-integral factor:

$$\frac{\partial(1)}{\partial \upsilon_\alpha} = \frac{m_e}{m}\frac{\partial}{\partial \upsilon_\alpha}(\nu(\upsilon)\upsilon_\alpha f) = \frac{m_e}{m}\left(3f\nu(\upsilon) + \upsilon\frac{\partial}{\partial \upsilon} f\nu(\upsilon)\right) = \frac{m_e}{m}\frac{1}{\upsilon^2}\frac{\partial}{\partial \upsilon}\left(\upsilon^3\nu(\upsilon)f\right) \tag{B.14a}$$

$$\frac{\partial(2)}{\partial \upsilon_\alpha} = \frac{1}{2}\left(\frac{6T}{m\upsilon}\nu(\upsilon)\frac{\partial f}{\partial \upsilon} + \frac{2T}{m}\upsilon\frac{\partial}{\partial \upsilon}\left(\frac{\nu(\upsilon)}{\upsilon}\frac{\partial f}{\partial \upsilon}\right) - \frac{\partial}{\partial \upsilon_\alpha}\Phi(\theta)\right) = \frac{1}{2}\left(\frac{2T}{m\upsilon^2}\frac{\partial}{\partial \upsilon}\left(\upsilon^2\nu(\upsilon)\frac{\partial f}{\partial \upsilon}\right) - \frac{\partial}{\partial \upsilon_\alpha}\Phi(\theta)\right) \tag{B.14b}$$

Where $\Phi(\theta)$ stands for the term containing an angle dependence:

$$\frac{\partial\Phi(\theta)}{\partial \upsilon_\alpha} = \frac{\partial}{\partial \upsilon_\alpha}\nu(\upsilon)\frac{1}{\sin\theta}\frac{\partial f}{\partial\theta}\left(\frac{\delta_{\alpha z}}{\upsilon} - \frac{\upsilon_\alpha\upsilon_z}{\upsilon^3}\right)\left(\upsilon^2 - \frac{T}{m}\right) = \left(\upsilon^2 - \frac{T}{m}\right)\nu(\upsilon)\frac{\partial}{\partial \upsilon_\alpha}\left(\frac{1}{\sin\theta}\frac{\partial f}{\partial\theta}\left(\frac{\delta_{\alpha z}}{\upsilon} - \frac{\upsilon_\alpha\upsilon_z}{\upsilon^3}\right)\right) \tag{B.15}$$

Where in doing the last step the property B.12 has been utilized. The remaining derivative can be found straightforwardly:

$$\begin{aligned}\frac{\partial}{\partial \upsilon_\alpha}\left(\frac{1}{\sin\theta}\frac{\partial f}{\partial\theta}\left(\frac{\delta_{\alpha z}}{\upsilon} - \frac{\upsilon_\alpha\upsilon_z}{\upsilon^3}\right)\right) &= \frac{1}{\sin\theta}\frac{\partial f}{\partial\theta}\frac{\partial}{\partial \upsilon_\alpha}\left(\frac{\delta_{\alpha z}}{\upsilon} - \frac{\upsilon_\alpha\upsilon_z}{\upsilon^3}\right) + \left(\frac{\delta_{\alpha z}}{\upsilon} - \frac{\upsilon_\alpha\upsilon_z}{\upsilon^3}\right)\left(\frac{\delta_{\alpha z}}{\upsilon} - \frac{\upsilon_\alpha\upsilon_z}{\upsilon^3}\right)\left(\frac{-1}{\sin\theta}\frac{\partial}{\partial\theta}\left(\frac{1}{\sin\theta}\frac{\partial f}{\partial\theta}\right)\right) = \\ = \frac{1}{\sin\theta}\frac{\partial f}{\partial\theta}\left(\frac{-2\upsilon_z}{\upsilon^3}\right) - \frac{1}{\upsilon^2}\left(1 - \frac{\upsilon_z^2}{\upsilon^2}\right)\frac{1}{\sin\theta}\frac{\partial}{\partial\theta}\left(\frac{1}{\sin\theta}\frac{\partial f}{\partial\theta}\right) &= -\frac{2\cos\theta}{\upsilon^2\sin\theta}\frac{\partial f}{\partial\theta} - \frac{\sin\theta}{\upsilon^2}\frac{\partial}{\partial\theta}\left(\frac{1}{\sin\theta}\frac{\partial f}{\partial\theta}\right) = \\ = -\frac{1}{\upsilon^2}\frac{1}{\sin\theta}\frac{\partial}{\partial\theta}\left(\sin\theta\frac{\partial f}{\partial\theta}\right)\end{aligned} \tag{B.16}$$

Where the obvious relation $\upsilon_z = \upsilon\cos\alpha$ has been used. On inserting equation B.16 into equation B.14 and summing the two parts one finally finds the collisional integral for one "partner" particle:

$$\frac{1}{\upsilon^2}\frac{\partial}{\partial \upsilon}\left(\upsilon^2\nu(\upsilon)\left(\frac{m_e}{m}\upsilon f + \frac{T}{m}\frac{\partial f}{\partial \upsilon}\right)\right) + \frac{\nu(\upsilon)\left(1 - \frac{T}{m\upsilon^2}\right)}{2\sin\theta}\frac{\partial}{\partial\theta}\left(\sin\theta\frac{\partial f}{\partial\theta}\right) \tag{B.17}$$

The first term representing a change with the absolute value of velocity contains the ratio $m_e/m$. This term can be neglected for the electron-ion collisions in comparison with electron-electron collisions $m_e/M \ll 1$, which expresses the fact that the energy exchange between electrons and ions is ineffective. While the second term that is responsible for the change in direction (the pitch angle scattering) does not depend on the mass ratio and is effective for both species.
Transformation of equation B.1 to polar coordinates and summing the collisional integral over protons and electrons result in the suitable kinetic equation:

$$\frac{\partial f}{\partial t} + \frac{eE}{m_e}\left(\cos\theta\frac{\partial f}{\partial \upsilon} - \frac{\sin\theta}{\upsilon}\frac{\partial f}{\partial\theta}\right) - \frac{1}{\upsilon^2}\frac{\partial}{\partial \upsilon}\left(\upsilon^2\nu_{ee}(\upsilon)\left(\upsilon f + \frac{T_e}{m_e}\frac{\partial f}{\partial \upsilon}\right)\right) - \frac{\nu(\upsilon)}{2\sin\theta}\frac{\partial}{\partial\theta}\left(\sin\theta\frac{\partial f}{\partial\theta}\right) = 0 \tag{B.18}$$

Where $\nu(\upsilon)$ designates the effective collision rate with ions and electrons:

$$\nu(\upsilon) \approx \nu_{ei}(\upsilon) + \nu_{ee}(\upsilon)\left(1 - \frac{T_e}{m_e\upsilon^2}\right) \tag{B.19}$$

In new dimensionless variables $u = \upsilon/\sqrt{T_e/m}$, $\tau = t\cdot\nu_{ee}(T_e/m)$, $\mu = \cos\theta$ the equation assumes the form (the term $1/u^2$ in collision frequency was neglected with respect to 1):

$$\frac{\partial f}{\partial\tau} + \frac{E}{E_D}\left(\mu\frac{\partial f}{\partial u} + \frac{1-\mu^2}{u}\frac{\partial f}{\partial\mu}\right) - \frac{1}{u^2}\frac{\partial}{\partial u}\left(\frac{1}{u}\frac{\partial f}{\partial u} + f\right) - \frac{1}{u^3}\frac{\partial}{\partial\mu}\left((1-\mu^2)\frac{\partial f}{\partial\mu}\right) = 0 \tag{B.20}$$

Note that parameter of the task $E/E_D$ is present in the final equation.

## B.2 Collisions with impurities

Here equation B.18 is generalized to include collisions with higher-$Z$ ions. First of all, as obvious the high-$Z$ ions are also much heavier than electron and consequently their role in the energy exchange can be safely neglected even in spite of collisional frequency being proportional to $Z^2$:

$$\frac{\text{ion}}{\text{electron}} \sim Z^2 \frac{m_e}{2ZM} \sim \frac{Z}{3000} \ll 1 \tag{B.21}$$

The contribution of species $j$ appears only in the angular part as $Z_j$ in $e'^2$ (eq. B.2). In summing such contributions over all ions the effective charge $Z = \sum_j Z_j^2 n_j / ne$ and the total collision frequency $\nu = \nu_{ee}(1+Z)$ appear naturally. With this designations the angular part reads:

$$\frac{\nu_{ee}(\upsilon)\left(\frac{1+Z}{2} - \frac{1}{2u^2}\right)}{\sin\theta} \frac{\partial}{\partial\theta}\left(\sin\theta \frac{\partial f}{\partial\theta}\right) \tag{B.22}$$

With $Z = 1$ this equation reduces to the initial one (eq. B.18 ). It is seen that for the runaway generation rate in impure plasma the effective charge has to enter the solution in the form $(1+Z)/2$.

## B.3 Weak relativistic form

The kinetic equation B.1 is known to be relativistic correct [55]. The flux vector in momentum space $s_\alpha$ now has the form (note that the thermal bulk of electrons is still non-relativistic and obeys the Maxwell distribution):

$$s_\alpha = \int \left(f \frac{\partial f'}{\partial p'_\beta} - f' \frac{\partial f}{\partial p_\beta}\right) B_{\alpha\beta} d^3p' = -\int \Big( \underbrace{f \frac{p'_\beta f'}{mT}}_{1} + \underbrace{f' \frac{\partial f}{\partial p_\beta}}_{2} \Big) B_{\alpha\beta} d^3p' \tag{B.23}$$

But in the relativistic case the tensor $B_{\alpha\beta}$ is given by:

$$B_{\alpha\beta} = 2\pi(ee')\ln\Lambda \frac{\gamma\gamma'\left(1 - \vec{v}\vec{v}'/c^2\right)^2}{c\left(\gamma^2\gamma'^2\left(1 - \vec{v}\vec{v}'/c^2\right)^2 - 1\right)^{3/2}} \Bigg\{ \left(\gamma^2\gamma'^2\left(1 - \frac{\vec{v}\vec{v}'}{c^2}\right)^2 - 1\right)\delta_{\alpha\beta} -$$
$$- \frac{\gamma^2}{c^2}\upsilon_\alpha\upsilon_\beta - \frac{\gamma'^2}{c^2}\upsilon_\alpha'\upsilon_\beta' + \frac{\gamma^2\gamma'^2}{c^2}\left(1 - \frac{\vec{v}\vec{v}'}{c^2}\right)\left(\upsilon_\alpha\upsilon_\beta' + \upsilon_\alpha'\upsilon_\beta\right) \Bigg\} \tag{B.24}$$

The sense of the derivation to follow is similar to that for the non-relativistic case in which $B_{\alpha\beta}$ was expanded in series of $\upsilon/\upsilon'$. In the so called weak relativistic approximation temperature of the background particles is assumed to be negligible $T/(mc^2) \ll 1$ and the expansion is limited to the terms independent on temperature. Such terms result from the zeroth order in $\upsilon_i'/c$ in the second component under integral B.23 and also from the second order terms in the first one due to the presence of $1/T$. Consequently $B_{\alpha\beta}$ is to be considered up to the first order in $\upsilon_i'/c$ only.
The relativistic factor $\gamma' = (1 - \upsilon'^2/c^2)^{-1/2}$ entering expression B.24 contains only the second order terms and can be taken to be 1. Then the fraction standing before brackets in equation B.24 is expanded as:

$$\frac{\gamma\gamma'\left(1 - \vec{v}\vec{v}'/c^2\right)^2}{c\left(\gamma^2\gamma'^2\left(1 - \vec{v}\vec{v}'/c^2\right)^2 - 1\right)^{3/2}} \approx \frac{\gamma\left(1 - 2\upsilon_\delta\upsilon_\delta'/c^2\right)}{c\left(\gamma^2-1\right)^{3/2}\left[1 - 2\gamma^2\upsilon_\delta\upsilon_\delta'/\left(c^2(\gamma^2-1)\right)\right]^{3/2}} \approx$$
$$\approx \frac{\gamma}{c\left(\gamma^2-1\right)^{3/2}}\left(1 - 2\frac{\upsilon_\delta\upsilon_\delta'}{c^2}\right)\left(1 + 3\frac{\gamma^2}{\gamma^2-1}\frac{\upsilon_\delta\upsilon_\delta'}{c^2}\right) \approx \frac{\gamma}{c\left(\gamma^2-1\right)^{3/2}}\left(1 + \frac{\gamma^2+2}{\gamma^2-1}\frac{\upsilon_\delta\upsilon_\delta'}{c^2}\right) \tag{B.25}$$

The expression in brackets is transformed in a similar manner:

$$(\dots) \approx \left(\gamma^2 - 1\right)\delta_{\alpha\beta} - 2\gamma^2 \frac{\upsilon_\delta \upsilon_\delta{}'}{c^2}\delta_{\alpha\beta} - \gamma^2 \frac{\upsilon_\alpha \upsilon_\beta}{c^2} + \frac{\gamma^2}{c^2}\left(\upsilon_\alpha \upsilon_\beta{}' + \upsilon_\alpha{}' \upsilon_\beta\right) \tag{B.26}$$

On combining eq. B.25 and eq. B.26 one finds in the 0-th order:

$$\frac{\gamma}{c\left(\gamma^2 - 1\right)^{3/2}}\left((\gamma^2 - 1)\delta_{\alpha\beta} - \gamma^2 \frac{\upsilon_\alpha \upsilon_\beta}{c^2}\right) \tag{B.27}$$

And in the first order:

$$\frac{\gamma}{c\left(\gamma^2 - 1\right)^{3/2}}\left((2 - \gamma^2)\frac{\upsilon_\delta \upsilon_\delta{}'}{c^2}\delta_{\alpha\beta} - \gamma^2 \frac{\gamma^2 + 2}{\gamma^2 - 1}\frac{\upsilon_\alpha \upsilon_\beta}{c^2}\frac{\upsilon_\delta \upsilon_\delta{}'}{c^2} + \frac{\gamma^2}{c^2}\left(\upsilon_\alpha \upsilon_\beta{}' + \upsilon_\alpha{}' \upsilon_\beta\right)\right) \tag{B.28}$$

For further simplifications some relationships for the energy and momentum from the special theory of relativity are required:

$$\gamma \equiv \frac{1}{\sqrt{1 - \upsilon^2/c^2}} = \sqrt{q^2 + 1} \tag{B.29a}$$

$$\frac{\upsilon}{c} = \frac{\sqrt{\gamma^2 - 1}}{\gamma} \tag{B.29b}$$

$$p = m\upsilon\gamma = mc\sqrt{\gamma^2 - 1} \equiv q \cdot mc \tag{B.29c}$$

It is straightforward to integrate the zeroth order terms and to transform it to the nondimensional momentum $q$:

$$(2) = \frac{n\gamma}{c\left(\gamma^2 - 1\right)^{3/2}}\left((\gamma^2 - 1)\left(\frac{p_\alpha}{p}\frac{\partial f}{\partial p} - \frac{1}{\sin\theta}\left(\frac{\delta_{\alpha z}}{p} - \frac{p_\alpha p_z}{p^3}\right)\frac{\partial f}{\partial \theta}\right) - \frac{p_\alpha p}{m_e^2 c^2}\frac{\partial p}{\partial p}\right) = \frac{n\sqrt{q^2 + 1}}{cq^2}q_\alpha \frac{\partial f}{\partial p} -$$
$$- \frac{n\sqrt{q^2 + 1}}{cq}\left(\frac{\delta_{\alpha z}}{p} - \frac{p_\alpha p_z}{p^3}\right)\frac{\partial f}{\partial \theta} - \frac{n\sqrt{q^2 + 1}}{cq^2}q_\alpha \frac{\partial f}{\partial p} = -\frac{n\sqrt{q^2 + 1}}{cq}\left(\frac{\delta_{\alpha z}}{p} - \frac{p_\alpha p_z}{p^3}\right)\frac{\partial f}{\partial \theta} \tag{B.30}$$

Divergency of this part can be found on basis of the results described in the previous sections:

$$\frac{\partial(2)}{\partial v_\alpha} = \frac{n\sqrt{q^2 + 1}}{m_e^2 c^3 q^3}\frac{1}{\sin\theta}\frac{\partial}{\partial\theta}\left(\sin\theta \frac{\partial f}{\partial\theta}\right) \tag{B.31}$$

As it is easy to see, the found part represents the pitch angle scattering independent on mass of a "partner" particle.
Similar integration and rearrangement of the first order terms result in:

$$(1) = \frac{f\gamma}{c\left(\gamma^2 - 1\right)^{3/2}}\frac{n}{mc^2}\left(\upsilon_\delta \delta_{\beta\delta}\delta_{\alpha\beta}(2 - \gamma^2) - \gamma^2 \frac{\upsilon_\alpha \upsilon_\beta}{c^2}\upsilon_\delta \delta_{\delta\beta}\frac{\gamma^2 + 2}{\gamma^2 - 1} + \gamma^2(3\upsilon_\alpha + \upsilon_\beta \delta_{\alpha\beta})\right) =$$
$$\frac{\gamma}{c\left(\gamma^2 - 1\right)^{3/2}}\frac{n}{mc^2}\upsilon_\alpha\left(2 + 3\gamma^2 - \gamma^2 \frac{v^2}{c^2}\frac{\gamma^2 + 2}{\gamma^2 - 1}\right) = \frac{2f}{c\left(\gamma^2 - 1\right)^{3/2}}\frac{n}{m_e mc^2}p_\alpha \gamma^2 = \frac{2fnq_\alpha}{mc^2}\frac{q^2 + 1}{q^3} \tag{B.32}$$

And finally taking divergency:

$$\frac{\partial(1)}{\partial v_\alpha} = \frac{2n}{m_e mc^3}\left(3f\frac{q^2 + 1}{q^3} - 3f\frac{q^2 + 1}{q^4}\frac{q_\alpha q_\alpha}{q} + 2f\frac{q}{q^3}\frac{q_\alpha q_\alpha}{q} + \frac{q^2 + 1}{q^3}\frac{\partial f}{\partial q}\frac{q_\alpha q_\alpha}{q}\right) =$$
$$= \frac{2n}{m_e mc^3 q^2}\frac{\partial}{\partial q}\left((q^2 + 1)f\right) \tag{B.33}$$

This term representing the drag force has a clear dependence on the mass $m$, so that the contribution of ions can be safely neglected.

With coefficient from B.24 the collisional integral including eq. B.33 and eq. B.31 is (impurities were included as described in section B.2):

$$\frac{eE_c}{m_e c}\left(\frac{1}{q^2}\frac{\partial}{\partial q}\left((q^2+1)f\right)+\frac{(Z+1)\sqrt{q^2+1}}{2q^3}\frac{1}{\sin\theta}\frac{\partial}{\partial\theta}\left(\sin\theta\frac{\partial f}{\partial\theta}\right)\right) \tag{B.34}$$

Where $E_c$ is the familiar critical field:

$$E_c = \frac{4\pi e^3 n_e \ln\Lambda}{m_e c^2} \tag{B.35}$$

In contrast to the non-relativistic equation B.18, the weak relativistic form contains only the drag force and pitch angle scattering but not the diffusive term. When combined with a source of the secondary fast particles it allows to find the avalanching RE rate, which does not include the primary mechanism.

# Appendix C

# ECE cut-off

To determine the region suitable for the propagation of electromagnetic wave it is necessary to consider the dispersion relation $k = f(\omega)$. The simplest way to obtain the dispersion relation in plasma is to work out the so called cold wave approximation, i.e. when the temperature of species is neglected.
Here the plane geometry with the magnetic field B parallel to $z$ axis is considered and the usual assumption of all quantities being proportional to $\exp\left(-i(\omega t - \vec{k}\cdot\vec{r})\right)$ is made. In this case the equation of motion for electrons is (since the mobility of ions is much lower, they are taken to be at rest):

$$-i\omega m v_x = -eE_x - \frac{eB}{c} v_y \tag{C.1a}$$

$$-i\omega m v_y = -eE_y + \frac{eB}{c} v_x \tag{C.1b}$$

$$-i\omega m v_z = -eE_z \tag{C.1c}$$

The straightforward solution and the relationship $\vec{j} = -ne\vec{v}$ lead to the expression for the conductivity tensor:

$$\sigma = \frac{ine^2}{m\omega}\frac{1}{1-\frac{\omega_c^2}{\omega^2}} \cdot \begin{pmatrix} 1 & -i\frac{\omega_c}{\omega} & 0 \\ i\frac{\omega_c}{\omega} & 1 & 0 \\ 0 & 0 & 1-\frac{\omega_c^2}{\omega^2} \end{pmatrix}$$

The electromagnetic part of the task is found from the Maxwell system:

$$-\vec{k}\times\left(\vec{k}\times\vec{E}\right) = \frac{\omega^2}{c^2} + \frac{4\pi}{c^2} i\omega\sigma\vec{E} \tag{C.2}$$

A nonzero solution of the system exists only when the determinant of the coefficient matrix is equal to zero. It is this determinant that results in the dispersion relation. In the suitable for ECE case of waves propagating perpendicular to the magnetic field the dispersion relation is:

$$\left(k^2 - \frac{\omega^2}{c^2} + \frac{\omega_p^2}{c^2}\right)\cdot\left(k^2\left(A - \frac{\omega^2}{c^2}\right) + A^2\left(1 - \frac{\omega_c^2}{\omega^2}\right) + \frac{\omega^2}{c^2}\left(\frac{\omega^2}{c^2} - 2A\right)\right) = 0 \tag{C.3}$$

$$A \equiv \frac{\omega_p^2}{c^2}\frac{1}{1-\frac{\omega_c^2}{\omega^2}} \tag{C.4}$$

Two separate branches appear in the solution: the first one incorporated in the first brackets is the ordinary wave having $\vec{E}$ parallel to the magnetic field and the second one is the extraordinary wave characterized by $\vec{E}$ perpendicular to the magnetic field. It is the latter one that is suitable for the ECE measurements.
The region of wave propagation is determined by the extraordinary points of the dispersion relation, i.e. by the points at which the dependence of $k$ on $\omega$ becomes either zero or infinite. The first case is called cut-off and the second one is called resonance. Generally in

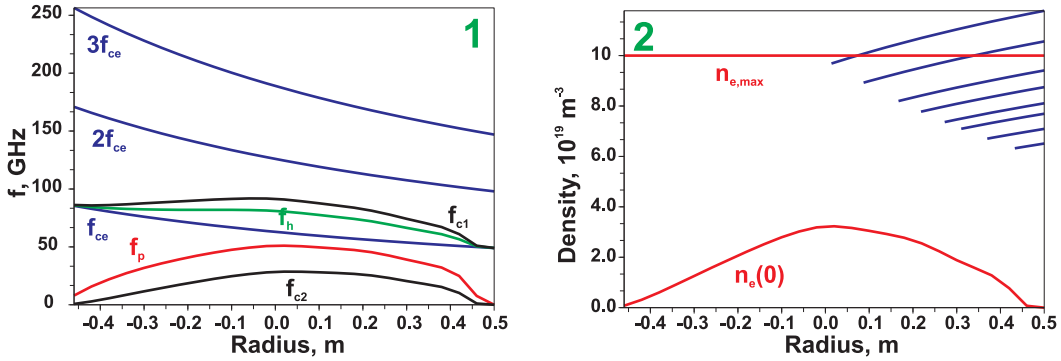


Figure C.1: Cut-off of the second harmonic of ECE. 1 - comparison of the cut-off and resonance frequencies with the electron cyclotron harmonics. The frequencies are calculated for the density profile measured by HCN interferometer in the flat top phase of the discharge. $f_{ce}$ - electron cyclotron frequency; $f_p$ - plasma frequency; $f_h$ - hybrid frequency; $f_{c1,2}$ - the first and the second cut-off frequencies. 2 - dependence of the cut-off density on radius. "blue" - different channels of the ECE diagnostics. Curves start at the position of the emission. "red" - density profiles. $n_e(0)$ - the initial density profile, $n_{e,max}$ - the maximal electron density for a uniform distribution of injected atoms.

cut-off the wave is reflected, while in resonances it is absorbed. For the particular situation considered here, the resonance is easily found to be at the hybrid frequency $\sqrt{\omega_p^2+\omega_c^2}$. To find the cut-off frequencies one has to solve equation:

$$\omega^4+\omega_p^4-\omega^2\omega_c^2+2\omega^2\omega_p^2=0 \tag{C.5}$$

After simple manipulations the solution turns out to be:

$$\left(\omega^2+\omega_p^2\right)^2=\omega^2\left(\omega_c^2+4\omega_p^2\right)$$
$$\omega_{c1,2}=\frac{\sqrt{\omega_c^2+4\omega_p^2}\pm\omega_c}{2} \tag{C.6}$$

The cut-off frequencies and resonance together with a few harmonics of the cyclotron frequency are plotted in figure C.1-1 for the density profile of the TEXTOR discharge used during this work. The first harmonic is always in cut-off, that is why the second one is usually used. The most "dangerous" from all presented frequencies is the largest cut-off $\omega_{c1}$, consequently it is this frequency that determines the density limit of the temperature measurements.

If on the ray path to the antenna the cut-off frequency becomes equal to the frequency of interest, measurements become impossible. The critical density for every position is easily found from the equation for plasma frequency resulting from a rearrangement of eq. C.6:

$$\omega_p^2=\frac{(2\cdot\omega_0-\omega_c)^2-\omega_c^2}{4} \tag{C.7}$$

Dependence of the critical density on radial position for the second ECE harmonic is plotted in figure C.1-2 ("blue" curves). The critical density curve starts at the origin of the signal and follows its path to the antenna located at the low field side. The density profile $n_e(0)$ shown in the figure is that during the flat top phase of the used discharge. The horizontal line $n_{e,max}=10^{20}$ cm$^{-3}$ is the maximal possible density in the experiments with injection of 1.5 bar of He if all atoms were distributed uniformly and were singly ionized. In reality the ECE signal starts to deteriorate already at the density about 80% of the critical one [117]. Therefore it is to be expected that in the course of the MGI experiments the

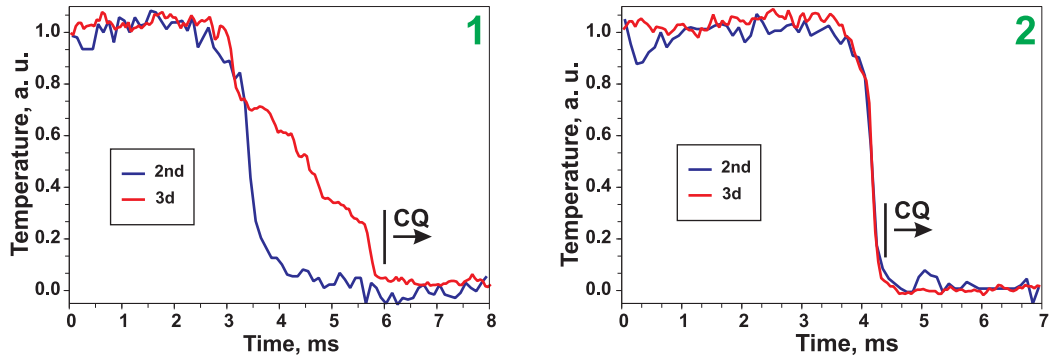


Figure C.2: Measurements with the third harmonic of ECE . 1 -TEXTOR shot 100929, injection of 1.8 bar of He "x1". Note a dramatic difference between the measurements with the second and third harmonics. 2 - TEXTOR shot 100930, injection of 3 bar of Ar "x1".

second ECE harmonic can fall into cut-off. The third harmonic that is not plotted here is unlikely to be in cut-off for low pressure injections because the minimal critical density of $2.7 \cdot 10^{20}$ m$^{-3}$ is higher than the density of $2 \cdot 10^{20}$ m$^{-3}$ that the complete ionization of helium could provide. At higher working pressures $p_w$ the third harmonic can also be in cut-off. These considerations are confirmed by the simultaneous measurements of the central temperature with the second and the third harmonics, fig. C.2. In the helium injection experiments the second harmonic drops to zero by 2 ms earlier than the third one. Moreover, the start of the current quench coincides rather well with the final drop of the third harmonic. In the MGI experiments with argon, both harmonics show the same behaviour, with the complete drop of temperature coinciding with the start of the current quench. While from this point of view the third harmonic is preferable, it has a disadvantage of the emitting region being not optically thick. Consequently the temperature diagnostics has to rely on the density measurements, which are unavailable during disruption. For this reason and also because of a poor radial coverage the third harmonic ECE system was not used systematically.

# Appendix D

# List of used symbols

Units below are given in SI system, note that in the thesis corresponding CGS units can be used instead. The symbols having evident meaning like $T_e$ are omitted.

$a$ [m] - plasma minor radius

$a_{RE}$ [m] - minor radius of the runaway beam

$A$ - inverse aspect ratio $a/R_0$

$A_{RE}$ - inverse aspect ratio of the runaway beam $a_{RE}/R_0$

$\alpha$ [$s^{-1}$] - exponential decay rate of the pressure in the valve working chamber, i.e. the inverse exhaust time $\tau_{Exhaust}$

$\alpha_{id}$ [$s^{-1}$] - ideal exponential decay rate of the pressure in the valve working chamber $c_s S_o/V$

$B_t$ [T] - toroidal magnetic field

$B_r$ [T] - radial magnetic field

$B_{r,eq}$ [T] - equilibrium component of the radial magnetic field, i.e. the radial field produced by the coils creating an elongated plasma configuration

$B_{r,ind}$ [T] - component of the radial magnetic field induced by the eddy currents in the wall

$B_z$ [T] - vertical magnetic field

$\beta_t$ - toroidal plasma beta $\sqrt{\langle p^2 \rangle}/(B_t^2/(2\mu_0))$

$c$ [$m \cdot s^{-1}$] - speed of light

$c_s$ [$m \cdot s^{-1}$] - sound speed

$E_C$ [$V \cdot m^{-1}$] - critical electric field for the generation of runaway electrons

$E_D$ [$V \cdot m^{-1}$] - Dreicer electric field

$E_{ind}$ [$V \cdot m^{-1}$] - induced electric field

$E_{th}$ [J] - thermal content of the tokamak discharge

$E_{mag}$ [J] - magnetic energy associated with the plasma current

$E_{tr}$ [V·m$^{-1}$] - electric field applied by the external transformer

Ef - efficiency of a fast disruption mitigation valve, i.e. the ratio of the injected amount of particles to that initially stored in the working chamber

$f_{primary}$ [m$^{-3}$· s$^{-1}$] - primary generation rate of runaway electrons

F [bar·l·s$^{-1}$] - peak influx rate of particles

$F_p$ [N] - closing force of the disruption mitigation valve exerted by the pressure imbalance on the output orifice

$F_{EM}$ [N] - electromagnetic force exerted by eddy currents that opens the disruption mitigation valve

$F_{ext}$ [N] - electromagnetic eddy currents force acting on the piston of disruption mitigation valve due to the presence of varying tokamak fields

$\phi_d$ [J·m$^{-2}$·s$^{-1/2}$] - wall damage factor, i.e. the value characterizing the surface temperature after a transitive heat load

$\phi_{cr}$ [J·m$^{-2}$·s$^{-1/2}$] - critical value of the damage parameter $\phi_d$ for evaporation/melting of the wall

$\gamma_{loss}$ [s$^{-1}$] - loss rate of runaway electrons

$\gamma_{RE}$ [s$^{-1}$] - avalanching growth rate of the runaway electrons population

$\gamma_v$ [s$^{-1}$] - exponential decay rate of the vessel currents, i.e. the value inverse to the vessel resistive time $\tau_v$

$\gamma_I$ [s$^{-1}$] - exponential decay rate of the plasma current, i.e. the value inverse to the duration of current quench $L/R$

$I$, $I_{pl}$ [A] - full plasma current

$I_\Omega$ [A] - ohmic plasma current

$I_p$ [A] - poloidal component of the halo current

$I_{pl,c}$ [A] - the plasma current flowing in the core region (in contrast to the halo region)

$I_{RE}$ [A] - the current carried by runaway electrons

$I_t$ [A] - toroidal component of the halo current

$I_v$ [A] - current induced in the vessel structures

$j_p$ [A·m$^{-2}$] - current density of poloidal halo current

$j_t$ [A·m$^{-2}$] - current density of toroidal halo current

$L$, $L_{pl}$ [H] - plasma inductance

$L_h$ [H] - inductance of halo region

$L_{RE}$ [H] - inductance of runaway beam

$L_v$ [H] - vessel inductance

$m$ [-; kg] - (1) poloidal mode number. (2) mass of a particle

$m_p$ [kg] - mass of the valve piston

$m_{pl}$ [kg] - mass of the plasma column

$M_{ph}$ [H] - the mutual inductance between the core plasma and the halo region

$M_{vp}$ [H] - the mutual inductance between the plasma and the vessel

$\mu_0 = 4\pi \cdot 10^{-7}$ [H·m$^{-1}$] - magnetic constant

$n$ [-; m$^{-3}$] - (1) decay index of the vertical field $-(R_0/B_z) \cdot (dB_z/dR)$; (2) particle density; (3) toroidal mode number

$n_{atoms}$ [m$^{-3}$] - particle density of injected atoms

$n_{cr}$ - the critical index characterizing coupling of the plasma to the vessel during vertical motion $(2(M'_{vp})^2 R_0)/(\mu_0 L_{pl} L_v)$

$n_D$ [m$^{-3}$] - particle density of deuterium ions

$n_e^*$ [m$^{-3}$] - the total density of electrons including free and bound electrons $n_e + n_{bound}$

$n_G$ [m$^{-3}$] - Greenwald density, i.e. the maximum line averaged density achievable at the given plasma current and plasma cross section

$n_{RE}$ [m$^{-3}$] - particle density of runaway electrons

$N_{atoms}$ - total number of injected atoms

$\nu$ [s$^{-1}$] - collision rate

$p_b$ [Pa] - pressure in the back chamber of disruption mitigation valve

$p_w$ [Pa] - pressure in the working chamber of disruption mitigation valve

$q$ - (1) overpressure factor of the fast valve $p_w/p_b$; (2) safety factor of tokamak; (3) dimensionless momentum of a particle $q \equiv p/mc$

$R_0$ [m] - tokamak major radius

$R_h$ [Ohm] - resistance of halo region

$R_v$ [Ohm] - vessel resistance

$S$ [$m^2$; $m^3 \cdot s^{-1}$] - (1) plasma cross section; (2) primary generation rate of runaway electrons

$S_b$ [$m^2$] - surface of the piston back part

$S_o$ [$m^2$] - cross section of the valve output orifice

$S_{RE}$ [$m^2$] - cross section of the runaway beam

$S_{REL}$ - the relativistic correction factor to the primary generation rate of runaway electrons

$\sigma$ [$S \cdot m^{-1}$; $m^2$] - (1) electrical conductivity; (2) - scattering cross section

$\sigma_h$ [$S \cdot m^{-1}$] - electrical conductivity of the halo region

$\sigma_{pl,c}$ [$S \cdot m^{-1}$] - electrical conductivity of the core plasma

$\sigma_{tr}$ [$m^2$] - transport cross section

$t^*$ [s] - duration of the valve injection

$t_{CQ}$ [s] - start of the current quench

$t_G$ [s] - moment of the gas arrival to the plasma edge

$t_{TQ}$ [s] - onset of the thermal quench

$\tau_{CQ}$ [s] - duration of the current quench

$\tau_{Exhaust}$ [s] - exhaust time of the disruption mitigation valve, i.e. the e-folding time of the particle content in the working chamber

$\tau_v$ [s] - resistive time of the vessel $L_v/R_v$

Th [bar·l] - throughput of disruption mitigation valve, i.e. the total number of injected particles

$\upsilon_c$ [$m \cdot s^{-1}$] - critical velocity for runaway particles, i.e. the velocity at which the collisional drag force becomes equal to the acceleration in electric field $\sqrt{(T_e E_D)/(mE)}$

$\upsilon_T$ [$m \cdot s^{-1}$] - thermal velocity of a particle

$w_h$ - width of the halo region

$Z$, $Z_{eff}$ - effective charge $\langle Z^2 \rangle$

# List of Figures

# List of Tables

# Bibliography


[1] Renhan E., Thermonuclear Burn Criteria, Transactions of Fusion Science and Technology (Special Issue, Proceedings of the Sixth Carolus Magnus Euro-Summer School on Plasma and Fusion Energy Physics), vol. 45 (2004), pp. 15 - 23

[2] Troyon F., Gruber R., et al., MHD Limits to Plasma Confinement, Plasma Physics and Controlled Fusion, vol. 26 (1984), pp. 209 - 215

[3] Artcimovich L. A., Shafranov V. D., Tokamak with Non-circular Cross Section of Plasma Loop, JETP Letters, vol. 15 (1972), pp. 72 - 76 (in Russian)

[4] Greenwald M., Terry J. L., Wolfe S. M., A New Look at Density Limits in Tokamaks, Nuclear Fusion, vol. 28 (1988), pp. 2199 - 2207

[5] Luk'yanov S. Yu., Hot Plasma and Controlled Thermonuclear Fusion, Moscow "Nauka" 1975, 398 pages (in Russian)

[6] Artcimovich L. A., Sagdeev R. Z., Plasma Physics for Physicists, Moscow "Atomizdat" 1979, 322 pages

[7] Shafranov V. D., Plasma Equilibrium in Magnetic Field, Reviews of Plasma Physics vol. 2 (ed. by Leontovich), Moscow "Atomizdat" 1963, pp. 92 - 131 (in Russian)

[8] Neubauer O., Czymek G., et al., Design Features of the Tokamak TEXTOR, Fusion Science and Technology, vol. 47 (2005) (Special Issue on TEXTOR), pp. 76 - 86

[9] http://www.iter.org

[10] Lazarus E. A., Chu M. S., et al., Higher Beta at Higher Elongation in the DIII-D Tokamak, Physics of Fluids B, vol. 3 (1991), pp. 2220 - 2228

[11] Strait E. J., Stability of High-beta Tokamak Plasmas, Physics of Plasmas, vol. 1 (1994), pp. 1415 - 1431

[12] Wesson J., The Science of JET, Cuhlam 2000, 179 pages

[13] Mukhavatov V. S., Shafranov V. D., Plasma Equilibrium in a Tokamak, Nuclear Fusion, vol. 11 (1971), pp. 605 - 633

[14] Kadomtsev B. B., Hydromagnetic plasma stability, Reviews of Plasma Physics vol. 2 (ed. by Leontovich), Moscow "Atomizdat" 1963, pp. 132 - 176 (in Russian)

[15] Bernstein I. B., Frieman E. A., et al., An Energy Principle for Hydromagnetic Stability Problems, Proceedings of the Royal Society, vol. A244 (1958), pp. 17 - 40

[16] Gantmacher F. R., Lectures on Analytical Mechanics, Moscow "Nauka" 1966, 300 pages (in Russian)

[17] Wesson J., Tokamaks, 3rd edition, Clarendon Press, Oxford 2004, 750 pages

[18] Wesson J. A., Gill R. D., et al., Disruptions in JET, Nuclear Fusion, vol. 29 (1989), pp. 641 - 666

[19] Schüller F. C., Disruptions in Tokamaks, Plasma Physics and Controlled Fusion, vol. 37 (1995), pp. A135 - A162

[20] Ward D. J., Wesson J. A., Impurity Influx Model of Fast Tokamak Disruptions, Nuclear Fusion, vol. 32 (1992), pp. 1117 - 1123

[21] Kadomtsev B. B., Disruptive Instability in Tokamaks, Soviet Journal of Plasma Physics, vol. 1 (1975), pp. 389 - 391

[22] ITER Physics expert group on Disruptions, Plasma Control and MHD, Chapter 3: MHD Stability, Operational Limits and Disruptions, Nuclear Fusion, vol. 39 (1999), pp. 2251-2389

[23] Kadomtsev B. B., Pogutse O. P., Nonlinear Helical Perturbations of a Plasma in the Tokamak, Soviet Physics - JETP, vol. 38 (1973), pp. 283 - 290

[24] Greenwald M., Density Limits in Toroidal Plasmas, Plasma Physics and Controled Fusion, vol. 44 (2002), pp. R27 - R80

[25] Waidmann G., Kuang G., Density Limits and Evolution of Disruptions in Ohmic TEXTOR Plasmas, Nuclear Fusion, vol. 32 (1992), pp. 645 - 654

[26] Yoshino R., Neyatani Y., et al., The Softening of Current Quenches in JT-60U, Nuclear Fusion, vol. 33 (1993), pp. 1599 - 1612

[27] Zohm H., Maraschek M., et al., MHD Stability and Disruption Physics in ASDEX Upgrade, Plasma Physics and Controled Fusion, vol. 37 (1995), pp. A 313 - A324

[28] Wolf R. C., Internal Transport Bariers in Tokamak Plasmas, Nuclear Fusion, vol. 45 (2003), pp. R1 - R91

[29] Riccardo V., Loarte A. and the JET EFDA Contributors, Timescale and Magnitude of Plasma Thermal Energy Loss before and during Disruptions in JET, Nuclear Fusion, vol. 45 (2005), pp. 1427 - 1438

[30] Sugihara M., Lukash V., et al., Edge Safety Factor at the Onset of Plasma Disruption during VDEs in JT-60U, Plasma Physics and Controled Fusion, vol. 46 (2004), pp. 15811589

[31] Gruber O., Lackner K., etc., Vertical Displacement Events and Halo Currents, Plasma Physics and Controlled Fusion, vol. 35 (1993), pp. B191-B204

[32] Putvinski S., Barabashi P., etc., Halo Current, Runaway Electrons and Disruption Mitigation in ITER, Plasma Physics and Controlled Fusion, vol. 39 (1997), pp. B157 - B171

[33] Smythe W. R., Static and Dynamic Electricity, 2nd ed. McGraw-Hill, New York, 1950, 608 pages

[34] Sivukhin D. V., Course of general physics vol. 3 Electricity, Moscow “Fizmatlit”, 2004, 656 pages (in Russian)

[35] Lazarus E. A., Lister J.B., Neilson G. H., Control of the Vertical Instability in Tokamaks, Nuclear Fusion, vol. 30 (1990), pp. 111-141

[36] Granetz R.S., Hutchinson I.H., et al., Disruptions and Halo Currents in Alcator C-MOD, Nuclear Fusion, vol. 36 (1996), pp. 545 - 556

[37] Nakamura Y., Yoshino R., et al., $\beta_p$-collapse Induced Vertical Displacement Event in High-$\beta_p$ Tokamak Disruptions, Plasma Physics and Controlled Fusion, vol. 38 (1996), pp. 1791 - 1804

[38] Nakamura Y., Yoshino R., et al., Mechanism of Vertical Displacement Events in JT-60U Disruptive Discharges, Nuclear Fusion, vol. 36 (1996), pp. 643 - 655

[39] Yoshino R., Nakamura Y., Neyatani Y., Avoidance of VDEs during Plasma Current Quench in JT-60U, Nuclear Fusion, vol. 36 (1996), pp. 295 - 307

[40] Yoshino R., Nakamura Y., Neyatani Y., Plasma Equilibrium Control during Slow Plasma Current Quench with Avoidance of Plasma-wall Interaction in JT-60U, Nuclear Fusion, vol. 37 (1997), pp. 1161 - 1166

[41] Nakamura Y., Puatasso G., et al., Axisymmetric Disruption Dynamics Including Current Profile Changes in the ASDEX-Upgrade Tokamak, Plasma Physics and Controlled Fusion, vol. 44 (2002), pp. 1471 - 1481

[42] Ward D. J., Jardin S. C., Effects of Plasma Deformability on the Feedback Stabilization of Axisymmetric Modes in Tokamak Plasmas, Nuclear Fusion, vol. 32 (1992), pp. 973 - 994

[43] Ward D. J., Hoffman F., Active Feedback Stabilization of Axisymmetric Modes in Highly Elongated Tokamak Plasmas, Nuclear Fusion, vol. 34 (1994), pp. 401 - 415

[44] Sayer R. O., Peng Y.-K. M., et al., TSC Plasma Halo Simulation of a DIII-D Vertical Displacement Episode, Nuclear Fusion, vol. 33 (1993), pp. 969 - 978

[45] Dreicer H., Electron and Ion Runaway in a Fuly Ionized Gas I, Physical Review, vol. 115 (1959), pp. 238 - 249

[46] Dreicer H., Electron an Ion Runaway in a Fully Ionized Gas II, Physical Review, vol. 117 (1960), pp. 329 - 342

[47] Rosenbluth M. N., MacDonald W. M., Judd D. L., Fokker-Planck Equation for an Inverse-Square Force, Physical Review, vol. 107 (1957), pp. 1 - 6

[48] Fuchs V., Caims R. A., et al., Velocity-space Structure of Runaway Electrons, Physics of Fluids, vol. 29 (1986), pp. 2931 - 2936

[49] Gurevich A. V., On the Theory of Runaway Electrons, Soviet Physics JETP, vol. 12 (1961), pp. 904 - 912

[50] Gurevich A. V., On the Amount of Accelerated Particles in an Ionized Gas under Various Accelerating Machanisms, Soviet Physics JETP, vol. 11 (1960), pp. 1150 - 1157

[51] Lebedev A. N., Contribution to the Theory of Runaway Electrons, Soviet Physics JETP, vol. 21 (1965), pp. 931 - 933

[52] Cohen R. H., Runaway Electrons in an Impure Plasma, The Physics of Fluids, vol.19 (1976), pp. 239 - 244

[53] Kulsrud R. M., Sun Y.-C., et al., Runaway Electrons in Plasma, Physics Review Letters, vol. 31 (1973), pp. 690 - 693

[54] Jaspers R., Finken K. H., et al., Experimental Investigation of Runaway Electron Generation in TEXTOR, Nuclear Fusion, vol. 33 (1993), pp. 1775 - 1785

[55] Landau L. D., Lifshitz E. M., Course of Theoretical Physics, Volume 10: Physical kinetics, Moscow "Nauka" 1979, 527 pages (in Russian)

[56] Connor J. W., Hastie R.J., Relativistic Limitations on Runaway Electrons, Nuclear Fusion, vol. 15 (1975), pp. 415 - 424

[57] Fussman G., On the Motion of Runaway Electrons in Momentum Space, Nuclear Fusion, vol. 19 (1979), pp. 327 - 334

[58] Martin-Solis J. R., Alvarez J. D., et al., Momentum-space Structure of Relativistic Runaway Electrons, Physics of Plasmas, vol. 5 (1998), pp. 2370 - 2377

[59] Bakhtiari M., Kramer G. J., et al., Role of Bremsstrahlung Radiation in Limiting the Energy of Runaway Electrons in Tokamaks, Physical Review Letters, vol. 94 (2005), pp. 215003-1 - 215003-4

[60] Sokolov Yu. A., "Multiplication" of Runaway Electrons in a Tokamak, Letters to JETP, vol. 29 (1979), pp. 244 - 246 (in Russian)

[61] Landau L. D., Lifshitz E. M., Course of Theoretical Physics, Volume 4: Quantum Electrodynamics, Moscow "Nauka" 1989, 723 pages (in Russian)

[62] Jayakumar R., Fleischmann H. H., Zweben S. J., Collisional Avalanche Exponentiation of Runaway Electrons in Electrified Plasmas, Physics Letters A, vol. 172 (1993), pp. 447 - 451

[63] Rosenbluth M. N., Putvinski S. V., Theory for Avalanche of Runaway Electrons in Tokamaks, Nuclear Fusion, vol. 37 (1997) pp. 1355 - 1362

[64] Chiu S. C., Rosenbluth M. N., Harvey R. W., Chan V. S., Fokker-Planck Simulation of Knock-on Electron Runaway Avalanche and Bursts in Tokamaks, Nuclear Fusion, vol. 38 (1998), pp. 1711 - 1721

[65] Paley J. I., Andrew P., et al., Energy Flow during Disruption in JET, Journal of Nuclear Materials, vol. 337 - 339 (2005), pp. 702 - 706

[66] Hollmann E. M., Gray D. S., et al., Radiated Power Measurement during the Thermal Quench Phase of a Density Limit Disruption, Physics of Plasmas, vol. 10 (2003), pp. 2863 - 2870

[67] Loarte A., Saibene G., et al., Transient Heat Loads in Current Fusion Experiments, Extrapolations to ITER and Consequensec for its Operation, Physica Scripta, T128 (2007), pp. 222 - 228

[68] Landau L. D., Lifshitz E. M., Course of Theoretical Physics, Volume 6: Hydrodynamics, Moscow "Nauka" 1986, 736 pages (in Russian)

[69] Sugihara M., Shimada M., Disruption Scenarios, their Mitigation and Operation Window in ITER, Nuclear Fusion, vol. 47 (2007), pp. 337 - 352

[70] ITER Physics Expert Groups on Divertor, Divertor Modeling and Database and ITER Physics Basis Editors, Chapter 4: Power and Particle Control, Nuclear Fusion, vol. 39 (1999), pp. 2391-2469

[71] Knight P. J., Castle G. G., et al., Analysis of Vertical displacement Events and Halo Currents in COMPAS-D, Nuclear Fusion, vol. 40 (2000), pp. 325 - 337

[72] Riccardo V., Hender T.C., etc., Analysis of JET halo currents, Plasma physics and controled fusion, v 46 (2004), pp. 925 - 934

[73] Humphreys D. A. and Kellman A. G., Analytic Modelling of Axisymmetric Disruption Halo Currents, Physics of Plasmas, vol. 6 (1999), pp. 2742 - 2756

[74] Humphreys D. A., Whyte D. G., Classical Resistivity in a Post-thermal Quench Plasma, Physics of Plasmas, vol. 7 (2000), pp. 4057 - 4061

[75] Humphreys D. A., Whyte D. G., etc., Predictive Modeling of Plasma Halo Evolution in Post-thermal Quench Disrupting Plasmas, $33^{rd}$ EPS Conference on Plasma Phycs, Rome 19 - 23 June 2006

[76] Riccardo V., Andrew Ph. etc., Disruption design criteria for Joint European Torus in-vessel Components, Fusion Science and Technology vol. 43 (2003), pp. 493-502

[77] Pautasso G., Tichmann C., et al., On-line Prediction and Mitigation of Disruptions in ASDEX Upgrade, Nuclear Fusion, vol. 42 (2002), pp. 100 - 108

[78] Cannas B., Fanni A., et al., Disruption Forecasting at JET Using Neural Networks, Nuclear Fusion, vol. 44 (2004), pp. 68 - 76

[79] Yoshino R., Neural-net Disruption Predictor in JT-60, Nuclear Fusion, vol. 43 (2003), pp. 1771 - 1778

[80] Wroblewski D., Jahns G. L., Tokamak Disruption Alarm Based on A Neural Network Model of the High-$\beta$ limit, Nuclear Fusion, vol. 37 (1997), pp. 725 - 741

[81] Yoshino R., Neural-net Predictor for $\beta$-limit Disruptions in JT-60, Nuclear Fusion, vol. 45 (2005), pp. 1232 - 1246

[82] Windsor C. G., Pautasso G., et al., A Cross-tokamak Neural Network Disruption Predictor for the JET and ASDEX Upgrade Tokamaks, Nuclear Fusion, vol. 45 (2005), pp. 337 - 350

[83] Parks P. B., Turnbull R. J., Foster C. A., A Model for the Ablation Rate of a Solid Hydrogen Pellet in a Plasma, Nuclear Fusion, vol. 17 (1977), pp. 539 - 556

[84] Milora S. L., Houlberg W. A., et al., Pellet Fuelling, Nuclear Fusion, vol. 35 (1995), pp. 657 - 754

[85] Timokhin V. M., Sergeev V. Yu., Kuteev B. V., Study of Discharge Quenching in the T-10 Tokamak by Injecting HIgh-Z Impurity Pellets, Plasma Physics Reports, vol. 27 (2001), pp. 195 - 208

[86] Pautasso G., Büchl K., et al., Use of Impurity Pellets to Control Energy Dissipation during Disruption, Nuclear Fusion, vol. 36 (1996), pp. 1291 - 1297

[87] Taylor P. L., Kellman A. G., et al., Disruption MItigation Studies in DIII-D, Physics of Plasmas, vol. 6 (1999), pp. 1872 - 1879

[88] Evans T. E., Kellman A. G., et al., Measurements of Non-axisymmetric Halo Currents with and without "Killer" Pellets during Disruptions in the DIII-D Tokamak, Journal of Nuclear Materials, vol. 241 - 243 (1997), pp. 606 - 611

[89] Yoshino R., Kondoh T., et al., Fast Plasma Shutdown by Killer Pellets Injection in JT-60U with Reduced Heat Flux on the Divertor Plate and Avoiding Runaway Electron Generation, Plasma Physics and Controlled Fusion, vol. 39 (1997), pp. 313 - 332

[90] Finken K. H., Mank G., et al., Mitigation of Disruptions by Fast Helium Gas Puffs, Nuclear Fusion, vol. 41 (2001), pp. 1651 - 1661

[91] Martin G., Sourd F., Saint-Laurent F. et al., Disruption Mitigation at Tore-Supra, at 32nd EPS Plasma Physics Conference,Tarragona (2005), http://www-pub.iaea.org/MTCD/Meetings/PDFplus/fusion-20-preprints/EX_10-6Rc.pdf

[92] Savchkov A., Mitigation of Disruptions in a Tokamak by Means of Large Gas Injection, PhD Thesis, Mathematisch-Naturwissenschaftlichen Fakultät der Heinrich-Heine Universität Düsseldorf (2002)

[93] Taylor P. L., Kellman A. G., et al., Experimental Measurements of the Current, Temperature, and Density Profile Changes during a Disruption in the DIII-D Tokamak, Physical Review Letters, 76 (1996), pp. 916 - 919

[94] Whyte D. G., Humphreys D. A., Taylor P. L., Measurement of Plasma Electron Temperature and Effective Charge during Tokamak Disruptions, Physics of Plasmas, vol. 7 (2000), pp. 4052 - 4056

[95] Whyte D. G., Jernigan T. C. et al., Mitigation of Tokamak Disruptions Using High-Pressure Gas Injection, Physical Review Letters, vol. 89 (2002), pp. 055001-1 - 055001-4

[96] Whyte D. G., Jernigan T. C., et al., Disruption Mitigation with High-pressure Noble Gas Injection, Journal of Nuclear Materials, vol. 313 - 316 (2003), pp. 1239 - 1246

[97] Hollmann E. M., Jernigan T. C. et al., Measurements of Impurity and Heat Dynamics during Noble Gas Jet-initiated Fast Plasma Shutdown for Disruption Mitigation in DIIID, Nuclear Fusion, vol. 45 (2005), pp. 1046 - 1055

[98] Hollmann E. M., Jernigan T. C., et al., Observation of $q$–profile Dependence in Noble Gas Injection Radiative Shutdown Times in DIII-D, Physics of Plasmas, vol. 14 (2007), pp. 012502-1 - 012502-8

[99] Granetz R, Whyte D. G., et al., Gas Jet Disruption Mitigation Studies at ALCATOR C-Mod, Nuclear Fusion, vol. 46 (2006), pp. 1001 - 1008

[100] Izzo V. A., A Numerical Investifation of the Effects of Impurity Penetration Depth on Disruption MItigation b Massive High-pressure Gas Jet, Nuclear Fusion, vol. 46 (2006), pp. 541 - 547

[101] Bakhtiari M., Kawano Y., et al., Fast Plasma Shutdown Scenarios in the JT-60U Tokamak Using Intense Mixed Gas Puffing, Nuclear Fusion, vol. 42 (2002), pp. 1197 - 1204

[102] Bakhtiari M., Tamai H., et al., Study of Plasma Termination Using High-Z Noble Gas Puffing in the JT-60U Tokamak, Nuclear Fusion 45 (2005), pp. 318 - 325

[103] Riccardo V. and JET EFDA contributors, Disruptions and Disruption Mitigation, Plasma Physics and Controlled Fusion, vol. 45 (2003), pp. A269 - A284

[104] Savtchkov A., Finken K. H. et al., Development of a Fast Valve for Mitigating Disruptions in Tokamaks, Review of Scientific Instruments, vol. 73 (2002), pp. 3490 - 3493

[105] Bates S. C., Burrell K. H., Fast Gas Injection System for Plasma Physics Experiments, Review of Scientific Instruments, vol. 55 (1984), pp. 934 - 939

[106] Soukhanovskii V. A., Kugel H.W. et al., Supersonic Gas Injector for Fueling and Diagnostic Applications on the National Spherical Torus Experiment, Review of Scientific Instruments, vol. 75 (2004), pp. 4320 - 4323

[107] Whyte D. G., Gas Jet Disruption Mitigation Studies, at 33rd EPS Plasma Physics Conference, Rome (2006), http://eps2006.frascati.enea.it/presentazioni_finali/Aula_Mayor/Thursday/Whyte/EPS_06_whyte.pdf

[108] Milora S. L., Combs S.K. et al., Fast-opening Magnetic Valve for High-pressure Gas Injection and Applications to Hydrogen Pellet Fueling Systems, Review Scientific Instruments, vol. 57 (1986), pp. 2356 - 2358

[109] Combs S. K., Foust C. R. and Gouge M. J., Fast-opening, High-throughput Gas Valve and Application for Inertial Fusion Energy R&D, Review Scientific Instruments, vol. 75 (2004), pp. 270 - 272

[110] Erents S. K., Finken K.-H., Savchkov A., Disruption Mitigation Valve - Project Final Report, EFDA JET, 2006, 74 pages

[111] Landau L. D., Lifshitz E. M., Course of Theoretical Physics, Volume 8: Electrodynamics of Continous Media, Moscow "Nauka" 1982, 620 pages (in Russian)

[112] www.prinsci.com/ffcam

[113] Hamamatsu 7868-02, $\lambda = 670$ nm, $\tau_{rise} = \tau_{fall} \approx 60$ ns, angle divergency less than 5°, http://usa.hamamatsu.com/assets/pdf/parts_L/L7868.pdf

[114] Macroblock constant current LED-driver MBI5026, $I \leq 60$ mA, 16 output channels, frequency up to 25 MHz, $\tau_{response} = 200$ ns. http://www.mblock.com.tw/download/pdf/MBI5026/Datasheets/MBI5026%20Datasheet%20VA.02.pdf

[115] Ralchenko, Yu., Jou, F.-C., Kelleher, D.E., Kramida, A.E., Musgrove, A., Reader, J., Wiese, W.L., and Olsen, K. (2007). NIST Atomic Spectra Database (version 3.1.2), Available online: http://physics.nist.gov/asd3 [2007, April 24]. National Institute of Standards and Technology, Gaithersburg, MD.

[116] K. P. Dere, E. Landi, H.E. Mason, B. C. Monsignori Fossi, P. R. Young, CHIANTI - An Atomic Database For Emission Lines - Paper I: Wavelengths greater than 50 A (Version 1), Astronomy and Astrophysics Supplementary Series, vol. 125 (1997), pp. 149-173; E. Landi, G. Del Zanna, P.R. Young, K.P. Dere, H.E. Mason, M. Landini, CHIANTI - an atomic database for emission lines - Paper VII: New data for X-rays and other improvements (Version 5), The Astrophysical Journal Supplementary Series, vol. 162 (2006) , pp. 261 - 280. Available online: http://www.arcetri.astro.it/science/chianti/chianti.html.

[117] Krämer-Flecken A., Microwave and Far-infrared Diagnostics, Transactions of Fusion Science and Technology (Special Issue, Proceedings of the Sixth Carolus Magnus Euro-Summer School on Plasma and Fusion Energy Physics), vol. 45 (2004), pp. 418 - 425.

[118] Landau L. D., Lifshitz E. M., Course of Theoretical Physics, Volume 2: Field Theory, Moscow "Nauka" 1988, 509 pages (in Russian)

[119] Son E. E., Lecterues on Physical Mechanics, Moscow "MIPT" 2002, 181 pages (in Russian)

[120] Bekefi J., Radiation Processes in Plasmas, Moscow "Mir", 1971, 438 pages (Russian translation from: Bekerfi J., Radiation Processes in Plasmas, John Wiley and Sons Inc.)

[121] Liang Y., Koslowski H. R., et al., Observation of mode structure and mode locking using the Dynamic Ergodic Divertor on TEXTOR, 31st EPS Conference on Plasma Physics London, 28 June - 2 July 2004 ECA Vol.28G, P-1.126 (2004)

[122] Ternov I. M., Synchrotron emmission, Uspekhi Fizicheskih Nauk (Advances in Physical Sciences), vol. 165(1995), pp. 429 - 456 (in Russian)

[123] Finken K. H., Watkins J. G., et al., Observation of Infrared Synchrotron Radiation from Tokamak Runaway Electrons in TEXTOR, Nuclear Fusion, vol. 30 (1990), pp. 859 - 870

[124] Entrop I., Lopes Cardozo N. J., et al., Scale Size of Magnetic Turbulence in Tokamaks Probed wirh 30-MeV Electrons, Physical Review Letters, vol. 84 (2000), pp. 3606 - 3609

[125] Jaspers R., Lopes Cardozo N. J., et al., A Synchrotron Radiation Diagnostics to Observe Relativistic Runaway Electrons in a Tokamak Plasma, Review of Scientific Instruments, vol. 72 (2001), pp. 466 - 470

[126] Jackson J. D., Classical Electrodynamics, John Wiley and Sons, Inc., New York - London, 1962, 703 pages

[127] Wesson J. A., Ward D. J., Rosenbluth M. N., Negative Voltage Spike in Tokamak Disruptions, Nuclear Fusion, vol. 30 (1990), pp. 1011 - 1014

[128] Sivukhin D. V., Course of general physics vol. 4 Optics, Moscow " Fizmatlit", 1980, 752 pages (in Russian)

[129] van der Meiden H. J., Varshney S. K., et al., 10 kHz Repetitive High-resolution TV Thomson Scattering on TEXTOR: Design and Performance, Review of Scientific Instruments, vol. 77 (2006), pp. 10E512-1- 10E512-8

[130] Fournier K. B., Cohen M., May M. J. and Goldstein W. H., Ionization State Distribution and Radiative Cooling Rate for Argon in a Low-density Plasma, Atomic Data and nuclear Data Tables, vol. 70 (1998), pp. 231 - 254

[131] Fournier K. B., Cohen M., May M. J. and Goldstein W. H., Erratum:Ionization State Distribution and Radiative Cooling Rate for Argon in a Low-density Plasma, Atomic Data and nuclear Data Tables, vol. 74 (2000), pp. 333 - 334

[132] Post D. E., Jensen R. V., Steady-State Radiative Cooling Rates for Low-Density, High-Temperature Plasmas, Atomic Data and Nuclear Data Tables, vol. 20 (1977), pp. 397 - 439

[133] Spitzer L., Physics of Fully Ionized Gases, Interscience Publishers, 1962, 170 pages

[134] Jarvis O. N., Sadler G., Thompson J. L., Photoneutron Production Accompanying Plasma Disruptions in JET, Nuclear Fusion, vol. 28 (1988), pp. 1981 - 1993

[135] Gill R. D., Generation and Loss of Runaway Electrons Following Disruptions in JET, Nuclear Fusion, vol. 33 (1993), pp. 1613 - 1625

[136] Gill R. D., Alper B., et al., Direct Observations of Runaway Electrons during Disruptions in the JET Tokamak, Nuclear Fusion, vol. 40 (2000), pp. 163 - 174

[137] Hoenen F., Euringer H., et al., In situ Calibration of Neutron Detectors on TEXTOR, Review of Scientific Instruments, vol. 63 (1992), pp. 1945 - 1952

[138] Voronov G. S., A Practical Fit Formula for Ionization Rate Coefficients of Atoms and Ions by Electron Impact: Z = 1 - 28, Atomic Data and Nuclear Data Tables, vol. 65 (1997), pp. 1 - 35

[139] Landau L.D., Kinetic Equation in the Case of Coloumb Ineraction, JETP, vol. 7 (1937), p. 203 (in Russian)

[140] Toyama H., Makishima K., et al., Magnetohydrodinamyc Properties of the D-shaped Tokamak Controlled by Active Field Shaping, Physical Review Letters, vol. 37 (1976), pp. 18 - 21

[141] Strait E. J., Lao L. L., et al., Observation of Poloidal Current Flow to the Vacuum Vessel Wall during Vertical Instabilities in the DIII-D Tokamak, Nuclear Fusion, vol. 31 (1991), pp. 527 - 534

[142] Goldston R. J., Rutherford P. H., Introduction to Plasma Physics, IOP Publishing Ltd., 1995, 491 pages

[143] Landau L. D., Lifshitz E. M., Course of Theoretical Physics, Volume 1: Theoretical Mechanics, Moscow "Nauka" 1988, 215 pages (in Russian)

Jül-4288
Februar 2009
ISSN 0944-2952